NOVEL ULTRASOUND IMAGING METHODS FOR THE CHARACTERIZATION OF TISSUE MICROVASCULAR NETWORKS

by

İpek Özdemir

APPROVED BY SUPERVISORY COMMITTEE:

Kenneth Hoyt, Chair

Clark A. Meyer

Shashank Sirsi

Jun Wang

Aziz Sancar

*Above every one of knowledge, there is someone more knowledgeable.*

# NOVEL ULTRASOUND IMAGING METHODS FOR THE CHARACTERIZATION OF TISSUE MICROVASCULAR NETWORKS

by

İPEK ÖZDEMIR, BS, MS

DISSERTATION

Presented to the Faculty of

The University of Texas at Dallas

in Partial Fulfillment

of the Requirements

for the Degree of

DOCTOR OF PHILOSOPHY IN

BIOMEDICAL ENGINEERING

THE UNIVERSITY OF TEXAS AT DALLAS

May 2021

# ACKNOWLEDGMENTS

I would like to thank my advisor, Dr. Kenneth Hoyt and my committee members, Dr. Clark Meyer, Dr. Shashank Sirsi, Dr. Jun Wang, and Dr. Aziz Sancar, for their support and feedback throughout my research. I thank to all my collaborators Dr. John Eisenbrey, Dr. Philip Shaul, Dr. Mawia Khairalseed, Dr. Junjie Li, Dr. Colette Shaw, Dr. Flemming Forsberg, Dr. Girgis Obaid, Dr. Baowei Fei, also Corrine Wessner, Shreya Reddy, Jane Song, Muskan Pawar, and Kenneth Johnson for their helpful input. I thank all my lab mates individually for the collaboration and friendship. My special thanks go to Jonsson Family for the Bioengineering Fellowship and the Texas Advanced Computing Center for the computing times. I wish to express my deepest respect and thanks to the participants in my studies. My sincere thanks go to Dr. Basak Dogan, Dr. Sevan Harput, Saide-Orhan Aslan, all my friends, particularly Yasemin and Tuba, and their families, for their critical support in the beginning of my life in the USA and in Germany.

Without a doubt, my interest in medical imaging started when having conversations with my sister about her medical studies and working as a researcher in the Brain Imaging Center. I can't thank you enough, Dr. Michael Wibral and my dear sister Dr. Semra Etyemez, for that inspiring time. I wish to express my deepest gratitude Dr. Thomas Letschert, Dr. Peter Kneisel, and Dr. Ismail Naci Cangül for excellent advices throughout my professional and academic career. My most heartfelt thanks goes to my parents Nilüfer and Osman Özdemir, my sisters Aslı, Oya, and Semra for your love, guidance, patience, and care, for giving me the confidence to achieve my personal and professional growth. From bottom of my heart, thanks to Demir, Deren, Deniz, and Defne for the strong source of emotional support. I love you and I am thankful for you all.

March 2021

NOVEL ULTRASOUND IMAGING METHODS FOR THE CHARACTERIZATION OF TISSUE MICROVASCULAR NETWORKS

İpek Özdemir, PhD
The University of Texas at Dallas, 2021

Supervising Professor: Kenneth Hoyt, Chair

The structure and function of tissue microcirculation are critical in most major disease developments and in the patient-specific treatment response. Adequate quantitative characterization of tissue microvasculature may therefore assist to better understand various types of disorders, to develop new therapeutic strategies, and to monitor early response to therapy. Currently, the greatest challenge is to accurately and precisely quantify the microvascular properties in a noninvasive manner. To address this challenge, this dissertation proposes characterizing the tissue microvascular network morphology using contrast-enhanced ultrasound (CEUS). We hypothesize that the development of morphological image analysis methods using CEUS images will improve *in vivo* quantitative analysis of tissue microvascular networks for early treatment monitoring. This work demonstrates (1) the potential of CEUS-derived morphological features as a predictor of anti-cancer therapy response, (2) the development and use of multiparametric CEUS image analysis, and (3) the implementation of three-dimensional super-resolution US visualization and quantification using advanced image analysis methods.

TABLE OF CONTENTS

LIST OF FIGURES

LIST OF TABLES

# CHAPTER 1

# INTRODUCTION

## 1.1 Background and motivation

Healthy tissue microvasculature is essential for the maintenance and function in all tissues. The structure of the microvasculature is complex and consists of several cell types interacting with the environment, which is crucial for tissue homeostasis [1]–[3]. Taking the form of microvascular networks, the tissue microvasculature supplies oxygen and nutrients to different organs and removes waste via blood perfusion. Insufficient function and structure of microvascular networks indicate the development and progression of diseases. Adequate and accurate characterization of microvascular network function and structure is therefore vital to understanding various major disease types, including diabetes, cancer, and cardiovascular [4]–[6], and to assist in developing better therapeutic strategies in clinical disease management [7], [5], [8]–[15]. In this dissertation work, we used diabetes and cancer as disease models to assess the ability of microvascular characterization to answer clinically relevant research questions.

### 1.1.1 The role of microvascular networks in diabetes

Diabetes is one of the leading causes of death in the world and type 2 diabetes is present in 90% to 95% of 422 million individuals [16], [17]. Type 2 diabetes is diagnosed by the insufficient use of insulin. Insulin is delivered from the central circulation into the muscle tissue microvasculature to allow for increased disposal in peripheral tissues [8], [18], [19]. Changes in microvascular function, as well as dysfunction, contribute to peripheral insulin resistance in skeletal muscle. As illustrated in Figure 1.1, microvascular recruitment is defined as the dilatation of the microvessels,

which increases the surface area of the microvascular endothelium to carry insulin and glucose into skeletal muscle myocytes. Impaired insulin-induced microvascular recruitment in skeletal muscle contributes to insulin resistance in type 2 diabetes. In the context of diabetes, there is a close link between small vessels and disease pathogenesis [5], [20]. A deep understanding of the regulation of skeletal muscle microvascular function at a smaller scale (e.g., vessels with diameters below 300 μm) would be possible with a reliable characterization of tissue microvascular networks.

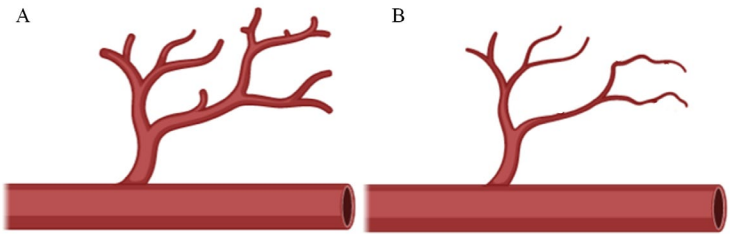


Figure 1.1. (A) Normal (dilated) versus (B) impaired microvascular recruitment. Impaired capillaries block the proper blood flow for insulin disposal in skeletal muscle, which is observed in type 2 diabetes (Created in BioRender.com).

### 1.1.2 The role of microvascular networks in cancer

Cancer resulted in 9.6 million deaths globally in 2018 and 27.5 million new cancer cases are expected by 2040 according to International Agency for Research on Cancer (IARC). Considering tumor diversity, several adaptive treatment options for unique tumor types have been developed. With a wide range of therapeutic strategies, it is important to be able to extract patient-specific tumor features for an efficient decision-making process for planning therapy. Accurately monitoring early therapy response guided by patient-specific features can reduce healthcare costs related to overtreatment. Monitoring changes in tumor size is known to be the most significant

response indicator to anti-cancer therapies when used with the Response Evaluation Criteria in Solid Tumors (RECIST) guidelines [21]. However, tracking tumor size requires several cycles of chemotherapy and a minimum of six weeks to detect the treatment response. Here, angiogenic networks can be used as a well-established biomarker for extracting patient-specific tumor features and for monitoring early tumor response to anti-cancer therapies [22]–[25]. Angiogenesis is a physiological neovascularization process that involves the formation of novel blood vessels from pre-existing vessels occurs in both health and diseased tissue [4]. As shown in Figure 1.2, compared to the healthy tissue, the microvascular networks (also known as tumor angiogenic networks) of diseased tissue is highly chaotic with disorganized, tortuous, and dilatated vessels due to an imbalance of stimulated pro-angiogenic factors [26]–[28]. Angiogenesis contributes critically to tumor growth, progression, metastasis, and therapy response [24], [26], [29], [30]. This is due to the fact that, beyond a tumor size of 1-2 mm, the angiogenic network is the only way to deliver nutrients and oxygen to sustain growth [22], to metastasize to distant sites of the body, and to deliver anti-cancer drugs to the tumor core. As illustrated in Figure 1.3, quantitative characterization of tumor angiogenic networks would enable us to capture the early response of anti-cancer therapies prior to any decreases in tumor size because alterations in tumor

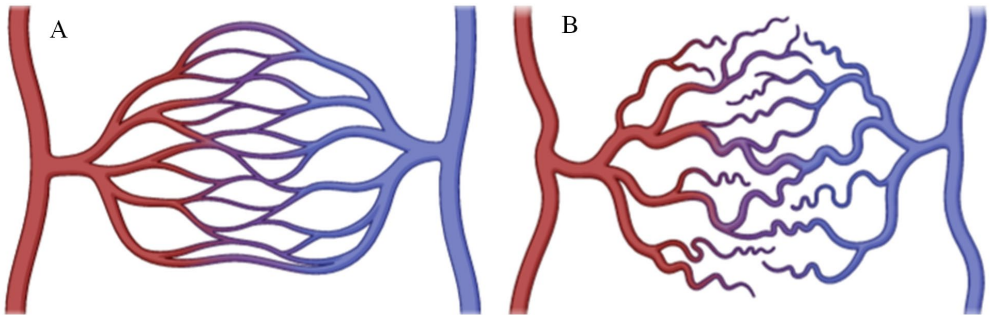


Figure 1.2. (A) Healthy versus (B) diseased (tumor) microvascular networks in tissue. (Created in BioRender.com)

microvascular networks precede alterations in tumor size. In terms of clinical assessment, histopathology based on either biopsy or a surgical resection is used as the gold standard for quantifying microvascular parameters for diagnosing cancer [7]. Nevertheless, invasiveness of histopathology is a major limitation for monitoring tumor status.

Medical imaging provides the necessary tools to noninvasively determine tissue microvascular function and treatment response [31]. There are several medical imaging modalities used in the hospital setting such as X-ray computed tomography (CT) which has a blood vessel detection limit of 400 μm [32] and magnetic resonance imaging (MRI) with a blood vessel detection limit of 300 μm. Traditional medical ultrasound (US) is the best alternative compared to

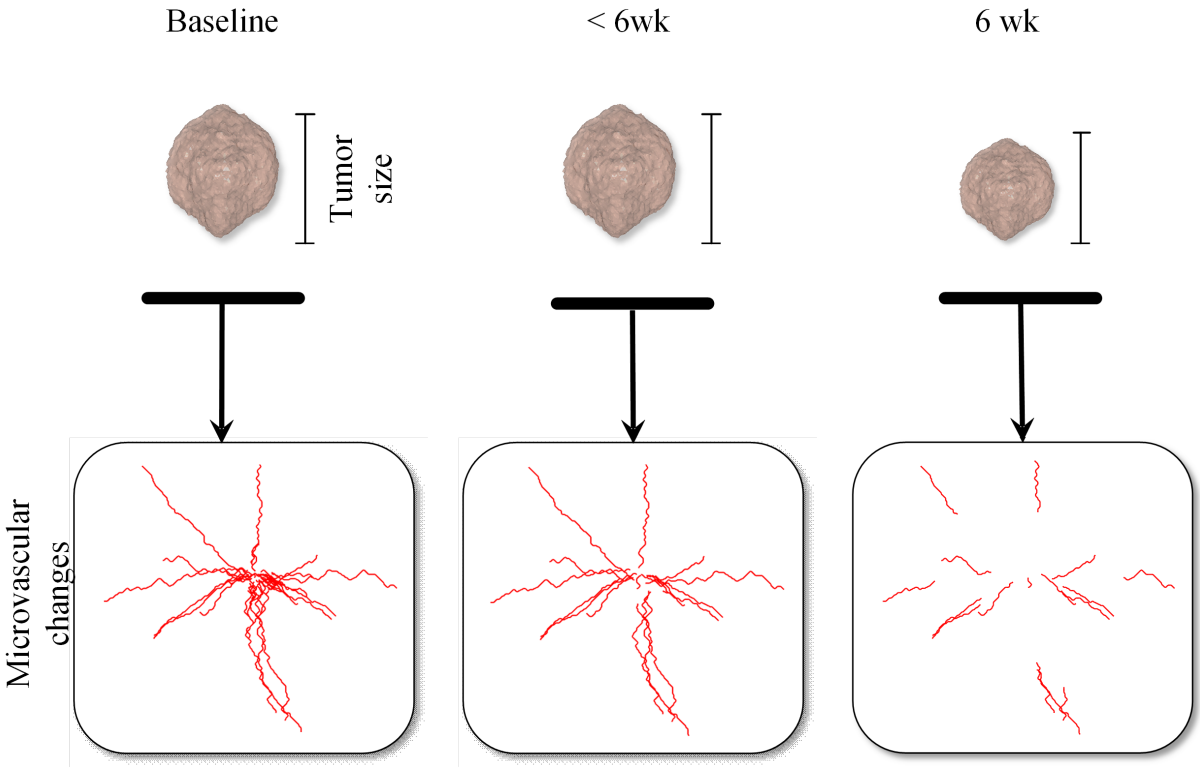


Figure 1.3. Tumor microvascular networks show earlier changes than the tumor size.

other imaging tools due to its compact size, use of nonionizing radiation, low cost, and real-time image acquisition. Additionally, US performed at clinical imaging frequencies is comparable to MRI for blood vessel imaging [31], [33].

### 1.2 Ultrasound

Medical US uses high frequencies ranging from 2 to 20 MHz, whereas the human hearing range is between 20 Hz and 20 kHz [34]. Ultrasound, as mechanical energy, is transmitted by pressure waves like from a piezoelectric element of a US transducer. Transducer elements, when made by a piezoelectric material, can convert electrical energy to mechanical energy and vice versa. After the application of electrical energy, the piezoelectric material creates mechanical vibrations that result in sound waves, also known as ultrasonic pulses. The speed of sound for soft tissue is assumed to be 1540 m/s [34]. When sound waves travel through different tissues, the speed of sound changes based in part on tissue density. Sound travels faster in more dense tissues. As the sound waves propagate through tissues of different densities and elasticities, these waves hit a smooth tissue boundary where the acoustic impedance of the first tissue is different than that of the next tissue. This creates an echo signal that is sent back to the transducer [34].

The acoustic impedance of each tissue is calculated based on the pressure and speed of sound and it indicates the resistance of the tissue to US waves [35]. The transmit time of a US wave to a tissue boundary and the return of the echo created at the boundary are used to calculate the distance between the boundary and the transducer. This allows the generation of A-line images as a function of depth using signals from each transducer element. With the activation of a group of elements at a time (usually four), all of the A-line signals from all transducer elements form a two-dimensional

grayscale image in brightness mode, which is called a B-mode image and is shown in Figure 1.4 [33].

The US wavelength determines the resolution in the axial direction while the spacing of the transducer elements dictates the resolution in the lateral direction. Longer US waves with low frequencies can penetrate deeper into the tissue but result in low-resolution images. Shorter US waves with high frequencies have increased image resolution but a lower penetration capability [34]. Although photo-acoustics [36] and functional US [37] based on ultrafast Doppler [38], [39] are helpful to improve the spatial resolution of US, these methods are not sufficient and spatial resolution needs further improvement to perform microvascular characterization at the capillary level [7].

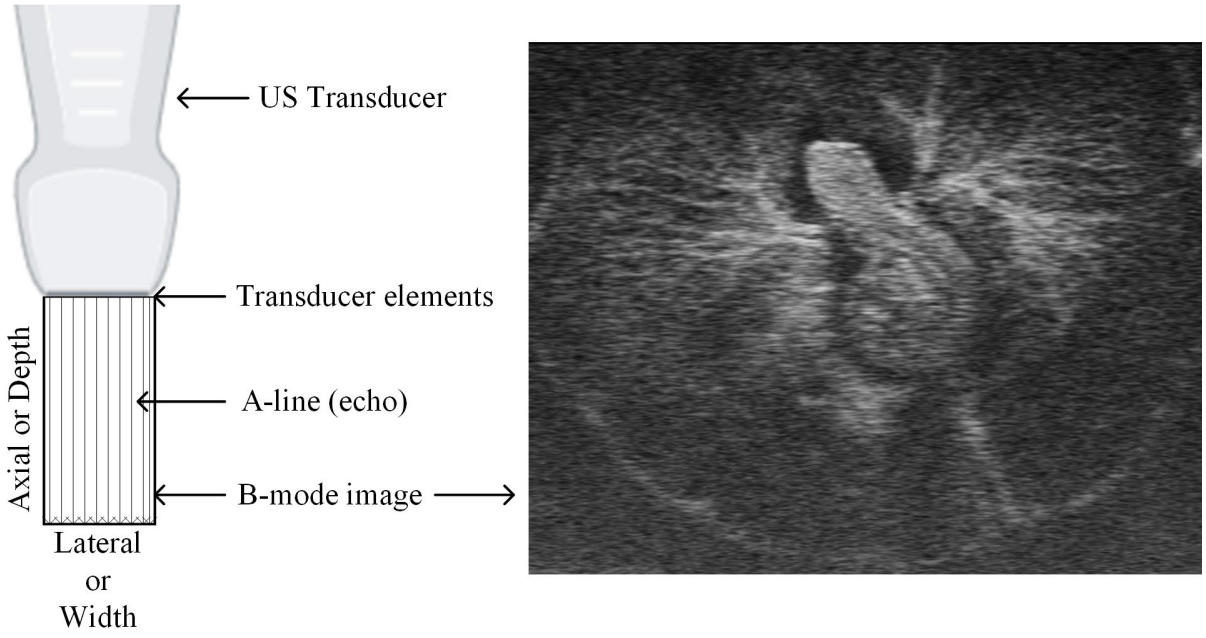


Figure 1.4. Ultrasound echo (A-line) and brightness mode (B-mode) image generated from the signal received at transducer elements (left) (Created in BioRender.com). B-mode image from a chicken embryo (right).

### 1.3 Microbubbles and contrast-enhanced ultrasound

The sensitivity of US limits to the detection of blood flow in microvessels at the capillary level. To overcome this limitation, microbubble (MB) contrast agents have been developed [40]. As illustrated in Figure 1.5, MBs have a diameter of less than 10 µm, enabling them to circulate in the microvasculature [41]. As they are different than red blood cells, lipid-shelled MBs with a nontoxic gas core can easily be detected by US imaging [41]. MBs begin oscillating when exposed to sufficiently high US pressures and these oscillations produce backscattered US signals with a nonlinear characteristic [42]. This nonlinearity allows MBs to be differentiated from the surrounding tissue due to an increased contrast-to-tissue ratio, and this allows more accurate

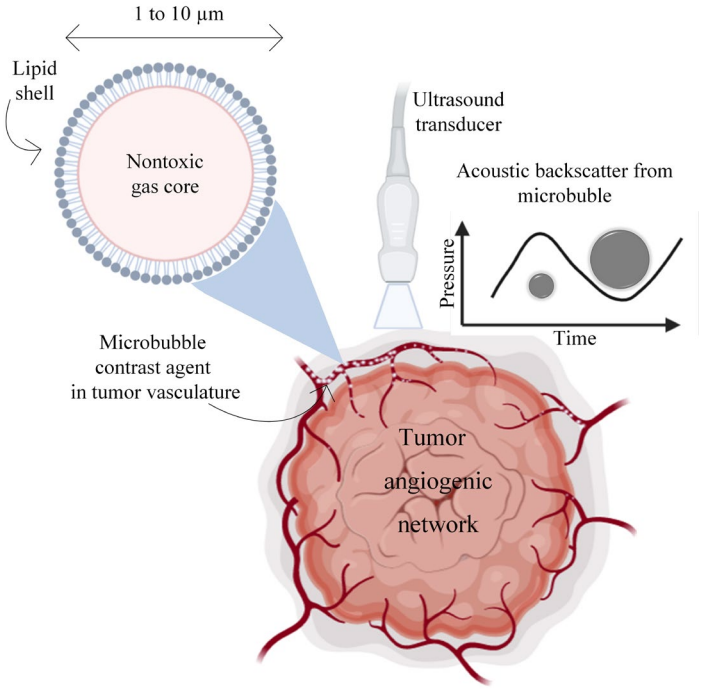


Figure 1.5. Lipid shelled and nontoxic gas core microbubble contrast agents circulating into the tumor angiogenic network and their non-linear acoustic signature shown between states of compression and rarefaction due to mechanically oscillations as pressure versus time in response to high frequency sound waves from ultrasound transducer. (Created in BioRender.com).

visualization of small vessels due to velocity-independent MB properties [43]. The recent FDA approval of MBs has enabled clinical use for patients who have contraindications to contrast agents that are used in MRI and CT [44].

Contrast-enhanced US (CEUS) is a non-invasive and safe imaging tool that does not use ionizing radiation and enables the measurement of blood flow and tissue perfusion [45]. CEUS has been widely utilized to analyze parameters of blood flow dynamics that have applications in the diagnosis and monitoring of the treatment response in diseases where tissue perfusion is vital [46]–[57]. Using CEUS, the microvascular network of the tissue can be quantitatively characterized in two ways: functionally and structurally [50], [52], [53], [58]–[62]. As shown in Figure 1.6, assuming that the MB concentration is similar to the blood concentration, blood perfusion is described by functional features (wash-in-rate, time-to-intensity-peak, peak-intensity, wash-out-rate, and area-under-the-curve). The structure of the microvascular networks is

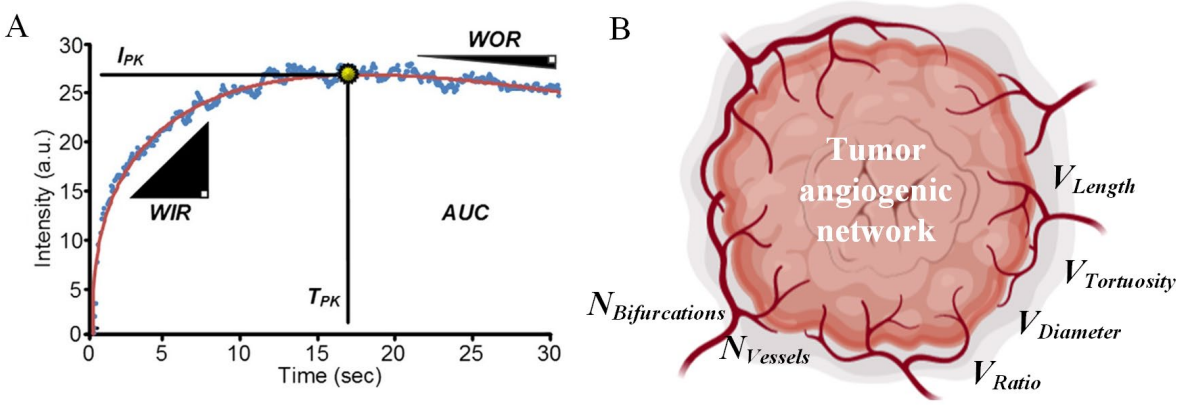


Figure 1.6. Contrast-enhanced ultrasound derived functional and structural parameters of tissue microvascular networks. Blood perfusion parameters (A) IPK: Intensity peak, WIR: Wash-in-rate, WOR: Wash-out-rate, TPK: Time to peak intensity, AUC: Area under the curve. Morphological microvascular network parameters (B) NB: Number of bifurcations, NV: Number of vessels, VL: Mean vessel length, VD: Mean vessel diameter, VT: Mean vessel tortuosity, VR: Mean vessel-to-tissue ratio or microvascular density (MVD). (Created in BioRender.com).

described by morphological features of microvessels [63] the number of vessels and bifurcations, geometric measures of mean vessel diameter and tortuosity, and vessel-to-tissue ratio or microvessel density (MVD) as a measure of compactness. Several research groups are interested in the characterization of tissue microvascular networks by morphological features for the monitoring of tumor development or regression [58], [64]–[67].

### 1.4 CEUS-derived morphological analysis and its limitations

In recent work, our group has shown that expanding the functional analysis of tissue microvascular networks with structural information may improve disease management [58]. Patient-specific features from tumor perfusion and neovascular morphology can be extracted from CEUS image sequences, and results from a pilot study with clinical data has demonstrated a promising correlation between morphological features and the pathological response to therapy [58]. These results suggest that features of both CEUS-derived blood perfusion and neovascular morphology are useful to capture early cancer response to anti-cancer therapy [58]. However,

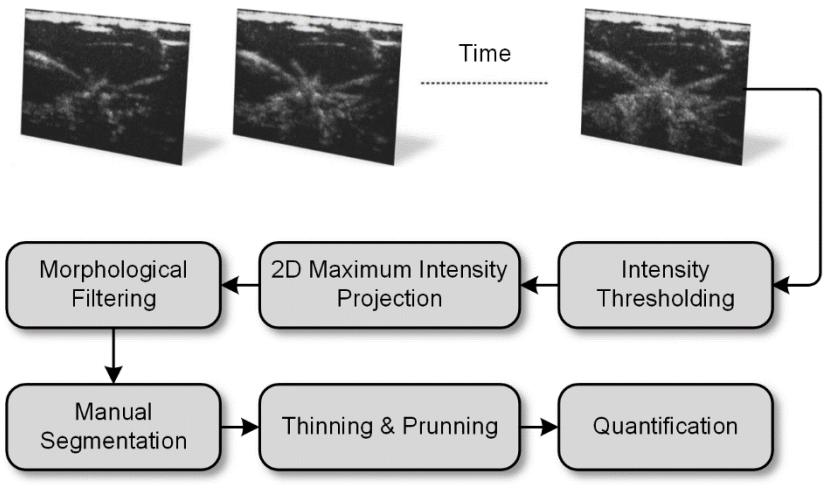


Figure 1.7. Present image processing pipeline for morphological analysis of tissue microvascular networks.

current planar CEUS imaging methods for the extraction of neovascular morphological features limits CEUS-derived morphology analysis (Figure 1.7) in a number of ways. One limitation is displacements in transducer position and subject or organ motion can have profound impacts on measurement reproducibility [46], so advanced CEUS imaging methods are necessary for motion-corrected tissue microvascular morphology analysis [68]. As examples, motion artifacts can cause a shadow around a vessel which may be seen as two vessels, or a straight vessel can be seen as a tortuous vessel. Motion-compensated CEUS-derived morphological features of microvascular networks can assist clinicians to accurately evaluate treatment response. Therefore, the **first aim** of this research is to improve the quantitative CEUS-derived image analysis pipeline with a motion correction strategy. This will enable us to investigate the clinical relevance of morphological features of tumor vascular networks as predictors of an early response to anti-cancer therapy.

Although we can achieve a high contrast-to-tissue ratio using MB contrast agents in CEUS imaging, super-resolution US (SR-US) imaging techniques provide a unique opportunity to measure vessels below 100 μm [7], [69], [70]. SR-US is based on MB localization and has been reported to achieve considerably high spatial resolution beyond the diffraction limit of the US system [71]–[73]. Increased spatial resolution and utilization of a multiscale vessel enhancement filter would enable automated segmentation and multiparametric quantification of clinically meaningful metrics for different vessel groups at multiple scales [74]–[76]. Automated algorithms are critical to enabling a reproducible, repeatable, and objective multiscale and morphological analysis using CEUS imaging [8], [19]. The **second aim** of this work is therefore to develop and evaluate a series of custom image processing algorithms for automated multiscale and morphological analysis of tissue microvascularity from CEUS images. In a multiparametric

approach, both structural and functional parameters were quantified, and CEUS-derived vessel diameters were used to perform a more sensitive perfusion analysis of tissue microvascular networks for vessel groups of different sizes. CEUS-derived multiparametric analysis may be used to assess tissue microvascular function for diseased or healthy tissue in diabetes research. Here, we also explored the utility of multiple parameters from CEUS by monitoring the early response to anti-cancer therapy validated by histological parameters.

Finally, the third limitation of the current morphological image analysis pipeline is the use of single plane (2D) CEUS-derived analysis for the characterization of tissue microvascular networks. A 2D analysis may not be sufficient for longitudinal studies because the same imaging plane from baseline imaging may not be found in follow-up imaging sessions. Specifically, within the scope of cancer, each tumor tissue has unique and heterogeneous characteristics. Structural properties of tumor angiogenic networks from preclinical and clinical CEUS studies have been reconstructed using a single imaging plane and have shown promising results [9], [32]. Nevertheless, the use of a single plane is still a major limitation because it cannot reveal the entire microvasculature or disease burden. It has been demonstrated that different imaging planes from the same tumor volume can show different results in tumor perfusion quantification, and 3D CEUS imaging approaches should be designed to capture the heterogeneous nature of tumor neovascularization more accurately [46].

Microvascular networks exist in three-dimensional (3D) space and, volumetric imaging is indispensable [18]–[21], as the adequate quantification of several important features of microvascular networks at the capillary level can only be extracted from 3D CEUS images using SR-US techniques. However, the validation of these measurements is a big challenge [65], [67],

[77]. To address this challenge, most US imaging studies have used histological markers (e.g., CD31 and CD34 staining of endothelial cells) for validating CEUS-derived microvascular measurements [22], [23]. However, there have been no validations of more geometric metrics such as vessel diameter obtained using automated algorithms and *in vivo* SR-US data. Therefore, for the **third aim** of this work, we present an automated approach for 3D SR-US imaging and morphological analysis of microvascular networks with a multimodal imaging validation. We used a chicken embryo model and co-registered optical microscopy images to validate the 3D SR-US image-derived measures.

Microvascular morphological features are extracted by a thinning algorithm and quantified by digital morphological image processing operations [58], [78], [79]. Digital morphological image processing is based on mathematical set theory and is used to describe shape of any region depicted in images [80]. Operating on binary images that consist exclusively of foreground and background values 1 and 0, morphological image processing methods are intensity invariant and rely on pixel locations. The pixel connectivity that embodies an object in the image is obtained by the pixel locations and provides information about the object's geometrical shape. The proposed research in this dissertation addresses the development of advanced CEUS imaging methods using digital morphological image analysis methods for tissue characterization and the assessment of the morphological tissue characterization in clinically relevant context.

### 1.5 Research objectives

The work presented in this dissertation examines the role of morphological features from tissue microvascular networks for CEUS-derived tissue characterization. Furthermore, this work evaluates how advanced image processing can improve the sensitivity and reliability of the

analysis by proposing an enhanced image analysis pipeline as shown in Figure 1.8. The overall goal of this research is to assess the benefits and feasibility of CEUS-derived morphological characterization of tissue microvascular networks. The Specific Aims of this work are summarized as follows:

(1) Evaluation of tumor angiogenic networks depicted in CEUS images as a predictor for anti-cancer treatment response using improved image processing via motion correction.

(2) Implementation and assessment of an SR-US-derived multiparametric quantitative analysis of microvascular changes using vessel diameter-based multiscale and multiparametric quantification.

(3) Development and validation of a new 3D SR-US imaging techniques for the visualization and quantification of microvascular networks.

Chapters 2 to 4 address Aim 1. Chapters 5 and 6 addresses Aim 2. Chapters 7 address Aim 3. Chapters 2 to 4 evaluate the structural features of tumor vascular networks using an improved

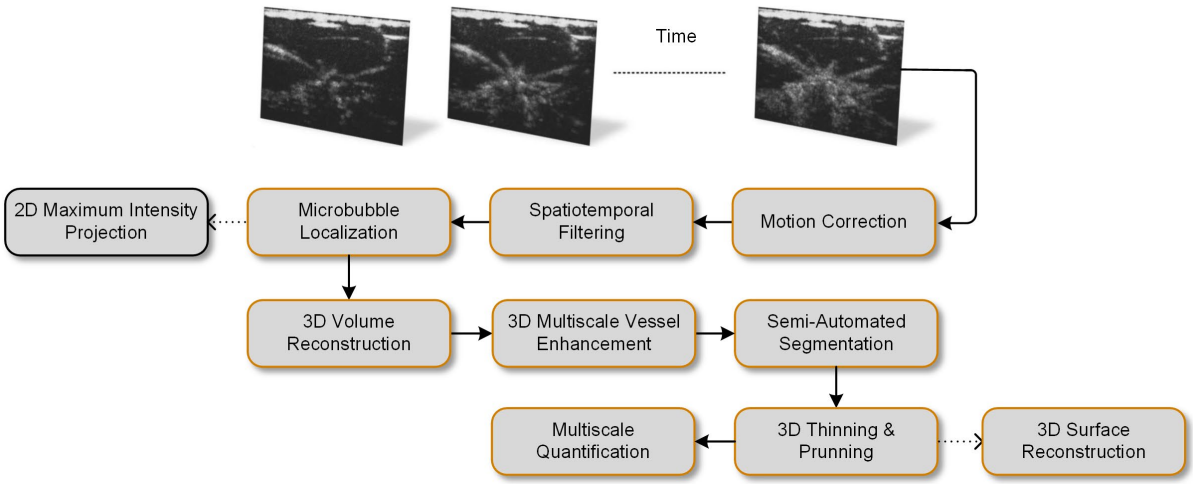


Figure 1.8. Proposed image processing pipeline for the characterization of tissue microvascular networks. Solid lines lead to multiscale quantification and dotted lines lead to different visualization methods.

image processing pipeline and presents the relationship between the predicted therapy response and pathological outcomes. We demonstrate that tumors with more complex vasculature have worse treatment response when compared to simpler networks. Chapter 5 presents the implementation of the custom software algorithm that extracts vessel diameters from microvascular networks and uses this metric for multiparametric and multiscale analysis. Although vessel diameter-based microvascular analysis has been used for diabetes research, vessel diameters have never been extracted using SR-US imaging and morphological image processing techniques to analyze microvascular recruitment based on vessel size. Our findings demonstrate that SR-US-derived structural parameters can be utilized to focus the analysis on one vessel group. We then compare results from different vessel groups with each other and show that smaller vessels are more affected by impaired microvascular recruitment. Chapter 6 shows that a similar multiparametric and multiscale morphological image analysis is also applicable for monitoring acute changes in response to targeted anti-cancer therapy. We find that morphological metrics have a positive correlation with perfusion metrics. Chapter 7 presents an advanced image processing method for volume and surface reconstruction of microvascular features from CEUS images. We show improved visualization with 3D volume rendering enables us to locate specific vessels for longitudinal monitoring. Measurements of vessel diameter are useful in reconstructing vessel surfaces, which improves visualization and quantification compared to traditional US images. We envision that the development of morphological image analysis methods using CEUS images will improve our ability to perform in *vivo* quantitative analysis of tissue microvascular networks for improved early treatment monitoring and disease progress.

## 1.6 References


[1] J. E. Beare, L. Curtis-Whitchurch, A. J. LeBlanc, and J. B. Hoying, "Microvasculature in health and disease," in *Encyclopedia of Cardiovascular Research and Medicine*, R. S. Vasan and D. B. Sawyer, Eds. Oxford: Elsevier, 2018, pp. 349–364.

[2] B. A. Corliss, C. Mathews, R. Doty, G. Rohde, and S. M. Peirce, "Methods to label, image, and analyze the complex structural architectures of microvascular networks," *Microcirculation*, vol. 26, no. 5, p. e12520, 2019.

[3] U. Blache, J. Guerrero, S. Güven, A. S. Klar, and A. Scherberich, "Microvascular networks and models, in vitro formation," in *Vascularization for Tissue Engineering and Regenerative Medicine*, 2017.

[4] N. Nishida, H. Yano, T. Nishida, T. Kamura, and M. Kojiro, "Angiogenesis in cancer," *Vascular Health and Risk Management*, vol. 2, no. 3, pp. 213–219, 2006.

[5] J. P. Glotzbach, V. W. Wong, and G. C. Gurtner, "Neovascularization in diabetes," *Expert Review of Endocrinology & Metabolism*, vol. 5, no. 1, pp. 99–111, 2010.

[6] A. J. H. M. Houben, R. J. H. Martens, and C. D. A. Stehouwer, "Assessing microvascular function in humans from a chronic disease perspective," *Journal of the American Society of Nephrology*, vol. 28, no. 12, pp. 3461–3472, 2017.

[7] K. Christensen-Jeffries *et al.*, "Super-resolution ultrasound imaging," *Ultrasound in Medicine & Biology*, vol. 46, no. 4, pp. 865–891, 2020.

[8] K. Tanigaki *et al.*, "Hyposialylated igg activates endothelial igg receptor fcγriib to promote obesity-induced insulin resistance," *The Journal of Clinical Investigation*, vol. 128, no. 1, pp. 309–322, 2016.

[9] I. Martín-Timón, C. Sevillano-Collantes, A. Segura-Galindo, and F. J. del Cañizo-Gómez, "Type 2 diabetes and cardiovascular disease: Have all risk factors the same strength?," *World Journal of Diabetes*, vol. 5, no. 4, pp. 444–470, 2014.

[10] M. A. Vincent *et al.*, "Microvascular recruitment is an early insulin effect that regulates skeletal muscle glucose uptake in vivo," *Diabetes*, vol. 53, no. 6, pp. 1418–1423, 2004.

[11] L. Womack, D. Peters, E. J. Barrett, S. Kaul, W. Price, and J. R. Lindner, "Abnormal skeletal muscle capillary recruitment during exercise in patients with type 2 diabetes mellitus and microvascular complications," *Journal of the American College of Cardiology*, vol. 53, no. 23, pp. 2175–2183, 2009.

[12] B. V. Zlokovic, "Neurovascular pathways to neurodegeneration in Alzheimer's disease and other disorders," *Nature Reviews Neuroscience*, vol. 12, no. 12, pp. 723–738, 2011.

[13] D. B. Stanimirovic and A. Friedman, "Pathophysiology of the neurovascular unit: disease cause or consequence?," *Journal of Cerebral Blood Flow & Metabolism*, vol. 32, no. 7, pp. 1207–1221, 2012.

[14] N. Weidner *et al.*, "Tumor angiogenesis: a new significant and independent prognostic indicator in early-stage breast carcinoma," *JNCI: Journal of the National Cancer Institute*, vol. 84, no. 24, pp. 1875–1887, 1992.

[15] S. M. Chadderdon *et al.*, "Temporal changes in skeletal muscle capillary responses and endothelial-derived vasodilators in obesity-related insulin resistance," *Diabetes*, vol. 65, no. 8, pp. 2249–2257, 2016.

[16] "Centers for Disease Control and Prevention. National Diabetes Statistics Report, Atlanta, GA: Centers for Disease Control and Prevention, U.S. Dept of Health and Human Service," p. 32, 2020.

[17] World Health Organization, *Global report on diabetes*. Geneva, Switzerland: World Health Organization, 2016.

[18] M. A. Vincent, L. H. Clerk, S. Rattigan, M. G. Clark, and E. J. Barrett, "Active role for the vasculature in the delivery of insulin to skeletal muscle," *Clinical and Experimental Pharmacology and Physiology*, vol. 32, no. 4, pp. 302–307, 2005.

[19] D. Dawson *et al.*, "Vascular recruitment in skeletal muscle during exercise and hyperinsulinemia assessed by contrast ultrasound," *American Journal of Physiology-Endocrinology and Metabolism*, vol. 282, no. 3, pp. E714–E720, 2002.

[20] T. R. Porter, "Capillary blood flow abnormalities in the skeletal muscle and microvascular complications in diabetes: lessons that cannot be learned from larger vessels," *Journal of the American College of Cardiology*, vol. 53, no. 23, pp. 2184–2185, 2009.

[21] E. A. Eisenhauer *et al.*, "New response evaluation criteria in solid tumours: Revised RECIST guideline (version 1.1)," *European Journal of Cancer*, vol. 45, no. 2, pp. 228–247, 2009.

[22] J. Folkman, "Angiogenesis," *Annual Review of Medicine*, vol. 57, no. 1, pp. 1–18, 2006.

[23] G. Gasparini and A. L. Harris, "Clinical importance of the determination of tumor angiogenesis in breast carcinoma: much more than a new prognostic tool," *Journal of Clinical Oncology*, vol. 13, no. 3, pp. 765–782, 1995.

[24] N. Weidner, J. P. Semple, W. R. Welch, and J. Folkman, “Tumor angiogenesis and metastasis — correlation in invasive breast carcinoma,” *New England Journal of Medicine*, vol. 324, no. 1, pp. 1–8, 1991.

[25] H. M. Shepard, “Breaching the castle walls: hyaluronan depletion as a therapeutic approach to cancer therapy,” *Frontiers in Oncology*, vol. 5, 2015.

[26] K. L. Weind, C. F. Maier, B. K. Rutt, and M. Moussa, “Invasive carcinomas and fibroadenomas of the breast: comparison of microvessel distributions--implications for imaging modalities.,” *Radiology*, vol. 208, no. 2, pp. 477–483, 1998.

[27] N. Boudreau and C. Myers, “Breast cancer-induced angiogenesis: multiple mechanisms and the role of the microenvironment,” *Breast Cancer Research*, vol. 5, p. 140, Jun. 2003.

[28] F. G *et al.*, “Angiogenesis as a prognostic indicator of survival in non-small-cell lung carcinoma: a prospective study,” *Journal of the National Cancer Institute*, 1997.

[29] R. I. Teleanu, C. Chircov, A. M. Grumezescu, and D. M. Teleanu, “Tumor Angiogenesis and Anti-Angiogenic Strategies for Cancer Treatment,” *Journal of Clinical Medicine*, vol. 9, no. 1, 2019.

[30] P. Carmeliet and R. K. Jain, “Angiogenesis in cancer and other diseases,” *Nature*, vol. 407, no. 6801, pp. 249–257, 2000.

[31] U. Sharma, K. K. A. Danishad, V. Seenu, and N. R. Jagannathan, “Longitudinal study of the assessment by MRI and diffusion-weighted imaging of tumor response in patients with locally advanced breast cancer undergoing neoadjuvant chemotherapy,” *NMR in biomedicine*, vol. 22, no. 1, pp. 104–113, 2009.

[32] T. Ap, G. An, B. Ld, Z. Ch, and A. Rd, “Three-dimensional CT angiography: a new technique for imaging microvascular anatomy.,” *Clinical Anatomy (New York, N.Y.)*, vol. 20, no. 2, pp. 116–123, 2007.

[33] S. TL. Szabo, *Diagnostic ultrasound imaging: Inside out.*, Second ed. Boston: Academic Press, 2014.

[34] J. A. Zagzebski, *Essentials of ultrasound physics*. St. Louis: Mosby.

[35] S. Suzuki, P. Gerner, and P. Lirk, “Pharmacology and physiology for anesthesia,” in *Pharmacology and Physiology for Anesthesia*, H. C. Hemmings and T. D. Egan, Eds. Philadelphia: Elsevier, 2019, pp. 390–411.

[36] L. V. Wang and S. Hu, “Photoacoustic tomography: in vivo imaging from organelles to organs,” *Science*, vol. 335, no. 6075, pp. 1458–1462, 2012.

[37] T. Deffieux, C. Demene, M. Pernot, and M. Tanter, "Functional ultrasound neuroimaging: a review of the preclinical and clinical state of the art," *Current Opinion in Neurobiology*, vol. 50, pp. 128–135, 2018.

[38] J. Bercoff *et al.*, "Ultrafast compound doppler imaging: providing full blood flow characterization," *IEEE Transactions on Ultrasonics, Ferroelectrics and Frequency Control*, vol. 58, no. 1, pp. 134–147, 2011.

[39] C. Demené *et al.*, "4D microvascular imaging based on ultrafast Doppler tomography," *NeuroImage*, vol. 127, pp. 472–483, 2016.

[40] J. Zhu *et al.*, "High frame rate contrast-enhanced ultrasound imaging for slow lymphatic flow: influence of ultrasound pressure and flow rate on bubble disruption and image persistence," *Ultrasound in Medicine & Biology*, 2019.

[41] S. Sirsi and M. Borden, "Microbubble compositions, properties and biomedical applications," *Bubble Science Engineering and Technology*, vol. 1, no. 1–2, pp. 3–17, 2009.

[42] M. x Tang and R. J. Eckersley, "Nonlinear propagation of ultrasound through microbubble contrast agents and implications for imaging," *IEEE Transactions on Ultrasonics, Ferroelectrics, and Frequency Control*, vol. 53, no. 12, pp. 2406–2415, 2006.

[43] M. A. Averkiou, M. F. Bruce, J. E. Powers, P. S. Sheeran, and P. N. Burns, "Imaging methods for ultrasound contrast agents," *Ultrasound in Medicine & Biology*, vol. 46, no. 3, pp. 498–517, 2020.

[44] T. D. Hull, A. Agarwal, and K. Hoyt, "New ultrasound techniques promise further advances in aki and ckd," *Journal of the American Society of Nephrology : JASN*, vol. 28, no. 12, pp. 3452–3460, 2017.

[45] R. Saini and K. Hoyt, "Recent developments in dynamic contrast-enhanced ultrasound imaging of tumor angiogenesis," *Imaging in Medicine*, vol. 6, no. 1, pp. 41–52, 2014.

[46] K. Hoyt, A. Sorace, and R. Saini, "Quantitative mapping of tumor vascularity using volumetric contrast enhanced ultrasound," *Investigative Radiology*, vol. 47, no. 3, pp. 167–174, 2012.

[47] K. Hoyt, A. Sorace, and R. Saini, "Volumetric contrast-enhanced ultrasound imaging to assess early response to apoptosis-inducing anti–death receptor 5 antibody therapy in a breast cancer animal model," *Journal of Ultrasound in Medicine*, vol. 31, no. 11, pp. 1759–1766, 2012.

[48] K. Hoyt *et al.*, "Determination of breast cancer response to bevacizumab therapy using contrast-enhanced ultrasound and artificial neural networks," *Journal of Ultrasound in Medicine*, vol. 29, no. 4, pp. 577–585, 2010.

[49] S. Feingold, R. Gessner, I. M. Guracar, and P. A. Dayton, "Quantitative volumetric perfusion mapping of the microvasculature using contrast ultrasound," *Investigative radiology*, vol. 45, no. 10, Oct. 2010.

[50] M. Averkiou, C. Keravnou, M. Izamis, and E. Leen, "Evaluation of perfusion quantification methods with ultrasound contrast agents in a machine-perfused pig liver," *Ultraschall in der Medizin - European Journal of Ultrasound*, vol. 39, no. 01, pp. 69–79, 2018.

[51] B. P. Davidson, J. T. Belcik, B. H. Mott, G. Landry, and J. R. Lindner, "Quantification of residual limb skeletal muscle perfusion with contrast-enhanced ultrasound during application of a focal junctional tourniquet," *Journal of Vascular Surgery*, vol. 63, no. 1, pp. 148–153, 2016.

[52] M. Doury *et al.*, "Quantification of tumor perfusion using dynamic contrast-enhanced ultrasound: impact of mathematical modeling," *Physics in Medicine & Biology*, vol. 62, no. 3, p. 1113, 2017.

[53] M. Mahoney, A. Sorace, J. Warram, S. Samuel, and K. Hoyt, "Volumetric contrast-enhanced ultrasound imaging of renal perfusion," *Journal of Ultrasound in Medicine*, vol. 33, no. 8, pp. 1427–1437, 2014.

[54] A. Sridharan *et al.*, "Perfusion estimation using contrast enhanced three-dimensional subharmonic ultrasound imaging: an in vivo study," *Investigative radiology*, vol. 48, no. 9, pp. 654–660, 2013.

[55] J. R. Eisenbrey *et al.*, "Three-dimensional subharmonic ultrasound imaging in vitro and in vivo," *Academic Radiology*, vol. 19, no. 6, pp. 732–739, Jun. 2012.

[56] S. Gummadi, M. Stanczak, A. Lyshchik, F. Forsberg, C. M. Shaw, and J. R. Eisenbrey, "Contrast-enhanced ultrasound identifies early extrahepatic collateral contributing to residual hepatocellular tumor viability after transarterial chemoembolization," *Radiology Case Reports*, vol. 13, no. 3, pp. 713–718, 2018.

[57] K. Nam, M. Stanczak, F. Forsberg, C. M. Shaw, and J. R. Eisenbrey, "Evaluation of hepatocellular carcinoma transarterial chemoembolization using 3d contrast enhanced ultrasound time-intensity curve analysis," in *2017 IEEE International Ultrasonics Symposium (IUS)*, 2017, pp. 1–4.

[58] K. Hoyt, H. Umphrey, M. Lockhart, M. Robbin, and A. Forero-Torres, "Ultrasound imaging of breast tumor perfusion and neovascular morphology," *Ultrasound in Medicine & Biology*, vol. 41, no. 9, pp. 2292–2302, 2015.

[59] E. Frampas, N. Lassau, M. Zappa, M.-P. Vullierme, S. Koscielny, and V. Vilgrain, "Advanced hepatocellular carcinoma: early evaluation of response to targeted therapy and

prognostic value of perfusion ct and dynamic contrast enhanced-ultrasound. preliminary results," *European journal of radiology*, 2013.

[60] A. El Kaffas *et al.*, "Spatial characterization of tumor perfusion properties from 3d dce-us perfusion maps are early predictors of cancer treatment response," *Scientific Reports*, vol. 10, no. 1, pp. 1–11, 2020.

[61] N. Lassau, L. Chami, B. Benatsou, P. Peronneau, and A. Roche, "Dynamic contrast-enhanced ultrasonography (DCE-US) with quantification of tumor perfusion: a new diagnostic tool to evaluate the early effects of antiangiogenic treatment," *European Radiology Supplements*, vol. 17, no. 6, pp. 89–98, 2007.

[62] W. M. Thaiss *et al.*, "Dose optimization of perfusion-derived response assessment in hepatocellular carcinoma treated with transarterial chemoembolization: comparison of volume perfusion ct and iodine concentration," *Academic Radiology*, 2018.

[63] R. K. Jain, "Determinants of tumor blood flow: a review," *Cancer Research*, vol. 48, no. 10, pp. 2641–2658, 1998.

[64] E. Bullitt *et al.*, "Tumor therapeutic response and vessel tortuosity: preliminary report in metastatic breast cancer.," *International Conference on Medical Image Computing and Computer-Assisted Intervention*, vol. 9, pp. 561–568, 2006.

[65] R. C. Gessner, S. R. Aylward, and P. A. Dayton, "Mapping microvasculature with acoustic angiography yields quantifiable differences between healthy and tumor-bearing tissue volumes in a rodent model," *Radiology*, vol. 264, no. 3, pp. 733–740, 2012.

[66] S. R. Rao, S. E. Shelton, and P. A. Dayton, "The 'fingerprint' of cancer extends beyond solid tumor boundaries: assessment with a novel ultrasound imaging approach," *IEEE Transactions on Biomedical Engineering*, vol. 63, no. 5, pp. 1082–1086, 2016.

[67] F. Lin, S. E. Shelton, D. Espíndola, J. D. Rojas, G. Pinton, and P. A. Dayton, "3-D Ultrasound localization microscopy for identifying microvascular morphology features of tumor angiogenesis at a resolution beyond," *Theranostics*, vol. 7, no. 1, pp. 196–204, 2017.

[68] S. Harput *et al.*, "Two-stage motion correction for super-resolution ultrasound imaging in human lower limb," *IEEE Transactions on Ultrasonics, Ferroelectrics, and Frequency Control*, vol. 65, no. 5, pp. 803–814, 2018.

[69] S. W. Hell and J. Wichmann, "Breaking the diffraction resolution limit by stimulated emission: stimulated-emission-depletion fluorescence microscopy," *Opt Lett*, vol. 19, no. 11, pp. 780–782, Jun. 1994.

[70] E. Betzig *et al.*, "Imaging intracellular fluorescent proteins at nanometer resolution," *Science (New York, N.Y.)*, vol. 313, no. 5793, pp. 1642–1645, 2006.

[71] K. Christensen-Jeffries, R. J. Browning, M.-X. Tang, C. Dunsby, and R. J. Eckersley, "In vivo acoustic super-resolution and super-resolved velocity mapping using microbubbles," *IEEE Transactions on Medical Imaging*, vol. 34, no. 2, pp. 433–440, 2015.

[72] C. Errico *et al.*, "Ultrafast ultrasound localization microscopy for deep super-resolution vascular imaging," *Nature*, 2015.

[73] M. A. O'Reilly and K. Hynynen, "A super-resolution ultrasound method for brain vascular mapping," *Medical Physics*, vol. 40, no. 11, 2013.

[74] D. Ghosh *et al.*, "Super-resolution ultrasound imaging of skeletal muscle microvascular dysfunction in an animal model of type 2 diabetes," *Journal of Ultrasound in Medicine*, vol. 38, no. 10, pp. 2589–2599, 2019.

[75] M. G. Clark, "Impaired microvascular perfusion: a consequence of vascular dysfunction and a potential cause of insulin resistance in muscle," *American Journal of Physiology - Endocrinology and Metabolism*, vol. 295, no. 4, pp. E732–E750, 2008.

[76] C. Manrique and J. R. Sowers, "Insulin resistance and skeletal muscle vasculature: significance, assessment and therapeutic modulators," *Cardiorenal Medicine*, vol. 4, no. 3–4, pp. 244–256, 2014.

[77] R. C. Gessner, C. B. Frederick, F. S. Foster, and P. A. Dayton, "Acoustic angiography: a new imaging modality for assessing microvasculature architecture," *International Journal of Biomedical Imaging*, vol. 2013, pp. 1–9, 2013.

[78] L. Lam, S.-W. Lee, and C. Y. Suen, "Thinning methodologies-a comprehensive survey," *IEEE Transactions on Pattern Analysis and Machine Intelligence*, vol. 14, no. 9, pp. 869–885, 1992.

[79] J. R. Eisenbrey, N. Joshi, J. K. Dave, and F. Forsberg, "Assessing algorithms for defining vascular architecture in subharmonic images of breast lesions," *Physics in Medicine and Biology*, vol. 56, no. 4, pp. 919–930, 2011.

[80] R. C. Gonzalez and R. E. Woods, *Digital Image Processing*, 4th ed. New York, NY, USA: Pearson, 2018.

# CHAPTER 2

# IMPROVED QUANTITATIVE CONTRAST-ENHANCED ULTRASOUND IMAGING OF HEPATOCELLULAR CARCINOMA RESPONSE TO TRANSARTERIAL CHEMOEMBOLIZATION

Authors – Ipek Oezdemir[1], Colette Shaw[2], John R. Eisenbrey[2], Kenneth Hoyt[1,3]

[1]The Department of Bioengineering, BSB 11
The University of Texas at Dallas
800 West Campbell Road
Richardson, TX 75080-3021

[2]The Department of Radiology, East Falls
Thomas Jefferson University
4201 Henry Ave
Philadelphia, PA 19144

[3]The Department of Radiology
The University of Texas Southwestern Medical Center
1801 Inwood Rd
Dallas, TX 75390

Author contribution: Ipek Ozdemir (myself) was responsible for the experimental design, the data analysis, and the manuscript preparation presented here.

The purpose of this research project was to improve the quantification of microvascular networks depicted in contrast-enhanced ultrasound (CEUS) images of human hepatocellular carcinoma (HCC) using a two-stage motion correction method. Due to limited anatomical information in CEUS images, grayscale B-mode ultrasound (US) data is preferred when estimating tissue motion. Transformation functions derived from the B-mode data are one solution for registering a dynamic sequence of CEUS images. Microvessel density (MVD) can then be calculated from both the original and motion corrected CEUS images as the ratio of the number of contrast-enhanced image pixels with a value greater than zero to the number of pixels of the entire tumor space. Using US images of HCC before and after treatment with transarterial chemoembolization, results revealed that affine and non-rigid motion correction improves visualization and quantitative analysis of clinical data. Using the correlation coefficient (CC) between CEUS frames as metric of tissue motion, our motion correction strategy produced a 20% increase in the average CC from motion corrected frames compared to the data before correction ($p < 0.001$). Furthermore, enhanced visualization of microvascular networks in the treated liver tumor space may improve determination of treatment efficacy and need for any repeat procedures.

## 2.1 Introduction

Dynamic contrast-enhanced ultrasound (CEUS) is a noninvasive imaging modality commonly used to quantify tissue microvascular networks, e.g., tumor angiogenesis [1], [2]. Analysis of tissue microvascular structures depicted in CEUS images of cancerous tissue is an emerging strategy for determining an early response to anticancer treatment [3]–[6]. During ultrasound (US) imaging, inevitable motion artifacts caused by probe motion, patient breathing, and cardiac pulsations, can degrade the accuracy of any image quantification. To improve image quantification, these motion artifacts should be properly addressed and removed, which is a process known as motion correction.

One motion correction strategy that has been applied to magnetic resonance (MR) images uses non-rigid registrations to align images with motion artifacts to a preselected reference frame [7]. In short, a global motion correction strategy first registers images by applying a series of affine transformations, e.g., rotations, translations, shearing, and scaling. To then correct for local motion, free-form deformations derived from basis spline (B-spline) functional analysis were used. A similarity measure defined by mutual information, e.g., cross-correlation coefficient (CC), can be used to help evaluate the degree of image registration (i.e., corrected motion). A more recent study demonstrated that this non-rigid registration approach to motion correction can be used to improve the quality of clinical CEUS images and quantification [8].

Another strategy for motion estimation and correction in US images is to discard the frames based on correlation between two consecutive frames [9]. Assuming that the frames have one dominant motion artifact, such as due to respiratory or cardiac motion, the image correction values can be computed and analyzed. Assuming that a lower CC is observed during certain periods of

the respiratory or cardiac cycles, these frames can be discarded to help eliminate any CEUS image frames corrupted by subject motion. In this paper, we demonstrate improved quantification of CEUS images using a combination of the two varying methods mentioned above.

## 2.2 Materials and Methods

### 2.2.1 Ultrasound Imaging

A retrospective analysis of CEUS images of human HCC was performed ($N$ = 8) [10]. All US examinations were performed using a Logiq E9 scanner equipped with a C1-6-D transducer (GE Healthcare, Wauwatosa, WI). After acquiring baseline images, subjects received a bolus injection of 0.2–0.3 ml of a microbubble (MB) contrast agent (Definity, Lantheus Medical Imaging, N Billerica, MA) followed by a 10 ml saline flush. CEUS imaging was performed using a dual imaging mode, enabling side-by-side visualization of the grayscale B-mode and CEUS images at a rate of 8 to 9 frames per sec. Each subject underwent CEUS exams at three time points: prior to a transarterial chemoembolization (TACE) treatment procedure, 1 to 2 wk post TACE, and again about 4 wk post TACE treatment. During scanning, the transducer was being rotated for 90° after the peak intensity point was reached and sweep through the region to be able to see all the other sides of the tumor region. Our analysis of the microvascular morphology was restricted by only one plane, so we discarded the frames after 30 to 40 sec as these contained mostly out-of-plane motions.

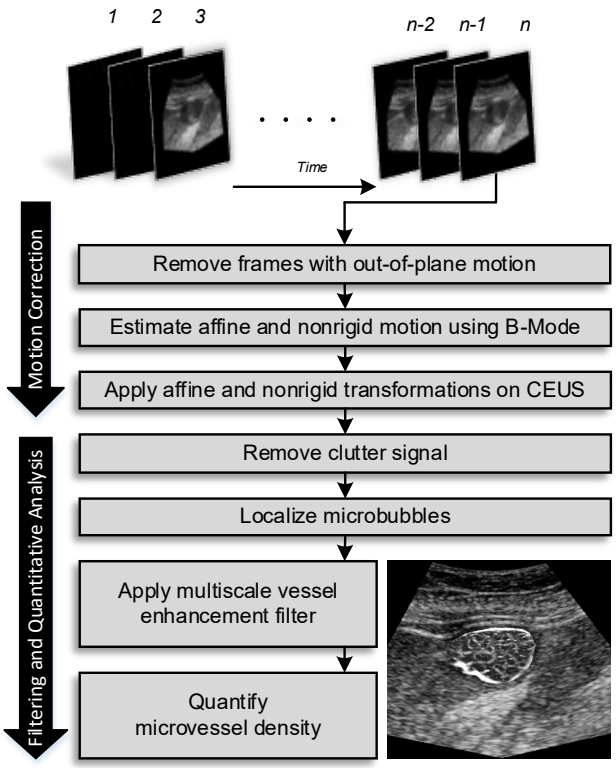


Figure 2.1. Diagram of the data processing strategy used for the improved quantification of microvascular structures depicted in contrast-enhanced ultrasound (CEUS) images.

### 2.2.2 Image Processing

CEUS images of HCC corrupted with motion artifacts caused by respiratory, cardiac, and probe motions were analyzed. B-Mode US images were used for motion estimation. As seen in Figure 2.1, the first step in the image processing pipeline was to remove the frames with out-of-plane motion prior to in-plane motion correction. According to the scanning protocol, consistent imaging was performed on plane at midline of lesion of interest for at least 10 sec after peak contrast enhancement was reached (about 30 sec after injection) was maintained. For this reason, the first 255 – 355 in-plane frames were remaining after we discarded the frames with out-of-plane motions. Full cine length was not the same across all the time points and subjects. Therefore, the

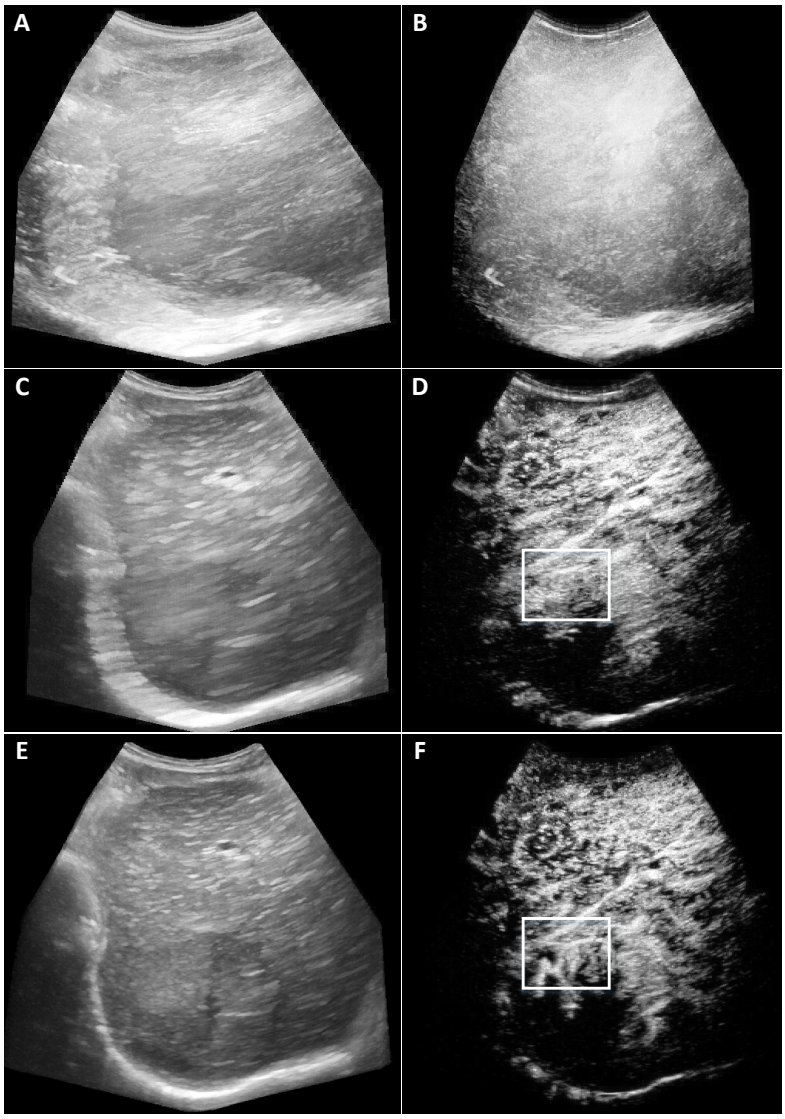


Figure 2.2. Original (A-B), out-of-plane frames eliminated (C-D), the resulting motion corrected (E-F) B-Mode (left) and CEUS (right) maximum intensity projection (MIP) images from 787, 255, and 255 frames respectively. Image size was 649x585 pixels. Highlighted changes in the white box did not contain any vessels for the original image while the corrected image shows the vessels, bifurcations, and tortuosity.

number of frames that were discarded was not the same for all subjects and time points. As an example, the images in the second row of Figure 2.2 were created using maximum intensity projection (MIP) of the first 255 in-plane frames out of 787 frames. Here, the first frame of each

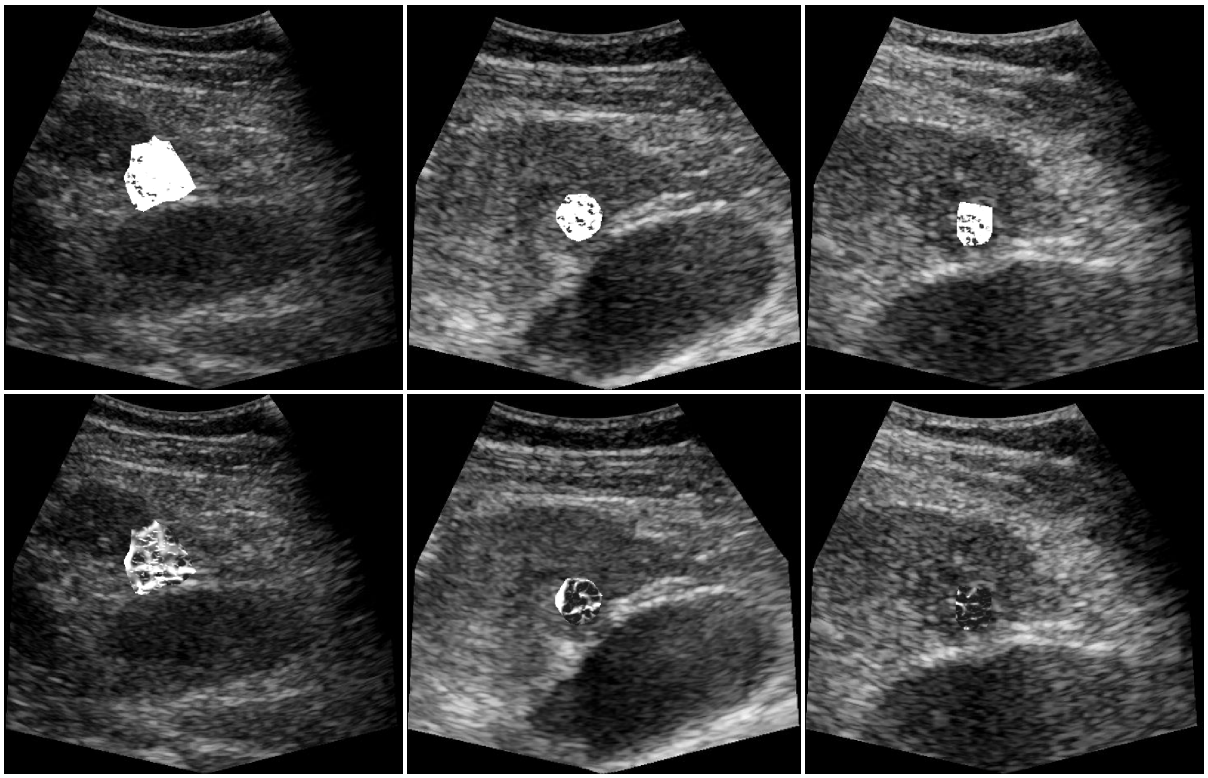

Figure 2.3. Vessel enhancement from region-of-interests (ROIs) were performed on the MIP of 255 frames and overlaid on a single B-Mode image for baseline (left), after two-wk (middle), and four-wk (right). The complete response from the clinical results were in line with the images (bottom). Dense vascularity on the baseline decreased after two- and four-wk. These temporal changes of the vascular morphology were not observable from the images (top) corrupted with motion.

image sequence was chosen as a reference frame and all subsequent frames were motion corrected and registered to that reference. Next, affine transformations were used to compensate for global motion and free-form deformations adjusted the motion on local regions in CEUS images. We customized the parts of the MATLAB code from [11] for using parallel processing in Texas Advanced Computing Center (TACC). The limited memory Broyden Fletcher Goldfarb Shanno (L-BFGS) optimization was used to minimize the squared pixel distance (SD) between static and moving images. Subsequently, both, original and motion corrected images were filtered to remove

clutter signal using a singular value filter (SVF) which was based on principle component analysis signal separation for medical US images [12] and to localize MBs using the methods from [13]. In addition, a multiscale vessel enhancement filter was applied for better visualization of vessels, e.g., tubular structures in the image were enhanced [14]. As a therapy response metric, we quantified the microvessel density (MVD) that should indicate the changes in the tumor vasculature. MVD was calculated as follows:

$$\text{MVD} = Vp \,/\, MN \tag{2.1}$$

where $V_P$ was used as an estimate of number of vascular points and $M$ and $N$ were the axial and lateral dimensions of the region of interest (ROI) [6].

### 2.2.3 Evaluation Metric

The CC was used as performance metric to demonstrate improvement after motion correction of CEUS images and given by:

$$CC = \frac{\sum_m \sum_n (A_{mn} - \bar{A})(B_{mn} - \bar{B})}{\sqrt{(\sum_m \sum_n (A_{mn} - \bar{A})^2)(\sum_m \sum_n (B_{mn} - \bar{B})^2)}} \tag{2.2}$$

where $A$ and $B$ are images, $m$ and $n$ are pixel coordinates, and $\bar{A}$ , $\bar{B}$ are the mean intensity values $A$ and $B$, respectively. MVD levels were then calculated to see if these will reflect the therapy response assessed by clinical results [10].

## 2.3 Results

From 8 subjects, the patient outcome of 3 subjects were incomplete and 5 subjects of them were complete response assessed by clinical criteria and MR imaging results [10]. Representative B-mode and CEUS images of human HCC are depicted in Figure 2.2. Before motion correction, vessels were not visible in certain image regions. Note that subject motion is akin to image

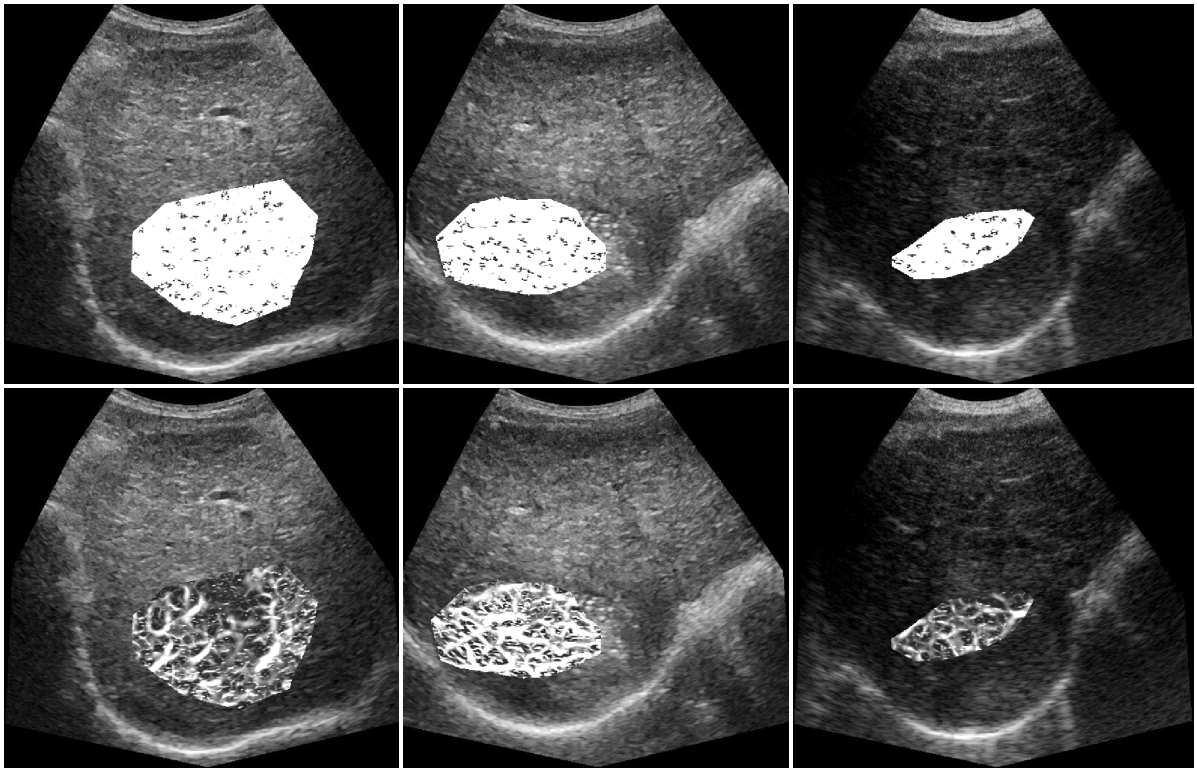

Figure 2.4. Vessel enhancement of ROIs was performed on the MIP of 255 frames and overlaid on a single B-Mode images for baseline (left), after two-wk (middle), and four-wk (right). Images (top) contain motion artifacts. The incomplete response from the clinical results was reflected on the images (bottom). Densely vascularized tumor on the baseline was preserved after two and four wk.

smoothing (blurring) and masks some smaller vascular structures. However, after applying our motion correction strategy, more vascular structures were visible, allowing for quantification of

certain morphological features, e.g., vessel length, number of bifurcations, vessel tortuosity and diameter.

Longitudinal CEUS images from an example of a complete HCC response to TACE treatment was depicted in Figure 2.3. Relative changes in MVD values were more pronounced after motion correction of the CEUS images due to a fundamental improvement in vascular network visualization. Figure 2.4 shows images from a representative incomplete response. The vascularity in the ROI from original images have high intensity values in every pixel because of motion artifacts. The motion corrected version of the same ROI has clearer visualized vascular network. Compared to the images in Figure 2.2., the motion corrected images from Figure 2.3 and Figure 2.4 had higher intensity values, because the latter were processed with the vessel enhancement filter after motion correction.

Results from complete response subjects showed rapidly decreasing MVD values after TACE treatment at the second and fourth wk when using motion corrected images. MVD values 0.92, 0.82, 0.80 at first, second, and fourth wk from the original data while motion corrected MVDs,

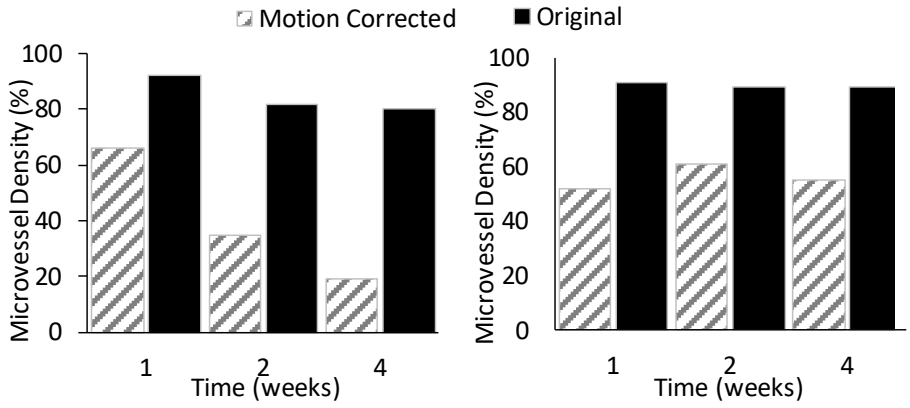


Figure 2.5. Higher relative changes in MVD values for complete response subject when motion was corrected (left). Consistent MVD values indicating the incomplete response to the therapy (right).

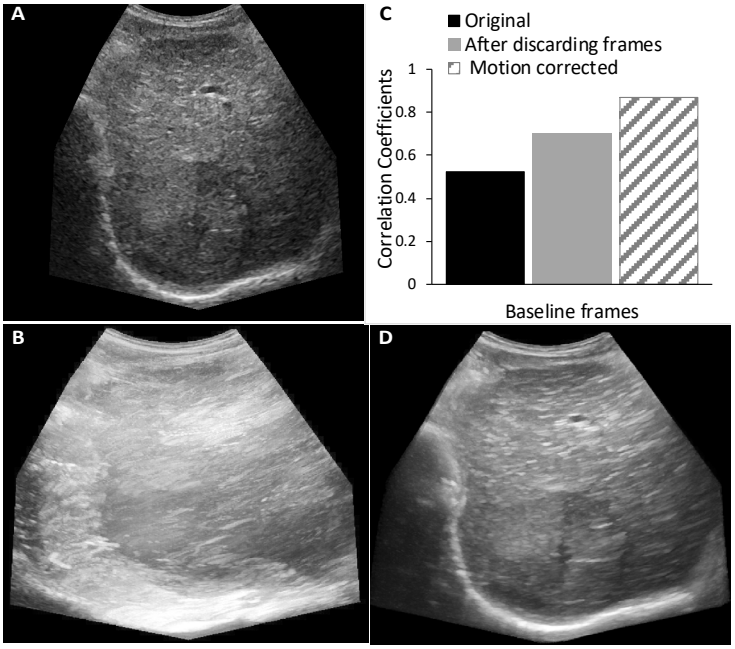


Figure 2.6. Single B-Mode as reference (A), MIP before (B) and after (D) motion correction. The CC values (C) were obtained for original full number of frames (787), for the frames (255) after discarding the out-of-plane motion, and for the corrected frames (255).

e.g., 0.66, 0.35, 0.19 were in line with the therapy response as it can be seen in Figure 2.5. The incomplete response subjects' original MVD values were 0.91, 0.89, 0.89, while motion corrected MVDs were first decreasing and then increasing, e.g., 0.52, 0.61, 0.55, that can explain the incomplete therapy response.

Figure 2.6 illustrates improved CC for each time point from the representative subject. CCs between reference frame and subsequent frames of the entire cine were computed for corrected and noncorrected cines. Higher CC values represent higher similarities between the ROIs from the images.

Finally, CC values from all frames of the eight subjects imaged at three time points each, were taken and compared with and without motion correction. The summary statistics from what a two-

sample t-test was performed resulted in a significant ($p < 0.001$) difference between all original and motion corrected frames based on CC values.

## 2.4 Conclusion

After TACE treatment, detection of intratumoral vascular structures during CEUS imaging can help inform additional procedures. Overall, motion correction of CEUS images improves visualization of the tumor microvasculature and any subsequent quantification of these structures. Future work will investigate the relationship between tumor microvascular morphology features at baseline and following both partial and complete TACE treatment successes.

## 2.5 References


[1] R. Saini and K. Hoyt, "Recent developments in dynamic contrast-enhanced ultrasound imaging of tumor angiogenesis," *Imaging Med*, vol. 6, no. 1, pp. 41–52, 2014.

[2] K. Hoyt, A. Sorace, and R. Saini, "Quantitative mapping of tumor vascularity using volumetric contrast-enhanced ultrasound," *Invest Radiol*, vol. 47, no. 3, pp. 167–174, 2012.

[3] K. Hoyt *et al.*, "Determination of breast cancer response to bevacizumab therapy using contrast-enhanced ultrasound and artificial neural networks," *J Ultrasound Med*, vol. 29, no. 4, pp. 577–585, 2010.

[4] D. Ghosh *et al.*, "Monitoring early tumor response to vascular targeted therapy using super-resolution ultrasound imaging," *Proc IEEE Ultrason Symp*, pp. 1–4, 2017.

[5] K. Hoyt, A. Sorace, and R. Saini, "Volumetric contrast-enhanced ultrasound imaging to assess early response to apoptosis-inducing anti-death receptor 5 antibody therapy in a breast cancer animal model," *J Ultrasound Med*, vol. 31, no. 11, pp. 1759–1766, 2012.

[6] K. Hoyt, H. Umphrey, M. Lockhart, M. Robbin, and A. Forero-Torres, "Ultrasound imaging of breast tumor perfusion and neovascular morphology," *Ultrasound in medicine & biology*, vol. 41, no. 9, pp. 2292–2302, 2015.

[7] D. Rueckert, L. I. Sonoda, C. Hayes, D. L. G. Hill, M. O. Leach, and D. J. Hawkes, "Nonrigid registration using free-form deformations: application to breast MR images," *IEEE Transactions on Medical Imaging*, vol. 18, no. 8, pp. 712–721, 1999.

[8] S. Harput *et al.*, "Two-stage motion correction for super-resolution ultrasound imaging in human lower limb," *IEEE Transactions on Ultrasonics, Ferroelectrics, and Frequency Control*, vol. 65, no. 5, pp. 803–814, 2018.

[9] J. Foiret, H. Zhang, T. Ilovitsh, L. Mahakian, S. Tam, and K. W. Ferrara, "Ultrasound localization microscopy to image and assess microvasculature in a rat kidney," *Scientific Reports*, vol. 7, no. 1, 2017.

[10] K. Nam *et al.*, "Evaluation of hepatocellular carcinoma transarterial chemoembolization using quantitative analysis of 2d and 3d real-time contrast enhanced ultrasound," *Biomedical Physics & Engineering Express*, vol. 4, no. 3, p. 035039, 2018.

[11] D. J. Kroon, "B-spline Grid, Image and Point based Registration," *Mathworks*, 2011.

[12] F. W. Mauldin, D. Lin, and J. A. Hossack, "The singular value filter: a general filter design strategy for pca-based signal separation in medical ultrasound imaging," *IEEE Transactions on Medical Imaging*, vol. 30, no. 11, pp. 1951–1964, 2011.

[13] D. Ghosh *et al.*, "Super-resolution ultrasound imaging of the microvasculature in skeletal muscle: a new tool in diabetes research," *Proc IEEE Ultrason Symp (IUS)*, pp. 1–4, 2017.

[14] A. F. Frangi, W. J. Niessen, K. L. Vincken, and M. A. Viergever, "Multiscale vessel enhancement filtering,"

# CHAPTER 3

# TUMOR VASCULAR NETWORKS AS PREDICTORS FOR TRANSARTERIAL CHEMOEMBOLIZATION TREATMENT RESPONSE OF HEPATOCELLULAR CANCER

Authors – Ipek Oezdemir[1], Corrine E. Wessner[2], Colette Shaw[2], John R. Eisenbrey[2], Kenneth Hoyt[1,3]

[1]The Department of Bioengineering, BSB 11
The University of Texas at Dallas
800 West Campbell Road
Richardson, TX 75080-3021

[2]The Department of Radiology, East Falls
Thomas Jefferson University
4201 Henry Ave
Philadelphia, PA 19144

[3]The Department of Radiology
The University of Texas Southwestern Medical Center
1801 Inwood Rd
Dallas, TX 75390

*Adapted from *Ultrasound Med Biol*, **46**, Ipek Oezdemir, Corrine E. Wessner, Colette Shaw, John R. Eisenbrey, Kenneth Hoyt, Tumor Vascular Networks as predictor for Transarterial Chemoembolization Treatment Response of Hepatocellular Cancer, 2276-86, Elsevier, 2020.

Author contribution: Ipek Ozdemir (myself) was responsible for the experimental design, the data analysis, and the manuscript preparation presented here.

In this study, we present an image processing and analysis approach for the prediction of hepatocellular carcinoma (HCC) response to transarterial chemoembolization (TACE) treatment using clinical CEUS images and known pathological responses. This method focuses on addressing the challenges of CEUS by incorporating a two-stage motion correction strategy, clutter signal removal, vessel enhancement at multiple scales, and machine learning for predictive modeling. The morphological features, namely, number of vessels (NV), number of bifurcations (NB), vessel to tissue ratio (VR), mean vessel length, tortuosity, and diameter from tumor architecture were quantified from CEUS images of 36 HCC patients before TACE treatment. Our analysis revealed that NV, NB, and VR are the dominant features for the prediction of long term TACE response. The model obtained an accuracy of 86% with a sensitivity and specificity of 89% and 82%, respectively. Reliable prediction of the TACE therapy response using CEUS-derived image features may help to provide personalized therapy planning, which will ultimately improve patient outcomes.

## 3.1 Introduction

Hepatocellular carcinoma (HCC) is the fifth most prevalent cancer worldwide [1] and the third most common cause of cancer mortality [2]. Liver function and the tumor location and stage are considered when planning treatment options, such as surgical resection, transplantation, locoregional treatment, or systemic therapy [3]. Patients with unresectable tumors are often candidates for a locoregional treatment option including drug-eluting bead transarterial chemoembolization (DEB-TACE or TACE) or transarterial radioembolization (TARE), which is not embolic. In the TACE procedure, polyvinyl alcohol beads or ethiodol are used to deliver chemotherapeutic agents into the tumor angiogenic network via a catheter placed in the tumor-feeding hepatic artery [4]. After the embolization, the beads start releasing the chemotherapeutic drug slowly into the tumor vasculature [5]. Successful treatment is defined by the complete occlusion of the tumor vasculature, but up to 65-75% of tumors show residual blood flow, and in this case, repeat TACE or alternative therapies are required [6].

Monitoring TACE therapy response is performed with contrast-enhanced magnetic resonance imaging (CE-MRI) or with contrast-enhanced computed tomography (CECT) [3]. The standard recommended time for the follow-up imaging is 4 to 6 weeks because both imaging modalities have limitations assessing the residual blood flow or lack thereof before this time point [3], [5]–[7]. Contrast-enhanced ultrasound (CEUS) is a low cost alternative to CECT and CE-MRI, and provides accurate evaluations of residual blood flow at 1 to 2 weeks post TACE treatment qualitatively [6] and quantitatively [8], [9]. Quantifications of TACE therapy response using CEUS are performed with blood perfusion parameters that provide functional information about the blood flow dynamics after the TACE treatment.

Structural information from the architecture of the tumor angiogenic network can be characterized by their morphological features [10]. These morphological features have also been shown as biomarkers for early response to anticancer therapy for different tumor models [11]–[19]. However, a more efficient HCC management would benefit from the information about future TACE response at the time of the treatment planning phase (in which case percutaneous ablation or TARE may be opted for as an alternative). Hence, a current clinical challenge is to determine which patients will respond to TACE as effective delivery of the embolic material may be influenced by the tumor vascular supply.

We hypothesize that CEUS image-derived tumor vascular morphology features may provide predictive information for efficient TACE therapy planning and HCC patient management. Challenges for improved quantification of tumor vascular morphology in abdominal imaging include the high amount of motion artifacts that limit direct quantification of the structural information and the tissue signal, i.e., clutter signal, which limits the vascular resolution reconstructed by the ultrasound (US) contrast agent (microbubble, MB) signal [10]. Another restriction is the lost visualization of small vessels in the tumor vasculature when focusing only on large vessels or vice versa during the vessel segmentation process [20]. Finally, an automated image processing pipeline is useful for reproducible results and clinical translation. Herein we investigate the potential use of abdominal CEUS and advanced image processing algorithms for predicting HCC response to TACE treatment.

## 3.2 Materials and Methods

### 3.2.1 Ultrasound Imaging

A retrospective analysis of CEUS images of human HCC was performed ($N$ = 36). Data was acquired as part of an ongoing IRB approved multi-center trial (NCT# 02764801) in which all participants provided informed consent. All US examinations were completed using a Logiq E9 scanner equipped with a C1-6-D transducer (GE Healthcare, Wauwatosa, WI). Subjects received a bolus injection of 0.2 to 0.3 ml of a MB contrast agent (Definity, Lantheus Medical Imaging, N Billerica, MA) followed by a 10 ml saline flush. CEUS imaging was performed using a dual imaging mode, enabling side-by-side visualization of the grayscale B-mode US and CEUS images at a rate of 8 to 9 frames per second. A low mechanical index (< 0.1) was used to avoid MB destruction during the US imaging sessions. A nonlinear harmonic imaging mode was used for improved MB visualization (transmit at 2 MHz, receive at 4 MHz) and gain settings were adjusted to minimize nonlinear signals prior to contrast injection. The focal zone was placed just below the approximate depth of the lesion to maximize the generation of nonlinear signals during CEUS imaging. The approximate tumor mid-line was imaged until homogenous liver enhancement was achieved (approximately 40 to 45 seconds post-injection), followed by imaging sweeps through the tumor. Patients underwent a total of three separate CEUS exams. In this study, we acquired only the pre-therapeutic baseline measurements from each subject. As a reference standard, treatment response was defined as incomplete (i.e., requiring retreatment) based on (in order of preference when available) (a) pathological examination of explanted livers demonstrating live tumor; (b) tumor enhancement seen with CT or MR and confirmed via angiography during retreatment; (c) interval tumor growth on 6 month follow-up CE-CT/MRI; or (d) asymmetrical or

nodular tumor enhancement on CE-MRI/CT on 6 month follow-up. Complete treatment response was determined using pathological examination of explanted livers when available, and a complete lack of enhancement and tumor size reduction on CE-MRI/CT at 6 months in patients who did not undergo transplant. Table 3.1 shows the patient's demographics including the tumor size and location in addition to TACE treatment information. All patients were treated with a single session with CEUS data collected before retreatment was initiated.

### 3.2.2 Image Processing

A custom MATLAB (MathWorks, Inc., Natick, MA) software was developed to pre-process the images and to extract the vascular morphology features. Figure 3.1 illustrates the proposed image processing and analysis pipeline. First, we applied a two-stage motion correction method to align the frames from the dynamic CEUS sequence. Following that, a singular value filter (SVF) was applied to remove the tissue signal, and a multiscale vessel enhancement filter was used as a pre-processing step before segmentation. After centerline detection, relevant morphological features were extracted. Finally, a distance weighted discrimination method was used to train and evaluate the vascular morphological features as TACE therapy response predictors in patients with HCC.

To delineate the tumor area, a region-of-interest (ROI) was drawn manually by a trained sonographer with over five years' experience in CEUS and who also conducted the US examinations. The quality of co-registered B-mode US and CEUS sequences was degraded due to patient's normal respiratory, cardiac physiology, and US transducer movement [21], [22]. According to the image acquisition protocol, any motion after about 40 seconds (the first 355 frames) were eliminated as the probe was rotated and resulted in out-of-plane motions.

Table 3.1. Patient Information: Sex, BMI, age, tumor dimensions, tumor location (segment), treatment received, TACE results (lipiodol TACE vs. DEB-TACE) and TACE response.

| Subject No. | Sex | BMI ($kg/m^2$) | Age | Largest tumor dimension(cm) | Tumor (segment) | Treatment received | TACE response |
|---|---|---|---|---|---|---|---|
| 1 | M | 35.3 | 63 | 2.0 | 6 | c-TACE | Complete |
| 2 | M | 22.1 | 71 | 7.1 | 7 | c-TACE | Incomplete |
| 3 | M | 21.0 | 52 | 4.2 | 8 | DEB-TACE | Complete |
| 4 | M | 39.2 | 44 | 2.4 | 8 | c-TACE | Complete |
| 5 | M | 31.9 | 68 | 2.3 | 7 | DEB-TACE | Complete |
| 6 | M | 28.1 | 62 | 2.0 | 2 | c-TACE | Complete |
| 7 | M | 41.8 | 42 | 5.5 | 4 | DEB-TACE | Incomplete |
| 8 | M | 24.0 | 48 | 4.0 | 3 | DEB-TACE | Incomplete |
| 9 | M | 30.0 | 69 | 4.1 | 2 | DEB-TACE | Incomplete |
| 10 | F | 27.3 | 47 | 2.5 | 5 | DEB-TACE | Incomplete |
| 11 | M | 26.5 | 70 | 1.8 | 7 | DEB-TACE | Incomplete |
| 12 | M | 33.2 | 60 | 2.4 | 8 | DEB-TACE | Complete |
| 13 | M | 23.7 | 67 | 2.8 | 6 | DEB-TACE | Incomplete |
| 14 | M | 27.3 | 78 | 2.4 | 8 | DEB-TACE | Complete |
| 15 | M | 27.5 | 62 | 2.1 | 2 / 3 | DEB-TACE | Complete |
| 16 | F | 37.7 | 44 | 2.5 | 7 | DEB-TACE | Complete |
| 17 | M | 29.0 | 56 | 2.6 | 2 | DEB-TACE | Complete |
| 18 | M | 24.0 | 56 | 1.8 | 3 | DEB-TACE + c-TACE | Complete |
| 19 | M | 23.9 | 54 | 3.0 | 8 | DEB-TACE + c-TACE | Incomplete |
| 20 | M | 28.7 | 67 | 2.6 | 4A | c-TACE | Incomplete |
| 21 | M | 26.2 | 69 | 6.3 | 8 | DEB-TACE + c-TACE | Incomplete |
| 22 | M | 29.5 | 65 | 1.5 | 6 | DEB-TACE + c-TACE | Complete |
| 23 | M | NA | 62 | 3.5 | 6 | DEB-TACE | Complete |
| 24 | M | 19.7 | 56 | NA | 2 | DEB-TACE + c-TACE | Complete |
| 25 | M | 25.9 | 66 | 3.8 | 5 | DEB-TACE | Incomplete |
| 26 | F | 22.4 | 72 | 5.9 | 7 | DEB-TACE + c-TACE | Incomplete |
| 27 | M | 31.4 | 60 | 8.1 | 2 | DEB-TACE | Incomplete |
| 28 | F | 27.7 | 71 | 3.8 | 4 | DEB-TACE | Incomplete |
| 29 | M | 31.9 | 74 | 2.4 | 8 | DEB-TACE + c-TACE | Complete |
| 30 | M | 25.8 | 66 | 1.3 | 8 | DEB-TACE + c-TACE | Complete |
| 31 | M | 39.0 | 72 | 7.2 | 7 | DEB-TACE + c-TACE | Incomplete |
| 32 | M | 23.9 | 69 | 8.4 | 6 | DEB-TACE + c-TACE | Incomplete |
| 33 | M | 31.0 | 64 | 2.9 | 6 | DEB-TACE + c-TACE | Complete |
| 34 | F | NA | 65 | 2.8 | 4B | DEB-TACE | Complete |
| 35 | M | 25.0 | 66 | 1.7 | 8 | c-TACE | Complete |
| 36 | F | 32.0 | 62 | 3.0 | 8 | DEB-TACE | Incomplete |

BMI = body mass index; TACE = transarterial chemoembolization; c-TACE = lipiodol TACE; DEB-TACE = drug-eluting beads TACE

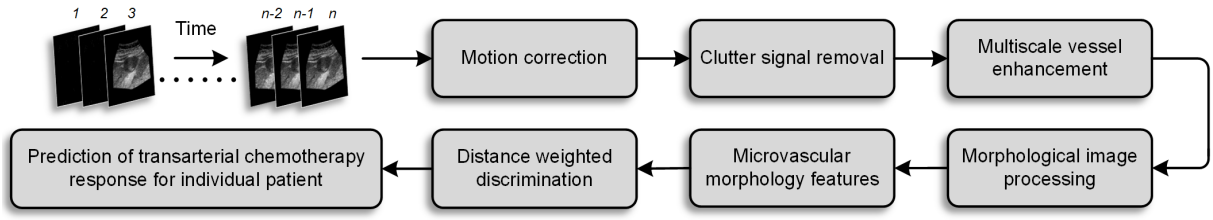


Figure 3.1. Image processing and analysis pipeline for prediction of transarterial chemotherapy (TACE) response for an individual patient with hepatocellular carcinoma (HCC). The contrast-enhanced ultrasound (CEUS) image sequence was aligned using the first frame as reference. Tissue signal was removed, and vasculature was enhanced at multiple scales before segmentation. Using morphological operations, tumor microvascular features were extracted. A distance-weighted discriminator was trained using the CEUS image-derived morphological features and leave-one-out validation.

The remaining B-mode US images were used to estimate the in-plane tissue motion. Since the co-registered CEUS images contained more visible MB motion, which was relevant for the further processing steps, the tissue motion was estimated on the B-mode US image sequence. The first frame was selected as reference frame based on the assumption that the best visualization of the tumor was collected at the beginning of the acquisition. Following that, affine and non-rigid motion estimation methods were used to compute the displacements of the B-mode US images from the reference. In brief, the affine transformations compensated the global motion, and free-form deformations adjusted the motion on local regions in CEUS images using a limited memory Broyden Fletcher Goldfarb Shanno (L-BFGS) optimizer [23], [24]. According to the combined transformations estimated from the B-mode US images:

$$T(x, y) = T_{global}(x, y) + T_{local}(x, y) \tag{3.1}$$

where $x$ and $y$ are the pixel coordinates, the corresponding CEUS images were aligned with the reference frame [21], [22].

The tissue clutter signal was removed using a SVF [25]. SVF is a principal component analysis (PCA) based filter using singular value decomposition (SVD). It forms a small windowed matrix over all the frames (a temporal kernel), which reduces the computation time and memory consumption for SVD. The temporal kernel helps to incorporate more local information by separating the three dominate US signals, namely, from the tissue, MB contrast agent, and noise [26]. Removing the tissue artifacts from the images increases the contrast-to-tissue (CNR) ratio. After SVF, all of the frames were merged using the maximum intensity projection (MIP) technique whereby the final image has the maximum intensity values throughout consecutive frames of the image sequence at each pixel location [27].

To visualize the tumor vascular network in greater detail, the tubular structures of the MIP were enhanced using a multiscale vessel enhancement filter. This method has been used in magnetic resonance and computed tomography (CT) angiography to increase the diagnostic quality [28]. It uses the second fundamental form from differential geometry, which allows approximating an image locally by its second-order Taylor expansion. The first and second-order derivatives of the image in the Taylor expansion provide a directional change in intensity values and curvature information of the image [29]. Specifically, the eigenvectors of the Hessian matrix give the amount of intensity variations. Tubular structures are detected as structures with high variations in the longitudinal direction and low variations in cross-sectional direction, i.e., the highest eigenvalues and its orthogonal counterpart at each pixel, respectively. Derivatives of the image are provided by the convolutions with the derivatives of Gaussian kernels, while multiscale enhancement is achieved by different sigma (the width of the kernel) values of these Gaussians. A

vesselness function $V_o(\gamma)$ results in higher values for tubular structures in 2D and minimizes the noise:

$$.. \quad V_o(\gamma) = \begin{cases} 0 & if\ \lambda_2 > 0 \\ exp\left(-\frac{R_{B^2}}{2\beta^2}\right)\left(1 - exp\left(-\frac{S^2}{2c^2}\right)\right) \end{cases}, \quad R_B = \frac{|\lambda_1|}{\sqrt{|\lambda_2|}}, S = \sqrt{\sum_{j=1}^{2} \lambda_j^2} \tag{3.2}$$

where $\lambda_{1,2}$ are eigenvalues from the Hessian matrix of the image, $R_B$ is for identification of blob-like or tubular patterns, $S$ is the definition of the structureness, $\gamma$ is used for the different scales of Gaussian kernels, $\beta$ and $c$ are the regularization parameters for adjusting filter sensitivity. With this, thicker vessels are detected by kernels with a large sigma, while thinner vessels are detected by kernels with a small sigma in the scale selection process.

Using the same clinical US system and settings used for patient data collection, a flow phantom of known vessel dimensions was used to calibrate the custom software for the scale range selection in a controlled environment. Although this scale selection process can be optimized for thicker vessels, finding a lower bound for the thinner vessels was only possible with the risk of including some noise or removing some desired vessel signal. Hence, this lower limit was assessed qualitatively by the amount of background suppression. After the scale selection process, a multiscale image with enhanced vascular structures was created.

### 3.2.3 Morphological Feature Extraction

To use morphological image operations, vessels from the multiscale image were segmented using an adaptive thresholding method [30]. This method first creates an integral image to compute the average value of the neighboring pixels. The binary image is created by the comparison of the current pixel value with this average. The foreground and background pixels from the binary image

were used to compute the morphological features of tumor vasculature. First, the vessel-to-tissue ratio (VR) was estimated [10].

The centerlines of the segmented vessels were extracted using a parallel thinning algorithm [31] as a simplified version of the tumor vascular network. This method keeps the same digital connectivity patterns and the topology of the vascular structures by modifying 8-connected skeletons and retaining diagonal lines as well as 2 x 2 squares [32]. As shown in Figure 3.2, the nodes and edges of the skeletonized network was considered as bifurcations (or branching points) and individual vessel segments, respectively. Accordingly, the number of bifurcations (NB) was found by counting each node of the network, and the number of vessels (NV) was the edge count of the network. As introduced in our previous work [19], the distance transform was used to estimate vessel diameters at each pixel on the centerline as the Euclidian distance between the centerline pixel and the closest edge pixel of the regarded tubular structure (vessel edge). A mean vessel diameter for the entire tumor was then computed by averaging all of the mean diameters from individual vessel segments. Similarly, the mean vessel length (VL) and vessel tortuosity (VT)

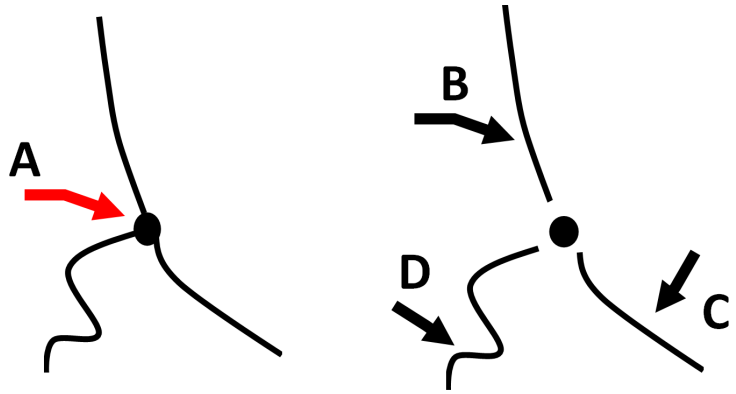


Figure 3.2. Schematic for the definition of select morphological features. The simplified tumor angiogenic network from centerlines of the tubular structures contain vessels with branching points or nodes (A). Individual vessel segments, edges are counted after the removal of the branching point. (B), (C), and (D) denote individual vessels with gradually increased tortuosity and different vessel length.

metrics were computed by averaging over all of the vessel segments [10]. Note VT as metric value is zero only for straight vessel segments

### 3.2.4 Feature Selection and Model Assessment

The predictability of HCC response to TACE treatment was evaluated using a distance weighted discrimination method (DWD) [33]. This employs an improved machine learning method for statistical analysis of high-dimension low-sample size data. Similar to support vector machines (SVM), DWD discriminates the data into two classes but different from SVM; DWD avoids data piling and increases the generalizability of the model. The small sample size of our dataset is the rationale of choosing the DWD as the classification algorithm.

All of the data points were labeled with one of the two classes, i.e., complete and incomplete response to prepare the training data [34]. The leave one out cross-validation method was used to have a reliable accuracy [35]. For this, the sample (N = 36) was divided into a construction (N = 35) and a validation (N = 1) sub-datasets for each patient data [36]. Thus, 36 different models were trained separately with 35 patient's data and validated on one exam. In the end, the average accuracy of all 36 cases was reported as the final accuracy. To investigate the contributions of the six extracted features from tumor vasculature for the prediction of the TACE response, two models were trained with a different set of features. The first model used all of the features, while the second model used only the most discriminative features, which was assessed visually by the pair plots of features, i.e., the most correlated features were excluded. Both models were tuned using a polynomial kernel with different values for the hyper-parameters and the best performing model was chosen from the largest values of accuracy and interrater reliability statistics (kappa). The data were centered and scaled in a pre-processing step before each training. All computations and data

analyses were performed using a statistical software package (R Foundation for Statistical Computing, Vienna, Austria) [37], [38].

### 3.3 Results

CEUS image-derived vascular morphological features were used to evaluate HCC response to TACE treatment in 36 patients. According to the CT, MRI, and pathology outcomes, 19 patients had a complete response, and the other 17 had an incomplete response. Figure 3.3 shows the two-step motion correction results using two representative patients' data with complete and incomplete response, respectively. Starting from a single B-mode US image showing the anatomical structures, two MIPs of the initial dynamic B-mode US and CEUS image sequence have a challenging view of the tumor. MIPs are created using the maximum intensity value of each frame for each pixel location. Given use of the same dynamic range as the original CEUS images, MIPs can have intensity saturations, e.g., bright pixels. Here, the raw results after MIP processing were presented directly without any gain compensation for comparison with the results after the motion correction process. After the correction of the in-plane motion, the abdominal structures and the tumor vasculature are more visible in the MIP. These representative US images demonstrate the need for motion correction in the image processing pipeline to improve tumor visibility before starting with the feature extraction.

The effect of clutter signal removal is illustrated in Figure 3.4. The presence of the tissue signal can complicate vessel detection. Removing the tissue signal increased the CNR as depicted in the

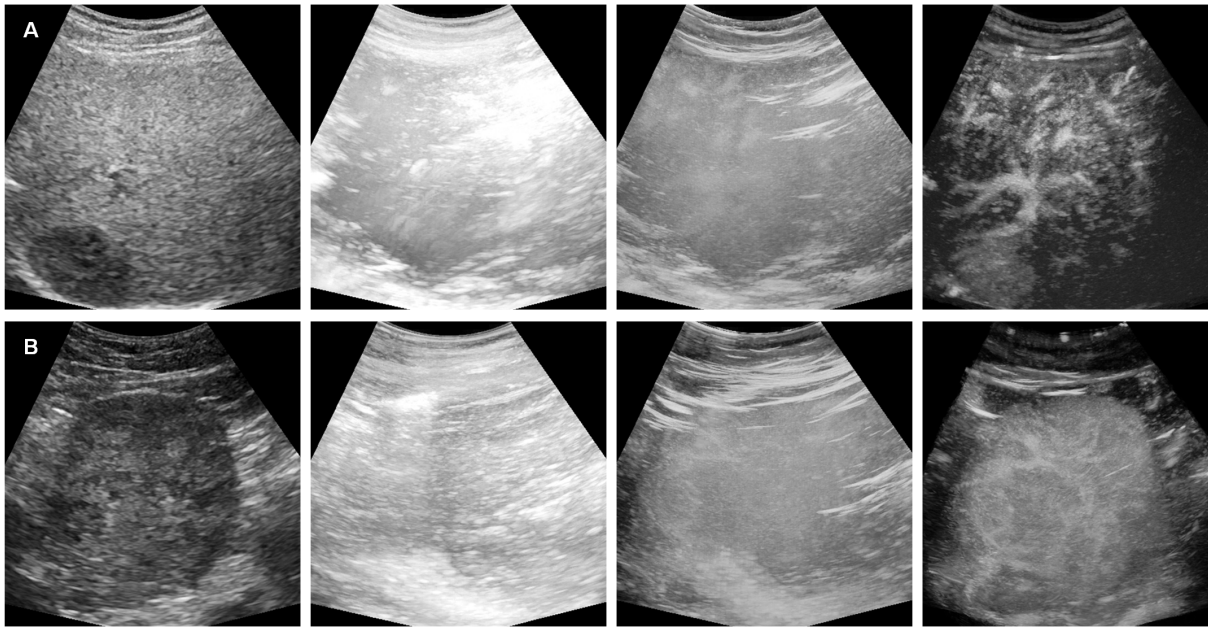


Figure 3.3. Representative ultrasound (US) results from patients with HCC determined to have either a complete (top) or incomplete (bottom) response to TACE treatment. As shown from left to right are the B-mode US image, maximum intensity projection (MIP) of the original B-mode US, CEUS image, and MIP of the motion corrected CEUS image sequence.

paired images. These SVF outputs improve the results of the multiscale vessel enhancement filter in the next step. The morphological image processing results summarized in three steps for each of the representative cases, is depicted in Figure 3.5. First, the results from the multiscale vessel enhancement filter is overlaid on the SVF results. The enlarged ROIs depict the binary image before spatial morphological filters like opening and closing. The enlarged ROIs also represent the centerlines detected from the binary vasculature. The simplified tumor network topology (centerlines) indicates the vascular routes for effective drug delivery, which is crucial for effective embolization. Figure 3.6 and Figure 3.7 present cases of HCC from individual patients for complete responders and incomplete responders, respectively. The colors indicate the vessel diameters. Here, the difference in tumor vascular complexity for the complete and incomplete

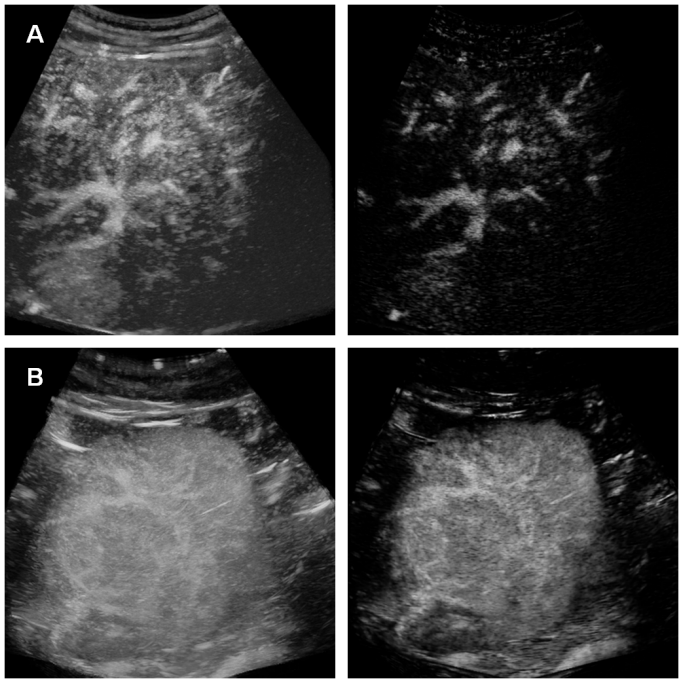


Figure 3.4. Representative results after spatiotemporal filtering of the CEUS images from patients with HCC determined to have either a complete (top) or incomplete (bottom) response to TACE treatment.

response groups can be assessed qualitatively. A larger number of vessels and bifurcations contribute more to the chaotic visualizations of the tumor vascular networks which was observed more in incomplete responders group.

CEUS derived morphological features were used to assess the correlated and discriminative features qualitatively for complete and incomplete response patients. As highlighted in Figure 3.8, the weakest feature was the VD parameter compared to all other features. Training with all of the features achieved only a 52% accuracy while training with the feature set where VD was excluded achieved an accuracy of 72% and training with the dominant features (NV, NB, and VR) achieved the best overall accuracy of 86%. As informed by the pair plot and confirmed by the accuracy, the dominant features, namely, NV, NB, and VR, were selected to train and tune the final machine

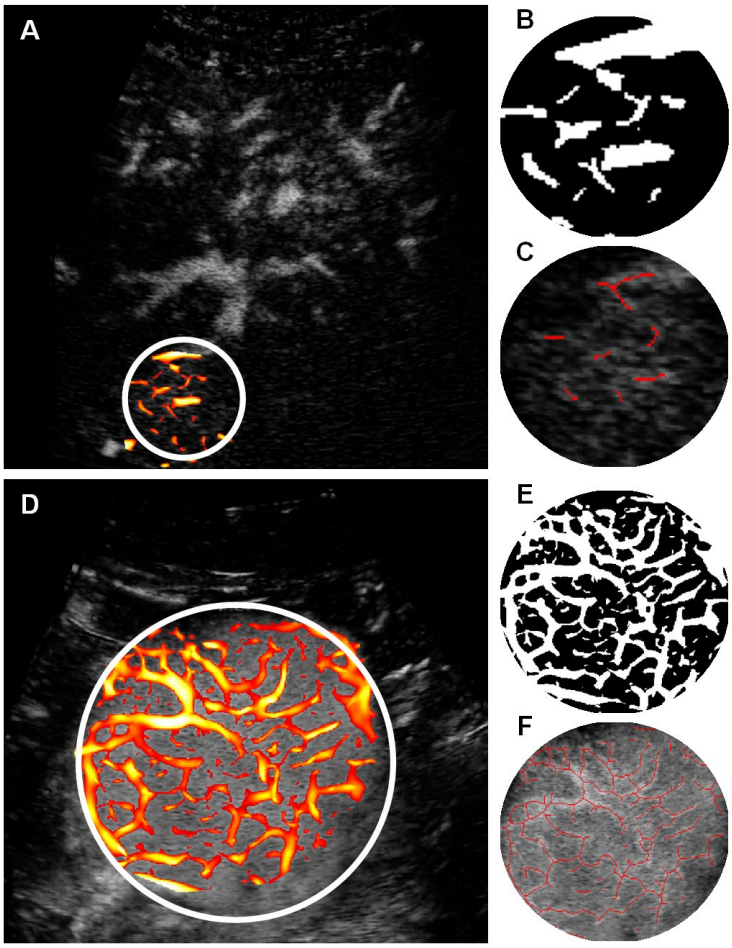


Figure 3.5. Morphological operations after application of multiscale vessel enhancement in (A) and (D), the result of spatial filtering and binarization in (B) and (E) , and the centerline detection in (C) and (F) for the representative complete and incomplete response patients, respectively.

learning model. As listed in Table 3.2, this final model achieved a validation accuracy of 86% (95% CI [0.70, 0.95]) and a kappa statistic of 72%. A sensitivity and specificity of 89% and 82%, respectively, were obtained. Table 3.3 details the confusion matrix for the model performance in terms of individual predictions. Overall, these performance metrics showed that our model was able to make reliable pre-therapeutic HCC response to TACE predictions.

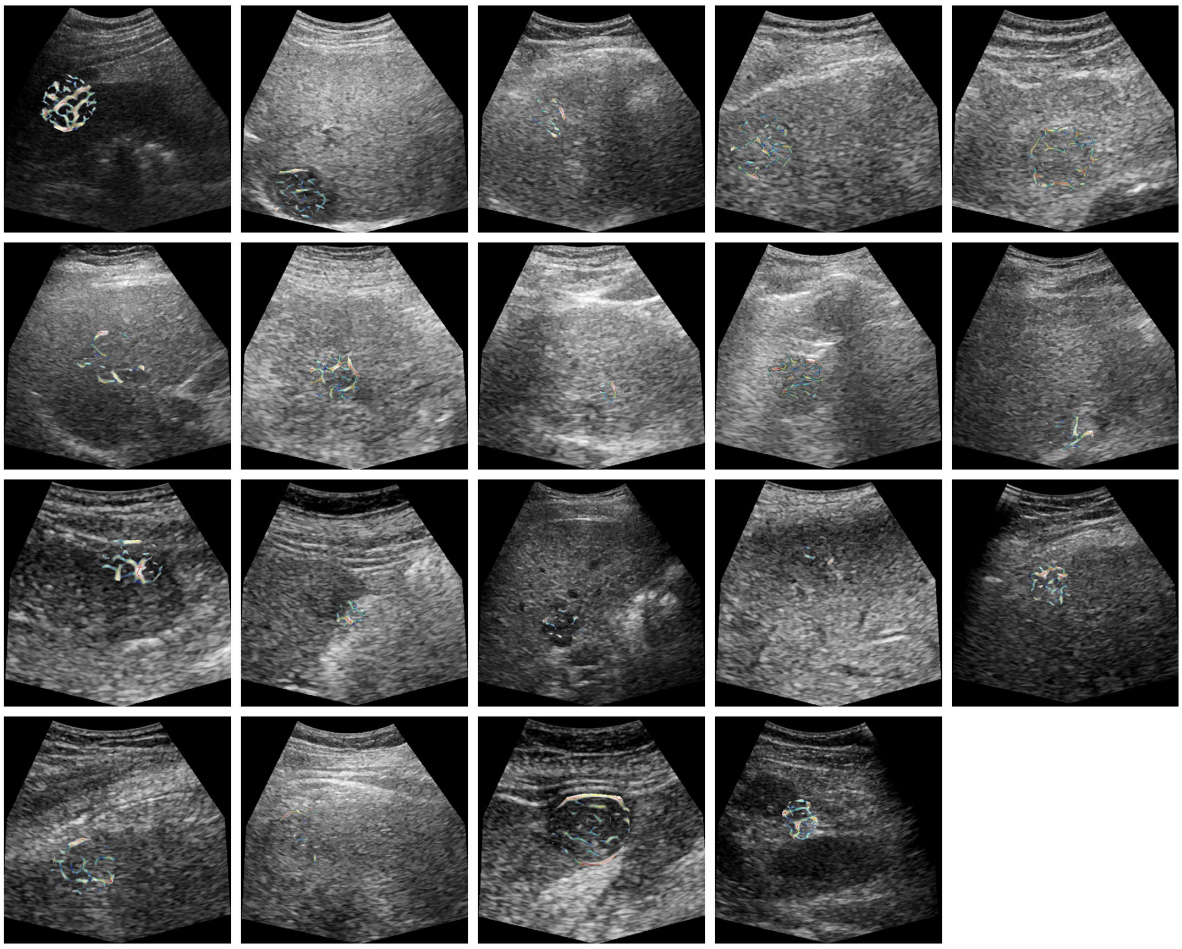

Figure 3.6. US images from patients with HCC that exhibited a complete response to TACE treatment. Microvascular morphological structures are overlaid on a single B-mode US image (reference frame). Color indicates the vessel diameter measurements from red (high) to blue (low).

### 3.4 Discussion

The strength of the proposed image processing and analysis method is that it is based on the patient specific geometry of their tumor vascular network while addressing the image processing

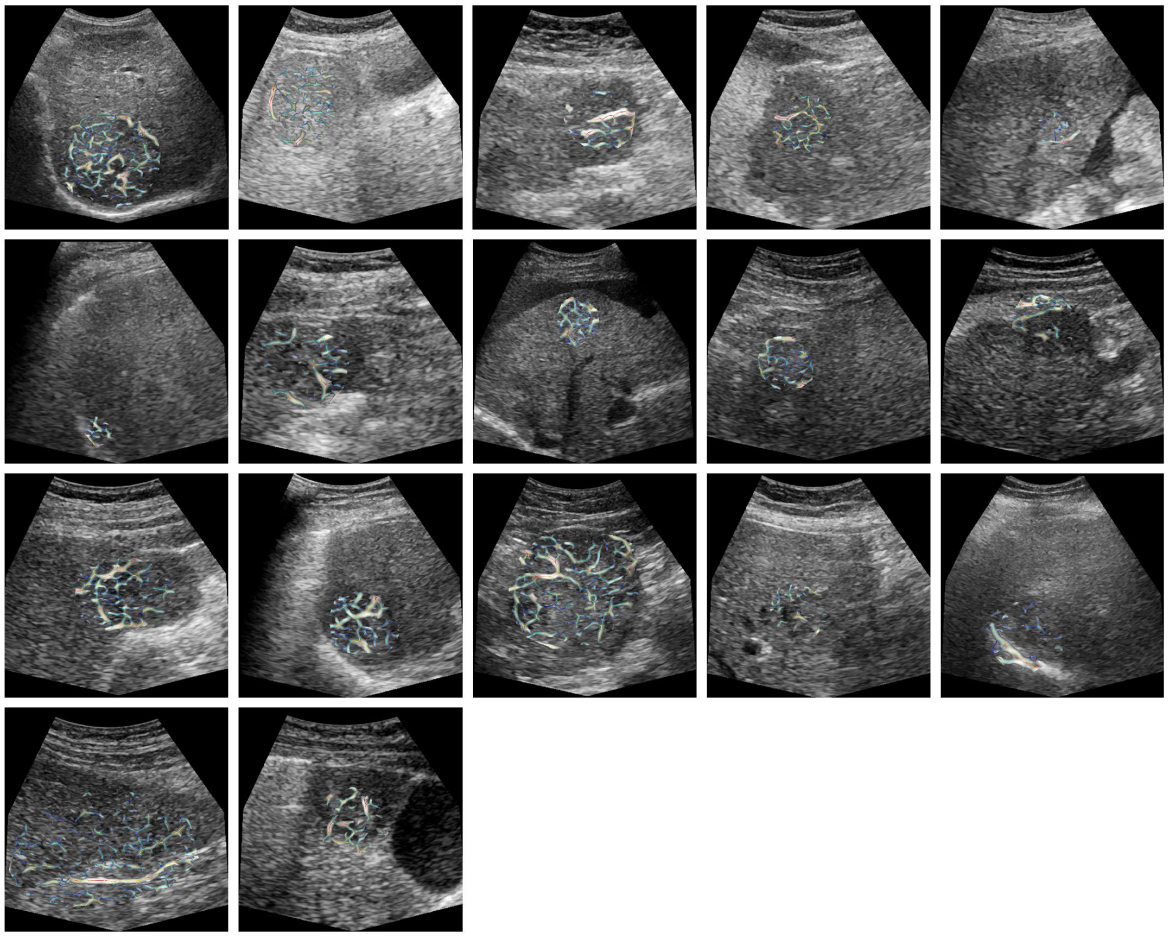

Figure 3.7. US images from patients with HCC that exhibited an incomplete response to TACE treatment. Microvascular morphological structures are overlaid on a single B-mode US image. Color indicates the vessel diameter measurements from red (high) to blue (low). Note that tumors are relatively large and have a more chaotic microvascular structure compared to patient tumors that exhibit a complete response to TACE.

challenges, such as motion artifacts, tissue signal, and multi-scale segmentation in abdominal CEUS imaging before parameterization. This enables automated pre-processing for each patient and a reliable prediction of the TACE therapy response. Reproducible quantifications of HCC vascular networks depicted in CEUS images and the prediction of pre-therapeutic TACE response, can improve customized treatment strategies in personalized medicine.

Table 3.2. Model Performance Parameters

| Model Trained with Features | NV, NB, and VR |
|---|---|
| **Accuracy** | 86 % |
| **Kappa** | 72 % |
| **Sensitivity** | 89 % |
| **Specifity** | 82 % |
| **%95 CI*** | 0.705 – 0.953 |

*CI = Confidence Interval
NV = Number of vessels, NB = Number of bifurcations,
VR = Vessel-to-tissue ratio

Aggressive tumors are known to have chaotic angiogenic networks [39] with more tortuous [13]–[15] and dense vasculature [10]. The complexity of the tumor vascular network may affect the arterial delivery of the drug-eluting beads during TACE treatment. Thus, quantification of the tumor angiogenic network may provide crucial information for physicians during treatment planning. The NV, NB and VR parameters were shown to be the most effective features for predicting HCC response to TACE. The more bifurcations in the angiogenic network may result in more embolization targets.

Table 3.3. Leave-one-out cross-validation results

| Predictions/True Response | Incomplete | Complete |
|---|---|---|
| **Incomplete** | 14 | 2 |
| **Complete** | 3 | 17 |

If it is believed that the intra-arterial therapies will not provide adequate treatment response, alternative locoregional therapies such as ablation or radiation may be employed. In this study, CEUS image-derived morphological features of the HCC vascular network were able to predict

the eventual TACE response. The preliminary results indicate that liver tumors with less complex vascular networks have a higher potential for a complete response to TACE therapy. This may be partially attributed to the fact that tumors with more developed vascular patterns may have multiple feeding sources, requiring multiple TACE treatments for complete embolization. These tumors may be more amenable to TARE, which requires localized deposit of radiation containing beads but not complete embolization of the tumor vasculature.

Using MRI as a preoperative conventional, image features and texture analysis have been shown to predict tumor response to TACE treatment [40]. Texture features from CT images have also been shown to be potential predictors for identifying patients who are not suitable for TACE

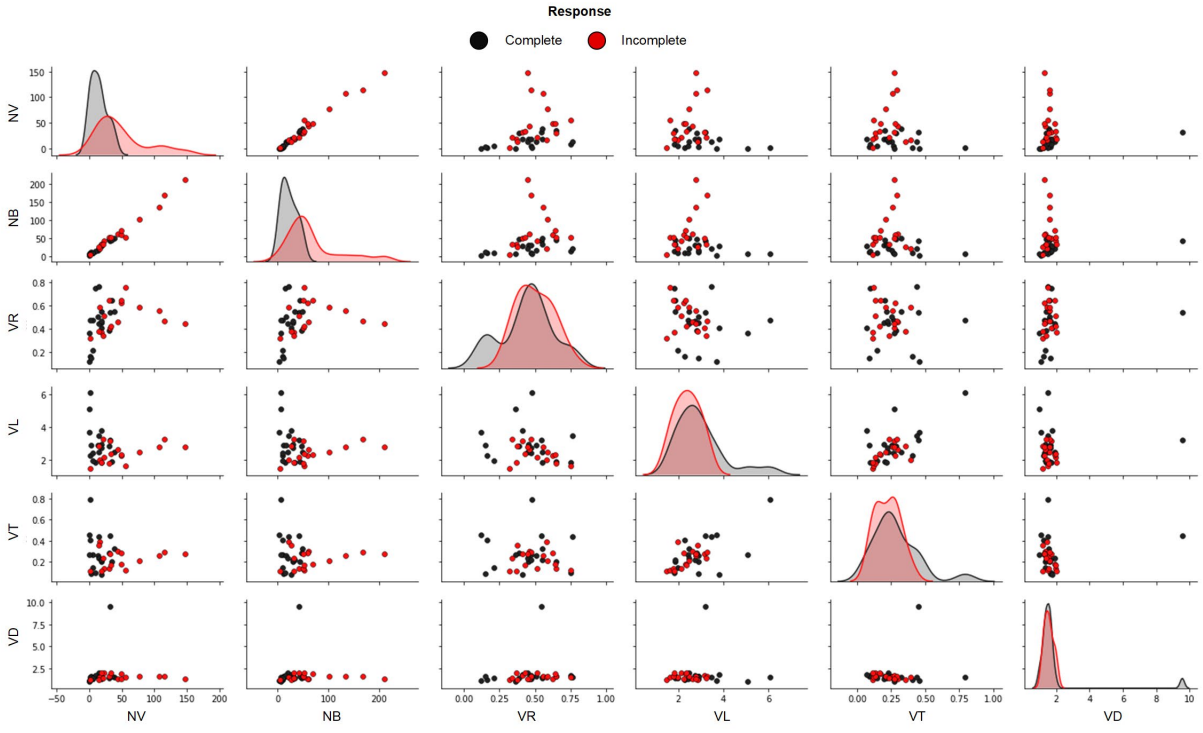


Figure 3.8. Visual assessment of morphological features from patients that were determined to have undergone either a complete or incomplete response TACE. Number of vessels (NV), number of branching points (NB), vessel-to-tissue ratio (VR), mean vessel length (VL), mean vessel tortuosity (VT), and mean vessel diameter (VD).

treatment [41]–[43]. In a more recent study, it was shown that CT-derived image features can predict the response of TACE using a residual convolutional neural network with up to 85% accuracy [44]. Another recent study aimed to establish the feasibility of an artificial intelligence–based radiomics strategy for predicting TACE response [45]. To date none of these approaches have resulted in clinical adoption.

CEUS imaging can be used to help monitor tumor response to systemic drug treatment [8], [10]. Advanced image analysis of breast tumor vascular networks depicted in clinical CEUS images showed both a strong correlation between functional and structural tumor parameters as well as to the post-therapeutic monitoring capabilities of CEUS image-derived morphological features [10]. This study introduced a method for quantification of unique vascular morphological features while the motion artifacts caused by patient, organ, or transducer motion were neglected during the image processing. Motion artifacts can negatively impact the accuracy during quantification of vascular morphological features. In a recent preclinical study, a simpler morphological feature called the vascular network length was used [46]. This parameter was shown to be a feasible metric for describing tumor vascular morphology from CEUS images with the support of the other features, such as first- order statistics, functional, textural, and wavelet-based features. This study segmented the tumor vasculature by intensity thresholding without addressing the potential lost visualization of the smaller vessels when focused on larger vessels only. Segmentation at only one scale can also affect the quantification of vascular morphology. Our method addressed both of these challenges and helped improve the overall CEUS image quantification process.

Showing the feasibility of morphological feature extraction from HCC tumor vasculature and the ability of assessing the future TACE response, this study is limited by its small sample size. Before introducing to clinical practice, the approach presented in this paper needs to be extensively validated using a large sample size and data from different sites.

### 3.5 Conclusion

A novel CEUS image processing and analysis method was developed that both extracts the morphological features from the tumor vascular network and predicts HCC response to TACE treatment. Introduction of a reliable method for predicting a TACE response may help provide more effective therapeutic planning and more personalized patient strategies.

### 3.6 References


[1] S. F. Altekruse, K. A. McGlynn, and M. E. Reichman, "Hepatocellular carcinoma incidence, mortality, and survival trends in the United States from 1975 to 2005," *Journal of Clinical Oncology: Official Journal of the American Society of Clinical Oncology*, vol. 27, no. 9, pp. 1485–1491, 2009.

[2] H. Kim and H. B. El-Serag, "The epidemiology of hepatocellular carcinoma in the usa," *Curr Gastroenterol Rep*, vol. 21, no. 4, p. 17, 2019.

[3] D. B. Brown *et al.*, "Quality improvement guidelines for transhepatic arterial chemoembolization, embolization, and chemotherapeutic infusion for hepatic malignancy," *Journal of Vascular and Interventional Radiology*, vol. 23, no. 3, pp. 287–294, 2012.

[4] R. Yamada *et al.*, "Transcatheter arterial chemoembolization (tace) in the treatment of unresectable liver cancer," *World J. Surg.*, vol. 19, no. 6, pp. 795–800, 1995.

[5] R. Kloeckner, G. Otto, S. Biesterfeld, K. Oberholzer, C. Dueber, and M. B. Pitton, "Mdct versus mri assessment of tumor response after transarterial chemoembolization for the treatment of hepatocellular carcinoma," *Cardiovasc Intervent Radiol*, vol. 33, no. 3, pp. 532–540, 2010.

[6] C. M. Shaw *et al.*, "Contrast-enhanced ultrasound evaluation of residual blood flow to hepatocellular carcinoma after treatment with transarterial chemoembolization using drug-eluting beads," *Journal of Ultrasound in Medicine*, vol. 34, no. 5, pp. 859–867, 2015.

[7] F.-H. Yan *et al.*, "Role and limitation of fmpspgr dynamic contrast scanning in the follow-up of patients with hepatocellular carcinoma treated by tace," *World J Gastroenterol*, vol. 8, no. 4, pp. 658–662, 2002.

[8] K. Nam *et al.*, "Evaluation of hepatocellular carcinoma transarterial chemoembolization using quantitative analysis of 2d and 3d real-time contrast enhanced ultrasound," *Biomedical Physics & Engineering Express*, vol. 4, no. 3, p. 035039, 2018.

[9] M. A. Averkiou, M. F. Bruce, J. E. Powers, P. S. Sheeran, and P. N. Burns, "Imaging methods for ultrasound contrast agents," *Ultrasound in Medicine & Biology*, vol. 46, no. 3, pp. 498–517, 2020.

[10] K. Hoyt, H. Umphrey, M. Lockhart, M. Robbin, and A. Forero-Torres, "Ultrasound imaging of breast tumor perfusion and neovascular morphology," *Ultrasound in Medicine & Biology*, vol. 41, no. 9, pp. 2292–2302, 2015.

[11] D. Ghosh *et al.*, "Super-resolution ultrasound imaging of skeletal muscle microvascular dysfunction in an animal model of type 2 diabetes," *Journal of Ultrasound in Medicine*, vol. 38, no. 10, pp. 2589–2599, 2019.

[12] K. Hoyt, A. Sorace, and R. Saini, "Quantitative mapping of tumor vascularity using volumetric contrast enhanced ultrasound," *Investigative Radiology*, vol. 47, no. 3, pp. 167–174, 2012.

[13] R. C. Gessner, S. R. Aylward, and P. A. Dayton, "Mapping microvasculature with acoustic angiography yields quantifiable differences between healthy and tumor-bearing tissue volumes in a rodent model," *Radiology*, vol. 264, no. 3, pp. 733–740, 2012.

[14] F. Lin, S. E. Shelton, D. Espíndola, J. D. Rojas, G. Pinton, and P. A. Dayton, "3-D Ultrasound localization microscopy for identifying microvascular morphology features of tumor angiogenesis at a resolution beyond," *Theranostics*, vol. 7, no. 1, pp. 196–204, 2017.

[15] S. R. Rao, S. E. Shelton, and P. A. Dayton, "The 'fingerprint' of cancer extends beyond solid tumor boundaries: assessment with a novel ultrasound imaging approach," *IEEE Transactions on Biomedical Engineering*, vol. 63, no. 5, pp. 1082–1086, 2016.

[16] S. E. Shelton *et al.*, "Quantification of microvascular tortuosity during tumor evolution using acoustic angiography," *Ultrasound in Medicine & Biology*, vol. 41, no. 7, pp. 1896–1904, 2015.

[17] J. R. Eisenbrey, N. Joshi, J. K. Dave, and F. Forsberg, "Assessing algorithms for defining vascular architecture in subharmonic images of breast lesions," *Physics in Medicine and Biology*, vol. 56, no. 4, pp. 919–930, 2011.

[18] R. Saini and K. Hoyt, "Recent developments in dynamic contrast-enhanced ultrasound imaging of tumor angiogenesis," *Imaging in medicine*, vol. 6, no. 1, pp. 41–52, 2014.

[19] I. Özdemir and K. Hoyt, "Morphological image processing for multiscale analysis of super-resolution ultrasound images of tissue microvascular networks," *Proc. SPIE Medical Imaging*, vol. 10955, p. 1095505, 2019.

[20] I. Oezdemir, C. E. Wessner, C. Shaw, J. R. Eisenbrey, and K. Hoyt, "Multiscale quantification of tumor microarchitecture for predicting therapy response using dynamic contrast-enhanced ultrasound imaging," *Proc IEEE Ultrason Symp*, pp. 1173–1176, 2019.

[21] S. Harput *et al.*, "Two stage sub-wavelength motion correction in human microvasculature for CEUS imaging," *Proc IEEE Ultrason Symp*, pp. 1–4, 2017.

[22] I. Oezdemir, C. Shaw, J. R. Eisenbrey, and K. Hoyt, "Improved quantitative contrast-enhanced ultrasound imaging of hepatocellular carcinoma response to transarterial chemoembolization," *Proc IEEE Int Symp Biomedical Imaging*, pp. 1737–1740, 2019.

[23] D. Rueckert, L. I. Sonoda, C. Hayes, D. L. G. Hill, M. O. Leach, and D. J. Hawkes, "Nonrigid registration using free-form deformations: application to breast MR images," *IEEE Transactions on Medical Imaging*, vol. 18, no. 8, pp. 712–721, 1999.

[24] D. J. Kroon, "B-spline Grid, Image and Point based Registration," *Mathworks*, 2011.

[25] F. W. Mauldin, D. Lin, and J. A. Hossack, "The singular value filter: a general filter design strategy for pca-based signal separation in medical ultrasound imaging," *IEEE Transactions on Medical Imaging*, vol. 30, no. 11, pp. 1951–1964, 2011.

[26] C. Demené *et al.*, "Spatiotemporal clutter filtering of ultrafast ultrasound data highly increases doppler and fultrasound sensitivity," *IEEE Transactions on Medical Imaging*, vol. 34, no. 11, pp. 2271–2285, 2015.

[27] F. Forsberg *et al.*, "Contrast enhanced maximum intensity projection ultrasound imaging for assessing angiogenesis in murine glioma and breast tumor models: A comparative study," *Ultrasonics*, vol. 51, no. 3, pp. 382–389, 2011.

[28] A. F. Frangi, W. J. Niessen, K. L. Vincken, and M. A. Viergever, "Multiscale vessel enhancement filtering," *SpringerLink*, pp. 130–137, 1998.

[29] R. C. Gonzalez and R. E. Woods, *Digital Image Processing*, 4th ed. New York, NY, USA: Pearson, 2018.

[30] D. Bradley and G. Roth, "Adaptive thresholding using the integral image," *ACM J. Graph. Tools*, pp. 13–21, 2007.

[31] T. Y. Zhang and C. Y. Suen, "A fast parallel algorithm for image processing and computer vision," *Communications of the ACM*, vol. 27, no. 3, p. 4, 1984.

[32] L. Lam, S.-W. Lee, and C. Y. Suen, "Thinning methodologies-a comprehensive survey," *IEEE Transactions on Pattern Analysis and Machine Intelligence*, vol. 14, no. 9, pp. 869–885, 1992.

[33] J. S. Marron, M. J. Todd, and J. Ahn, "Distance-weighted discrimination," *Journal of the American Statistical Association*, vol. 102, no. 480, pp. 1267–1271, 2007.

[34] G. James, D. Witten, T. Hastie, and R. Tibshirani, *An introduction to statistical learning*, 1st ed. New York, NY, USA: Springer-Verlag, 2013.

[35] T. Hastie, R. Tibshirani, and J. Friedman, *The elements of statistical learning*, 2nd ed. New York, NY, USA: Springer-Verlag, 2009.

[36] M. Stone, "Cross-validatory choice and assessment of statistical predictions," *Journal of the Royal Statistical Society. Series B (Methodological)*, vol. 36, no. 2, pp. 111–147, 1974.

[37] M. Kuhn, "Building predictive models in r using the caret package," *Journal of Statistical Software*, vol. 28, no. 1, pp. 1–26, 2008.

[38] R core team, "R: The R project for statistical computing," 2013. .

[39] N. Weidner, J. P. Semple, W. R. Welch, and J. Folkman, "Tumor angiogenesis and metastasis — correlation in invasive breast carcinoma," *New England Journal of Medicine*, vol. 324, no. 1, pp. 1–8, 1991.

[40] H. Zhang *et al.*, "Preoperative mri features and clinical laboratory indicators for predicting the early therapeutic response of hepatocellular carcinoma to transcatheter arterial chemoembolization combined with high-intensity focused ultrasound treatment," *The British Journal of Radiology*, vol. 92, no. 1099, p. 20190073, 2019.

[41] J. Y. Yu *et al.*, "Value of texture analysis based on enhanced mri for predicting an early therapeutic response to transcatheter arterial chemoembolisation combined with high-intensity focused ultrasound treatment in hepatocellular carcinoma," *Clinical Radiology*, vol. 73, no. 8, p. 758.e9-758.e18, 2018.

[42] Q. Cai, Y. Mao, Q. Yang, H. Wen, S. Li, and R. Zhang, "Texture analysis of computed tomography images for predicting the efficacy of transcatheter arterial chemoembolization in hepatocellular carcinoma patients," *SSRN*, 2019.

[43] H. J. Park *et al.*, "Prediction of therapeutic response of hepatocellular carcinoma to transcatheter arterial chemoembolization based on pretherapeutic dynamic ct and textural findings," *American Journal of Roentgenology*, vol. 209, no. 4, pp. W211–W220, 2017.

[44] J. Peng *et al.*, "Residual convolutional neural network for predicting response of transarterial chemoembolization in hepatocellular carcinoma from CT imaging," *European Radiology*, vol. 30, no. 1, pp. 413–424, 2020.

[45] D. Liu *et al.*, "Accurate prediction of responses to transarterial chemoembolization for patients with hepatocellular carcinoma by using artificial intelligence in contrast-enhanced ultrasound," *European Radiology*, 2020.

[46] B. Theek, T. Opacic, Z. Magnuska, T. Lammers, and F. Kiessling, "Radiomic analysis of contrast-enhanced ultrasound data," *Scientific Reports*, vol. 8, 2018.

# CHAPTER 4

# FASTER MOTION CORRECTION OF CLINICAL CONTRAST-ENHANCED ULTRASOUND IMAGING USING DEEP LEARNING

Authors – Ipek Oezdemir[1], Corrine E. Wessner[2], Colette Shaw[2], John R. Eisenbrey[2], Kenneth Hoyt[1,3]

[1]The Department of Bioengineering, BSB 11
The University of Texas at Dallas
800 West Campbell Road
Richardson, TX 75080-3021

[2]The Department of Radiology, East Falls
Thomas Jefferson University
4201 Henry Ave
Philadelphia, PA 19144

[3]The Department of Radiology
The University of Texas Southwestern Medical Center
1801 Inwood Rd
Dallas, TX 75390

Author contribution: Ipek Ozdemir (myself) was responsible for the experimental design, the data analysis, and the manuscript preparation presented here.

In this study, we present a faster motion correction strategy for clinical contrast-enhanced ultrasound imaging using deep learning methods. Motion artifacts affect the quantification accuracy of the tumor angiogenic network measurements from clinical contrast-enhanced ultrasound (CEUS) images. Reliable motion correction methods can improve image alignments but suffer from long computation times and large memory demands. This research project aims to reduce the time and memory needed for motion correction of clinical images from patients diagnosed with hepatocellular carcinoma (HCC). First, B-mode ultrasound (US) images were acquired using a clinical scanner from 36 patients and processed using a conventional two-stage motion correction strategy. Two channel input data consisting of static and moving B-mode US images were prepared as the training data ($N$ = 200 for each patient). Transformation functions derived from the conventional method for affine and non-rigid motion corrections were used as labels to train a deep learning model (encoder-decoder network). After model training, the performance was evaluated using a normalized correlation coefficient (CC) between the reference and moving images. Finally, the time needed for applying motion correction using the traditional method was compared to the prediction time from the deep learning model. On average the CC results were increased by 20% when compared to the data contaminated with motion. Importantly, the time needed to predict a single patch was $0.20 \pm 0.004$ sec instead of the $3.65 \pm 0.25$ sec, which was needed to perform motion correction in CEUS images using a more conventional method ($p$ = 0.001).

## 4.1 Introduction

As a noninvasive and nonionizing imaging modality, contrast-enhanced ultrasound (CEUS) is an ideal method for quantification of tissue microvascular networks [1]–[7]. Characterization of microvascular structures from CEUS images of tumor angiogenesis has been shown to be a useful strategy for prediction of anticancer treatment response [8]–[14]. Free hand ultrasound (US) image acquisition is not possible without any motion artifacts related to probe motion, respiratory motion, and organ motion. The accuracy of follow-up quantifications using motion contaminated data is highly dependent on a reliable motion correction method in the data processing pipeline.

Conventional motion correction methods for US images are mostly based on discarding frames after identification of the frames with respiratory and cardiac spikes [15]. Recently, a two stage motion correction strategy adapted from magnetic resonance (MR) imaging was applied to clinical CEUS images and increased overall image alignment by 20% when assessed using a normalized cross-correlation coefficient was applied to static and images corrupted with motion [16], [17]. These methods first applied affine transformations for global motion model of the vascularity depicted in the CEUS images. Then second, free form deformations based B-splines were used to model the local motion [18]. The method can be implemented by various similarity measures, such as squared differences, mutual information, or image differences between moving and reference images. Minimizing this difference metric results in the desired image alignment. The only drawback of this method is long computation times of the optimizer and large memory requirements during optimization.

Deep learning approaches have introduced new medical imaging functionality and can help accelerate processing pipelines for various processing and computer vision tasks [19], [20]. Motion

correction techniques as multimodal or unimodal image registration problems have previously been investigated using synthetic data and supervised learning for imaging modalities such as computed tomography (CT) [21]. However, synthetic training data is not realistic enough for reliable motion estimations and the models trained with synthetic images are not translatable to clinical US images yet. Here, we introduce a deep learning model that was trained and tested using human CEUS images of HCC contaminated by real motion artifacts to achieve a faster motion correction while the image registration improvement is comparable with the traditional method.

## 4.2 Materials and Methods

### 4.2.1 Ultrasound Imaging

CEUS exams of human hepatocellular carcinoma (HCC) were used for this study (N = 6) retrospectively [22]. As part of the initial research, participants provided informed consent to participate in this multi-center IRB-approved study. Images were collected with a Logiq E9 scanner (GE Healthcare, Wauwatosa, WI) equipped with a C1-6-D transducer at a rate of 8 to 9 fps. A bolus injection of 0.2 to 0.3 ml of a microbubble (MB) contrast agent (Definity, Lantheus Medical Imaging, N Billerica, MA) followed by a 10 ml saline flush helped enhanced the liver vasculature in a dual imaging mode with side-by-side visualization of the B-mode US and CEUS images. During scanning, the transducer was rotated 90° after the peak intensity point was reached and sweep through the region to be able to see all the other areas of the tumor region. This latter part of the data is excluded from the current study because it contains mostly out-of-plane motion which is not possible to improve due to missing information.

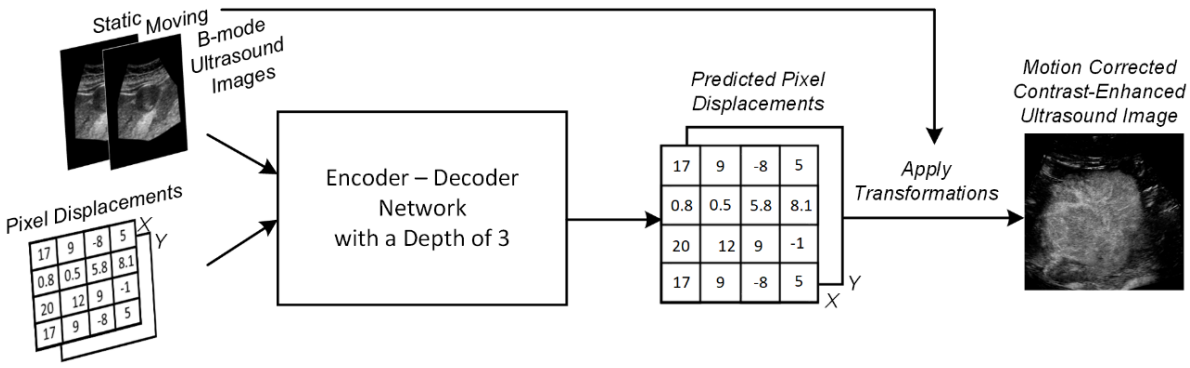


Figure 4.1. Flow chart detailing the proposed deep learning-based approach for motion correction of contrast-enhanced ultrasound (CEUS) images depicting human hepatocellular carcinoma (HCC). Image displacement measurements are obtained from moving B-mode ultrasound (US) image sequences and used to correct motion in the co-registered CEUS data.

### 4.2.2 Image Processing

Motion contaminated CEUS image sequences of HCC were cut for the first 200 frames to have only in-plane motion artifacts. Assuming that the sonographer started the cine loop with the best visualization of the tumor, the first frame of each image sequence was chosen as a reference frame and all subsequent frames were registered to that reference using the traditional motion correction method. First, affine transformations were used to compensate for global motion and then free-form deformations adjusted local motion regions in the CEUS image sequence. Limited memory Broyden-Fletcher-Goldfarb-Shanno (L-BFGS) optimization helped minimize the squared pixel distance (SD) between static and moving images. Here, instead of taking the entire frame (480 x 640), we down sampled it to 16 x 16 patches. From those we measured the optimization time to be compared with the prediction time of the proposed deep learning model. The pixel displacement matrices created by the traditional motion correction method were saved for later processing with the deep learning model.

### 4.2.3 Deep Learning Model

A fully convolutional neural network (FCN) with an encoder-decoder depth of three was developed in MATLAB (Mathworks Inc, Natick, MA). As shown in Figure 4.1, each moving image paired with its reference was used as training data. Supervision was achieved by the previously created pixel displacements. An encoder depth of 3 was chosen after having better results compared to the encoder depth of 4. All CEUS data and transformations matrices were divided in non-overlapping image tiles of 16 x 16 pixels to reduce the memory needed during training. In this study, we used 18 patches of each image and 200 frames from each subject.

For the proposed deep learning architecture to motion correction of CEUS images of HCC, we employed a standard encoder-decoder network with fully connected convolutional layers. However, we added a regression output layer after the final convolutional layer and implemented the SD metric as the loss function of the custom regression layer. The stochastic gradient descent with a momentum of 0.9 was configured as the network optimizer to have more control of oscillations on the way to the minimum value during training. A piecewise linear function (i.e., rectified linear unit, ReLU) was used for activations of each layer with an initial learning rate of 0.1. Learning rate drop factor of 0.1 and period of 10 as well as a batch size of 4 were defined empirically. The FCN was trained using CEUS images from all of the patients in an interpatient fashion. Specifically, the entire dataset was shuffled and divided into three groups, namely, training (76%), validation (8%), and testing (16%). Note that all of these three groups contained patches from all of the patients while the test data was unseen to the model during the training and validation time. The validation group was used to optimize the model training parameters for a better performance in image alignment. Once the training was completed by reaching the

maximum number of iterations for 100 epochs, the weights from the regression layer were used to create the predicted displacement fields. Once the predictions were completed, motion corrected images were generated by applying the transformations to the motion contaminated CEUS image sequences.

### 4.2.4 Evaluation Metrics

The performance of the proposed deep learning approach was evaluated in two aspects. First, the quality of the alignment in the final motion corrected image and second, the time to predict displacement fields. A normalized correlation coefficient (CC) between images with motion and the reference for the original data, for the optimizer-corrected data, and for the model-predicted data were then computed and compared. Higher CC values indicate better image registration between reference and the moving image:

$$\mathrm{CC} = \frac{\sum_m \sum_n (A_{mn} - \bar{A})(B_{mn} - \bar{B})}{\sqrt{(\sum_m \sum_n (A_{mn} - \bar{A})^2)(\sum_m \sum_n (B_{mn} - \bar{B})^2)}} \tag{4.1}$$

where $A$ and $B$ are US images, $m$ and $n$ are pixel coordinates, and $\bar{A}, \bar{B}$ are the mean image intensity of $A$ and $B$, respectively. Finally, computation times of both the conventional and deep learning-based motion correction methods were compared using a two-sample t-test.

## 4.3 Results

A deep learning approach using a fully convolutional network for motion correction of CEUS images from 36 patients with HCC is feasible in terms of efficiency and registration quality. The proposed network achieved an accuracy of 89% for any improvement with the predicted motion corrected images. Given that the traditional optimizer improved the image quality by

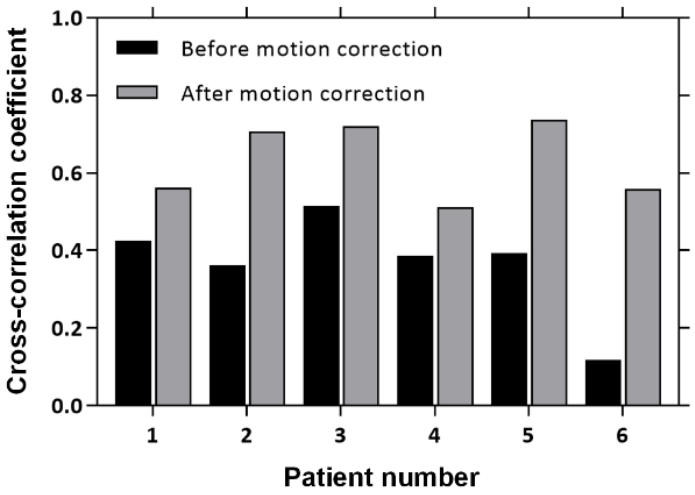


Figure 4.2. Summary of motion correction accuracy using CEUS images from six patients with HCC. Note that a higher normalized cross-correlation coefficient indicates improved image registration and elimination of motion artifacts.

approximately 0.2 in average for CC values [17], the accuracy was measured 78% for the same CC threshold (i.e., 0.2) using the proposed deep learning approach. In addition to the patch-level tests, the patient-level results presented in Figure 4.2 are promising. Increased CC values after motion correction compared to the original CC values from 6 representative patients indicate the potential of the deep learning approach to be used for motion correction of clinical CEUS images of HCC instead of the traditional optimizer.

The time needed for one frame to predict the displacement fields using the FCN was 0.20 ± 0.004 sec while the optimizer consumed 3.65 ± 0.25 sec (on average) to complete the same work. The proposed method outperformed the traditional optimizer during the prediction time, $p = 0.001$. A CEUS examination with 200 frames would require around 12 min for one patch using a more traditional motion correction method while it is completed within 38 sec using the FCN approach.

In this study, we aimed to accelerate motion correction as compared to a more traditional, but computationally exhaustive, image processing strategy. Future work for analysis of clinical CEUS images will target 3D quantifications, where a faster image processing pipeline is critically required. Although a better convergence of the deep neural network was not a priority in the work presented herein, these preliminary results are promising. The potential of the neural network encourages future experiments to increase the CC for even better alignments from the neural network than the traditional method. Here, the common consideration is the error carried from the traditional method directly to the FCN training, i.e., learning. An image similarity metric can address this concern and be optimized at multiple spatial resolutions at the same time, producing surrogate supervised information referred as a self-supervised method. This approach does not need transformation field information during training, e.g., pixel displacements.

### 4.4 Conclusion

The proposed deep learning-based motion correction approach was applied to clinical CEUS images of HCC. Motion correction was completed, and pixel-wise prediction of image displacement was 94.8% faster than results that were obtained using a more traditional CEUS image-based motion correction method. This is a considerable improvement in computational efficiency without any significant change in the registration improvement of approximately 20%.

### 4.5 References

[1] R. Saini and K. Hoyt, "Recent developments in dynamic contrast-enhanced ultrasound imaging of tumor angiogenesis," *Imaging Med*, vol. 6, no. 1, pp. 41–52, 2014.

[2] K. Hoyt, A. Sorace, and R. Saini, "Quantitative mapping of tumor vascularity using volumetric contrast-enhanced ultrasound," *Invest Radiol*, vol. 47, no. 3, pp. 167–174, 2012.

[3] I. Oezdemir *et al.*, "Multiscale and morphological analysis of microvascular patterns depicted in contrast-enhanced ultrasound images," *J Med Imaging*, vol. 7, no. 3, p. 034001, 2020.

[4] I. Özdemir and K. Hoyt, "Morphological image processing for multiscale analysis of super-resolution ultrasound images of tissue microvascular networks," *SPIE Medical Imaging*, vol. 10955, p. 1095505, 2019.

[5] D. Ghosh, F. Xiong, S. R. Sirsi, P. W. Shaul, R. F. Mattrey, and K. Hoyt, "Toward optimization of in vivo super-resolution ultrasound imaging using size-selected microbubble contrast agents," *Med Phys*, vol. 44, no. 12, pp. 6304–6313, 2017.

[6] D. Ghosh *et al.*, "Super-resolution ultrasound imaging of skeletal muscle microvascular dysfunction in an animal model of type 2 diabetes," *J Ultrasound Med*, vol. 38, no. 5, pp. 2589–2599, 2019.

[7] K. Tanigaki *et al.*, "Hyposialylated IgG activates endothelial IgG receptor FcγRIIB to promote obesity-induced insulin resistance," *J Clin Invest*, vol. 128, no. 1, pp. 309–322, 2018.

[8] K. Hoyt, H. Umphrey, M. Lockhart, M. Robbin, and A. Forero-Torres, "Ultrasound imaging of breast tumor perfusion and neovascular morphology," *Ultrasound Med Biol*, vol. 41, no. 9, pp. 2292–2302, 2015.

[9] K. Hoyt *et al.*, "Determination of breast cancer response to bevacizumab therapy using contrast-enhanced ultrasound and artificial neural networks," *J Ultrasound Med*, vol. 29, no. 4, pp. 577–585, 2010.

[10] K. Hoyt, A. Sorace, and R. Saini, "Volumetric contrast-enhanced ultrasound imaging to assess early response to apoptosis-inducing anti-death receptor 5 antibody therapy in a breast cancer animal model," *J Ultrasound Med*, vol. 31, no. 11, pp. 1759–1766, 2012.

[11] I. Oezdemir, C. E. Wessner, C. Shaw, J. R. Eisenbrey, and K. Hoyt, "Multiscale quantification of tumor microarchitecture for predicting therapy response using dynamic contrast-enhanced ultrasound imaging," *Proc IEEE Ultrason Symp*, vol. 1, pp. 1173–1176, 2019.

[12] I. Oezdemir, K. Javed, G. Rijal, and K. Hoyt, "Contrast-enhanced ultrasound imaging of acute changes in pancreatic cancer following targeted hyaluronan treatment," *Proc IEEE Ultrason Symp*, vol. 1, pp. 2303–2306, 2019.

[13] D. Ghosh *et al.*, "Monitoring early tumor response to vascular targeted therapy using super-resolution ultrasound imaging," *Proc IEEE Ultrason Symp*, pp. 1–4, 2017.

[14] I. Oezdemir, C. E. Wessner, C. Shaw, J. R. Eisenbrey, and K. Hoyt, "Tumor vascular networks depicted in contrast-enhanced ultrasound images as a predictor for transarterial

chemoembolization treatment response," *Ultrasound Med Biol*, vol. 46, no. 9, pp. 2276–2286, 2020.

[15] C. N. Ta, M. Eghtedari, R. F. Mattrey, Y. Kono, and A. C. Kummel, "2-tier in-plane motion correction and out-of-plane motion filtering for contrast-enhanced ultrasound," *Invest Radiol*, vol. 49, no. 11, pp. 707–719, 2014.

[16] S. Harput *et al.*, "Two-stage motion correction for super-resolution ultrasound imaging in human lower limb," *IEEE Trans Ultrason Ferroelectr Freq Control*, vol. 65, no. 5, pp. 803–814, 2018.

[17] I. Oezdemir, C. Shaw, J. R. Eisenbrey, and K. Hoyt, "Improved quantitative contrast-enhanced ultrasound imaging of hepatocellular carcinoma response to transarterial chemoembolization," *Proc IEEE Int Symp Biomedical Imaging*, vol. 1, pp. 1737–1740, 2019.

[18] D. Rueckert, L. I. Sonoda, C. Hayes, D. L. Hill, M. O. Leach, and D. J. Hawkes, "Nonrigid registration using free-form deformations: Application to breast MR images," *IEEE Trans Med Imaging*, vol. 18, no. 8, pp. 712–721, 1999.

[19] K. G. Brown, D. Ghosh, and K. Hoyt, "Deep learning of spatiotemporal filtering for fast super-resolution ultrasound imaging," *IEEE Trans Ultrason Ferroelectr Freq Control*, 2020.

[20] H. Tai, M. Khairalseed, and K. Hoyt, "Three-dimensional H-scan ultrasound imaging and use of a convolutional neural network for scatterer size estimation," *Ultrasound Med Biol*, 2020.

[21] K. A. J. Eppenhof and J. P. W. Pluim, "Pulmonary CT registration through supervised learning with convolutional neural networks," *IEEE Trans Med Imaging*, vol. 38, no. 5, pp. 1097–1105, 2019.

# CHAPTER 5

# MULTISCALE AND MORPHOLOGICAL ANALYSIS OF MICROVASCULAR PATTERNS DEPICTED IN CONTRAST-ENHANCED ULTRASOUND IMAGES

Authors – Ipek Oezdemir[1], Jun Peng[2], Debabrata Ghosh[1], Shashank Sirsi[1], Chieko Mineo[2], Philp W. Shaul[2], Kenneth Hoyt[1,3]

[1]The Department of Bioengineering, BSB 11
The University of Texas at Dallas
800 West Campbell Road
Richardson, TX 75080-3021

[2]The Department of Pediatrics
The University of Texas Southwestern Medical Center
5323 Harry Hines Blvd
Dallas, TX 75390

[3]The Department of Radiology
The University of Texas Southwestern Medical Center
1801 Inwood Rd
Dallas, TX 75390

*Adapted from *Journal of Medical Imaging*, **7**, Ipek Oezdemir, Jun Peng, Debabrata Ghosh, Shashank Sirsi, Chieko Mineo, Philp W. Shaul, Kenneth Hoyt, Multiscale and morphological analysis of microvascular patterns depicted in contrast-enhanced ultrasound images, 034001, SPIE, 2020.

Author contribution: Ipek Ozdemir (myself) was responsible for the experimental design, the data analysis, and the manuscript preparation presented here.

Here, an automated multiscale image processing approach was performed by defining a vessel diameter threshold for an objective and reproducible analysis at the microvascular level. A population of C57BL/6J male mice fed standard chow and studied at age 13-16 wk comprised the lean group and 24-31 wk-old mice who received a high-fat diet were designated the obese group. A clinical ultrasound (US) scanner (Acuson Sequoia 512) equipped with an 15L8-S linear array transducer was used in a nonlinear imaging mode for sensitive detection of an intravascular microbubble contrast agent. By eliminating large vessels from the CEUS images (above 300 μm in diameter), obesity-related changes in perfusion and morphology parameters were readily detected in the smaller vessels, which are known to have a greater impact on skeletal muscle glucose disposal. The results from the CEUS images including all of the vessels were compared for three different-sized vessel groups, namely, vessels smaller than 300, 200, and 150 μm in diameter. Thus, our automated image processing provides objective and reproducible results, focuses on a particular size of vessels, thereby allowing for a selective evaluation of longitudinal changes in microvascular recruitment for a specific-sized vessel group between diseased and healthy microvascular networks.

## 5.1 Introduction

Considering the high costs related to disease treatment, the impact of diabetes across the world is immense. Type 2 diabetes is suffered by 90 percent of the 400 million individuals estimated to have diabetes [1]. Alterations in microvascular function contribute to numerous aspects of type 2 diabetes pathogenesis and its complications, including the peripheral insulin resistance in skeletal muscle that drives the disorder [2], reductions in lower extremity muscle strength[3], and the associated increased risk of cardiovascular disease [4]. In type 2 diabetes, skeletal muscle microvascular recruitment is impaired, resulting in attenuated insulin delivery and compromised glucose disposal in the skeletal muscle tissue. Microvascular recruitment is defined as the dilatation of the microvasculature that delivers insulin and glucose to skeletal muscle myocytes due to an increased number of perfused capillaries. In the context of diabetes, small vessels are known to be more closely linked to disease pathogenesis and more sensitive to therapies [5], [6]. Therefore, greater knowledge of the processes that regulate muscle microvascular function at a smaller scale (e.g., vessels with diameters below 300 μm) could help increase our understanding of type 2 diabetes.

Dynamic contrast-enhanced ultrasound (CEUS) imaging has been used for the investigation of microvascular function or impairment [7]–[13]. Ultrasound (US) is widely known to be a real-time imaging mode, low-cost, and is devoid of ionizing radiation. Moreover, the spatial resolution of CEUS has been increased by 10-fold with the recently introduced technique known as super-resolution US (SR-US) [14]. This technique has enabled US imaging at the capillary level where microvascular recruitment is known to occur *in vivo*. These higher resolution CEUS images, and subsequent quantitative analysis, represent a promising new tool for assessing microvascular

recruitment in subjects suffering from type 2 diabetes [15]. However, a major challenge during CEUS image quantification is the subjectively surrounding ROI selection and placement for small vessel groups [7], [16], [17]. Reliable algorithms are critical to enable an automated and objective multiscale analysis, and to apply CEUS to both preclinical and clinical studies of type 2 diabetes risk and pathogenesis [2], [18].

The purpose of this study was to develop and evaluate a series of custom image processing algorithms for the automated multiscale analysis of CEUS images of tissue microvascularity. A second goal of this work was to investigate morphological metrics that provide structural information about the skeletal muscle microvascular network. In addition to functional perfusion parameters, CEUS-derived morphological parameters may be used to assess skeletal muscle microvascular responses to insulin challenges.

## 5.2 Materials and Methods

### 5.2.1 Image Acquisition

All animal experiments were approved by the Institutional Animal Care and Utilization Committee (IACUC) at the University of Texas Southwestern Medical Center. Studies were performed in male C57BL/6J mice (The Jackson Laboratory, Bar Harbor, ME) in two groups, namely, lean ($N$ = 14) and obese ($N$ = 9) mice. Lean mice were fed standard chow for their entire post-weaning life and were studied at 13-16 wk of age. Obese mice were placed on a high fat diet (D1233i, Research Diets Inc, New Brunswick, NJ) at weaning to promote obesity and invoke insulin resistance, and they were studied at 24 to 31 weeks of age. Mice were US imaged using a custom lipid-shelled, perfluorocarbon gas-filled, microbubble (MB) contrast agent. Following an overnight fasting

period, mice were anesthetized using isoflurane inhalation and normal body temperature (36.5 ± 0.5°C) was maintained throughout the procedure using a rectal probe and heating pad temperature monitor with homeothermic controller (Kent Scientific Corp, Torrington, CT). Animals were instrumented with a jugular venous catheter and a 4-way connector by which insulin, glucose, and the MB contrast agent could be administered as needed. The US imaging transducer was positioned and secured over the proximal hindlimb adductor muscle group (adductor magnus and semimembranosus) to capture microvascular changes along the same image plane. After a 60-min stabilization period following instrumentation, a grayscale US scan was collected before MB injection. Subsequently, baseline CEUS imaging was performed for 10 min before and following a slow bolus injection of the MB contrast agent (2.5 x $10^7$ MBs in 100 μL saline) [19]. MB concentrations were measured prior to injection using established methods (Multisizer 3 Coulter Counter, Beckman Coulter, Brea, CA). Following baseline imaging, mice underwent a 2 h hyperinsulinemic-euglycemic clamp. This procedure is the most widely used approach for the determination of insulin sensitivity, and it entails a continuous infusion of insulin (20 mU/kg/min) and a variable infusion of glucose to maintain a constant blood glucose level of 120 ± 5 mg/dL as determined every 5 min by a glucometer. A second US imaging session was done towards the end of the 2 h clamp procedure. Using a clinical US scanner (Acuson Sequoia 512, Siemens Healthcare, Mountain View, CA) equipped with a 15L8 linear transducer array and operating in a nonlinear contrast mode with a center frequency of 10 MHz, CEUS images were collected for 10 min at 15 frames per sec. Potential MB destructions were minimized using a mechanical index (transducer output) less than 0.2. CEUS images depth x width of 8 x 16 mm (121 x 281 pixels) were saved for offline processing.

### 5.2.2 High Resolution CEUS Imaging

The image processing strategy illustrated in Figure 5.1 starts with steps that are similar to methods used during SR-US image generation. The first frame of each CEUS dataset was subtracted from subsequent frames to normalize for any background tissue signal [10]. The tissue and MB signals were then separated using a singular value decomposition filter (SVD) [20], [21]. This method assumes that the US signal consists of three components, namely clutter, blood, and noise [20]. High spatiotemporal coherence in the clutter (tissue) signal compared to the low spatiotemporal coherence in the MB signal allows for removing the tissue signal from every frame before localization of MBs and the creation of a CEUS-derived maximum intensity projection (MIP) image. The frames with detected MB signals were binarized using a threshold, and a connected component analysis was applied to isolate individual MBs as described previously [7]. In short, a

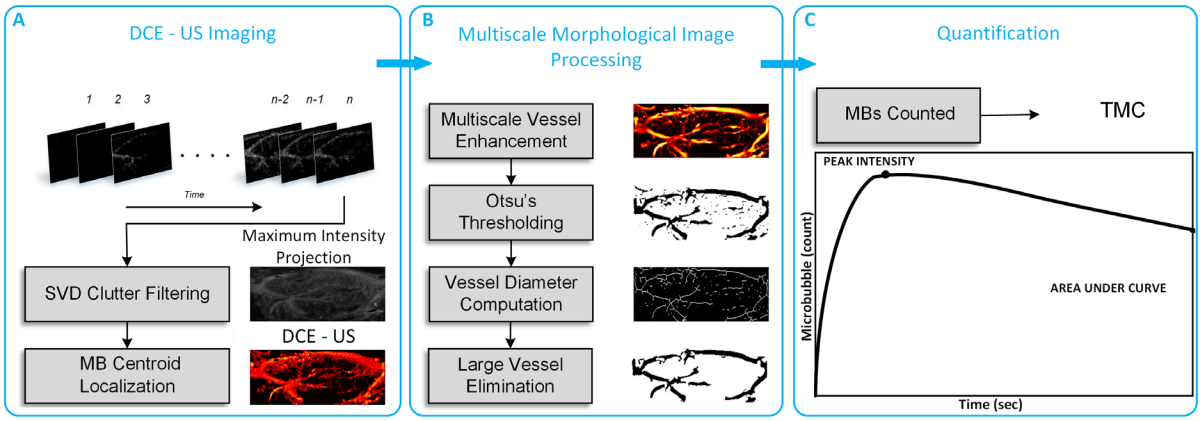


Figure 5.1. A new image processing approach for quantification of microvascular networks was developed and consists of three main components. After (A) acquisition of a series of dynamic contrast-enhanced ultrasound (DCE-US) images, singular value decomposition (SVD) filtering is used to remove any residual tissue clutter signal before microbubble (MB) localization. (B) Morphological image processing is then performed before computation of individual microvessel diameters and selective elimination of larger vessels. After vessel thresholding from the region-of-interest (ROI), structural parameters are quantified. (C) Tissue perfusion parameters are then derived from a time-MB count (TMC) curve. Outcomes of each processing step illustrate representative results.

comparison with an empirically defined point spread function (PSF) of an isolated MB was used to reject any clustering as isolated MBs and their centroids were accumulated at each pixel location throughout the stack of frames. The CEUS MIP images contains spatial and temporal information of MB density at each pixel location in a single image [12]. Custom software was developed in MATLAB (Mathworks Inc, Natick, MA) installed on an Alien Aurora desktop computer (Dell Inc, Round Rock, TX), and parallel processing was performed to reduce computation time.

### 5.2.3 Multiscale Vessel Enhancement

This section introduces our novel image processing strategy that uses multiscale and morphological image processing operations to provide the functionality of vessel size thresholding for improved quantification of the acquired CEUS images.

A multiscale vessel enhancement filter was applied to detect the larger vessels from the CEUS MIP image [22]. This method considers vessels as tubular structures (shapes) in 2D images. Tubular shapes were detected by the proportional relationship between the eigenvalues of the Hessian matrix derived from the image for a specific point. The curvature of the objects in the image at that point were used to detect the tubular shapes. Specifically, high curvature in one direction and low curvature in the orthogonal direction was defined as a vessel. The derivatives of the image were obtained using derivatives of Gaussian convolutions. By applying Gaussian kernels with different sizes, vessels within a specific range of scales were found. A vesselness function $\boldsymbol{V_o(\gamma)}$ defined as [22]:

$$V_o(\gamma) = \begin{cases} 0 & if\ \lambda_2 > 0 \\ exp\left(-\frac{R_B{}^2}{2\beta^2}\right)\left(1 - exp\left(-\frac{S^2}{2c^2}\right)\right) \end{cases}, R_B = \frac{|\lambda_1|}{|\lambda_2|}, S = \sqrt{\sum_{j=1}^{2} \lambda_j^2} \quad (5.1)$$

where $\lambda_{1,2}$ are eigenvalues of the Hessian matrix from the image, $R_B$ defines either a blob-like or tubular pattern, and S defines the structureness, has higher values for tubular structures in 2D and minimizes the impact of the image noise. Here, γ scales the Gaussian kernels and the β and c are filter sensitivity regularization parameters. After enhancing the tubular structures of an image, Otsu's global thresholding method [23] was used to create corresponding binary images as preparation for the morphological image processing steps given in Figure 5.1.

### 5.2.4 Morphological Image Processing and Structural Quantification

We used morphological image processing operations to build our vessel isolation algorithm, which is then used to assess changes in response to insulin in healthy versus diseased microvascular networks. Based on mathematical set theory, morphological image processing was applied to extract image components for representing and describing region shapes [24]. Using binarized images, morphological image processing methods were intensity invariant and relied on pixel locations. In this case, foreground pixels represent vessels and background pixels represent non-vessels. The 8-connectivity of the pixels that represent an object in the image contained the information about its geometric shape.

Vessel segments identified as connected components had their centerlines detected using a thinning algorithm while preserving their topology [25], [26]. For each foreground pixel on the centerline, the nearest background pixel was found using distance transform. Figure 5.2 shows how the Euclidian distance ($D_e$) between the centerline pixel ($u$) and the edge pixel ($v$) with coordinates ($x$, $y$) and ($k$, $l$), respectively, was computed as the radius ($r$) at $u$. A function $D$ used as a metric (distance measure) for the pixels $u$, $v$, and $z$ with the criteria: $D(u,v) \geq 0,\ D(u,v) =$

$0\ iff\ u = v,\ D(u,v) = D(v,u), D(u,v) \leq\ D(u,z) + D(z,v)$. The latter criterion ensures that the distance between *u* and *v* is always the minimum even if there is another ways to reach the pixel *v* starting from the pixel *u* going over the pixel *z*.

$$r = D_e(u,v) = \sqrt{(x-k)^2 + (y-l)^2} \tag{5.2}$$

Multiplying equation (2) by two provided an estimation of the diameter for the respective vessel segment at the specific centerline point. Mean vessel diameter was computed by averaging all values of vessel diameter computed from each pixel along the vessel centerline. The full width half maximum method (FWHM), which is the reference standard for vessel diameter estimations, was used to validate our diameter measurements [27]. Once all average diameters for vessel

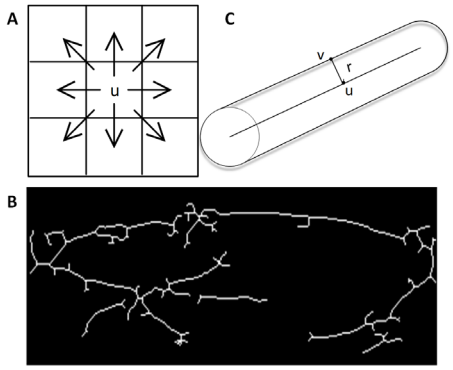


Figure 5.2. Morphological image processing methods using (A) 8-pixel connectivity of the arbitrary pixel u to form its connected components, then (B) detection each vascular structure centerline before (C) computing vessel diameter as the distance from each centerline to the closest edge pixel.

segments were computed, we were able to isolate vessels from the CEUS MIP image based on the vessel diameter threshold, Figure 5.3.

Perfusion and morphology parameters were compared using the full image that included all vessels as $ROI_{FULL}$, as well as for vessels with diameters less than 300, 200, and 150 µm, where these latter three groups are referred to hereafter as thresholded vessel groups. While our method allows to a microvascular perfusion and morphology analysis for any vessel diameter threshold, these three thresholds were selected based on two criteria: (1) minimum of the largest vessel diameters and the (2) different vessel diameter ranges. First, largest vessel diameters from the individual CEUS images were identified and the minimum, e.g., 300 µm, was selected as the threshold to exclude larger vessels from all CEUS images. Second, the 200 and 150 µm thresholds helped to exclude vessel groups of different diameter ranges. After removal of the largest vessels, we removed a vessel group with diameter range of 100 µm, i.e., from 200 µm to 300 µm, and

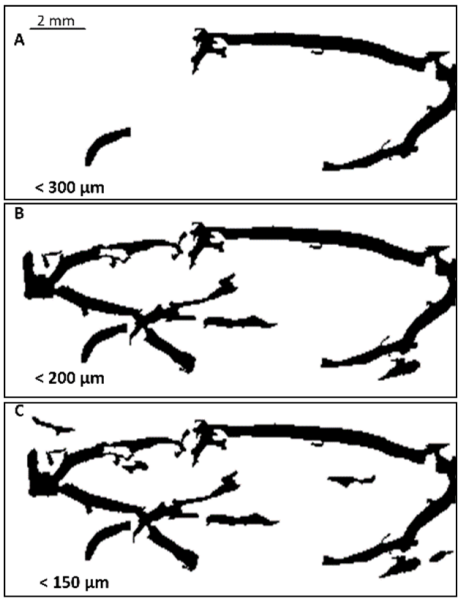


Figure 5.3. Thresholded vessel groups for perfusion parametric analysis using MB density over time for each white pixel location and zero for each black pixel. White regions contain the vessels that are smaller than (A) 300, (B) 200, and (C) 150 µm.

another vessel group with diameter range of 50 µm, i.e., from 150 µm to 200 µm. Morphology parameters were then extracted from the binarized and skeletonized CEUS MIP images and

included vessel-to-tissue ratio (VR) and number of vessels (NV) [10]. Both parameters can indicate increased microvascular openings or impaired microvascular recruitment. VR is defined as $VR = \frac{V_{Pixels}}{ROI_{Pixels}} \times 100$ where $V_{Pixels}$ is the number foreground pixels and $ROI_{Pixels}$ is the number of all pixels for the vessel group [10]. Using the skeletonized image, first the branching points were identified as pixels with more than two foreground neighbors. Individual connected components were then detected by removing the branching points. The number of individual vessel segments as connected components after the removal of the branching points (bifurcations) was used as the NV metric [10]. Increased NV, as well as increased VR, indicate a more complex vascular network. Note that the physical pixel size was 55 μm and this limits the resolution for extracting the structural parameters.

### 5.2.5 Functional Quantification

From the time sequence CEUS images, individual MBs detected within the ROI can be enumerated to produce a time MB count curve (TMC) [7]. It has been shown previously that TMC-derived values have less variance compared to the more traditional time intensity curve (TIC)-derived measurements. Each TMC was fit with a smoothing spline *s* that finds the minimum value $Z$ of

$$Z = a \sum_i w_i (y_i - s(x_i))^2 + (1 - a) \int \left(\frac{d^2 s}{dx^2}\right)^2 dx \tag{5.3}$$

where $a$ is the smoothing parameter, $w$ is weight, $y$ is the MB density and $s(x)$ is the fitted MB density value at time $i$ in units of sec. Parameters derived from the fitted TMC curve included the area under the curve (AUC) and peak MB count (IPK) values. AUC is a surrogate measurement

for blood volume and IPK is a surrogate measurement for blood velocity, where both of these measures are indicative of microvascular recruitment.

### 5.2.6 Statistical Tests

Perfusion and microvascular morphology parameters from both lean and obese groups of mice were summarized as mean ± standard error (SE). Longitudinal measurements of individual parameters were compared using a paired *t*-test for each group separately. Group comparisons were performed using a two-sample *t*-test. For the non-normal distributions Wilcoxon rank-sum test was applied.

## 5.3 Results

The experimental study involved CEUS imaging the microvascular features of skeletal muscle tissue of lean and obese mice. Before the US imaging sessions, the body weight (age) for the lean and obese animals was 25.1 ± 0.8 g (12.8 ± 0.4 wks) and 51.8 ± 1.1 g (27.0 ± 0.7 wks), respectively ($p < 0.001$). In the obese animals, there was a higher fasting blood glucose level than in the lean animals ($p < 0.001$). These values indicate that the obese mice have glucose intolerance and insulin resistance.

CEUS imaging was applied at baseline and again near the end of a 2 h hyperinsulinemic-euglycemic clamp procedure. Microvascular recruitment of smaller vessel segments during this 2-h period can be noted from inspection of Figure 5.4 for a lean subject. The vessels within the white box are considered small (with a diameter below 300 μm) and increased microvascularity in this area is visible at the second time point. Figure 5.5 shows the results of an obese subject where the microvascular recruitment was impaired at the second time point.

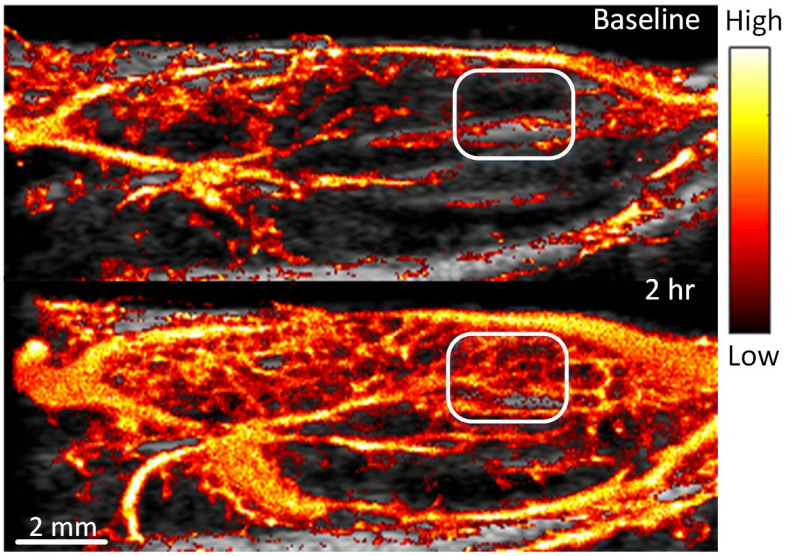


Figure 5.4. Representative DCE-US images of the microvascular network in the hindlimb of a lean mouse (baseline, top) and after application of an hyperinsulinemic-euglycemic clamp (2 h, bottom). Results shows obvious dilatations and recruitment of smaller microvascular structures (< 300 μm, white box).

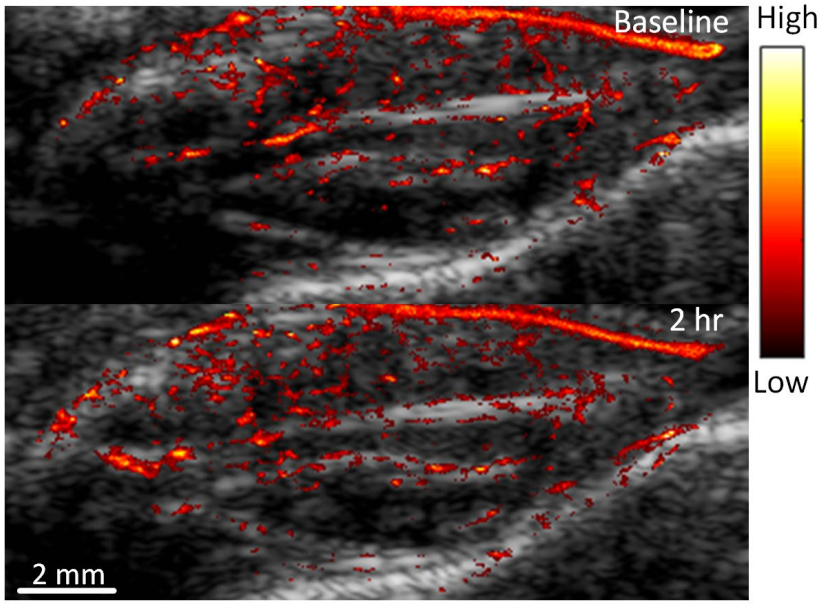


Figure 5.5. Representative DCE-US images of the microvascular network in the hindlimb of an obese mouse (baseline, top) and after application of an hyperinsulinemic-euglycemic clamp (2 h, bottom). Results show microvascular impairment.

Representative grayscale US and CEUS-based MIP images after having the SVD filter applied

are depicted in Figure 5.6 for a lean and in Figure 5.7 for an obese subject. Removal of tissue clutter made the MB signal more pronounced in the MIP image. The multiscale vessel enhancement filter helped to delineate the large vessels and was used as a preprocessing step before

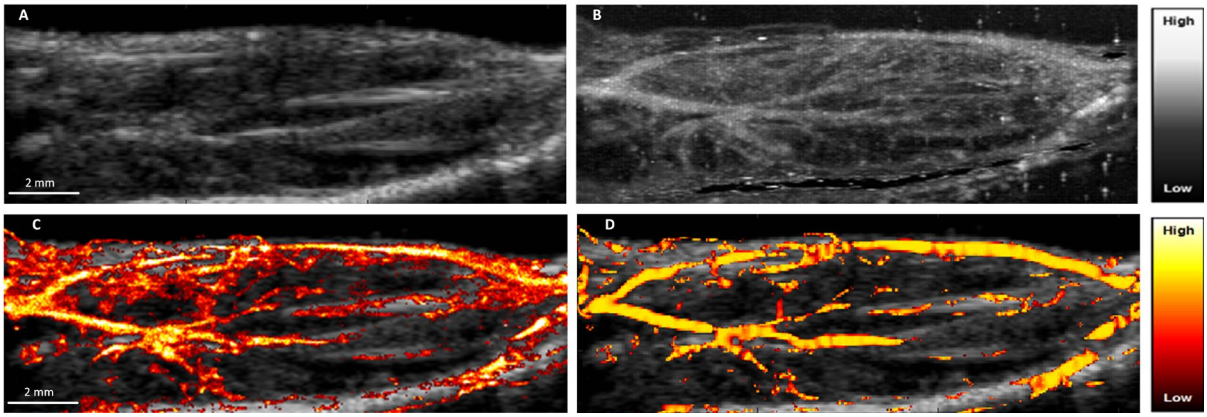


Figure 5.6. Representative lean subject. (A) Grayscale ultrasound (US) images of skeletal muscle tissue and co-registered (B) DCE-US-derived maximum intensity projection (MIP) images depicting the microvascular networks (C) after SVD filtering and (D) after vessel enhancement. Color bars denote image intensity.

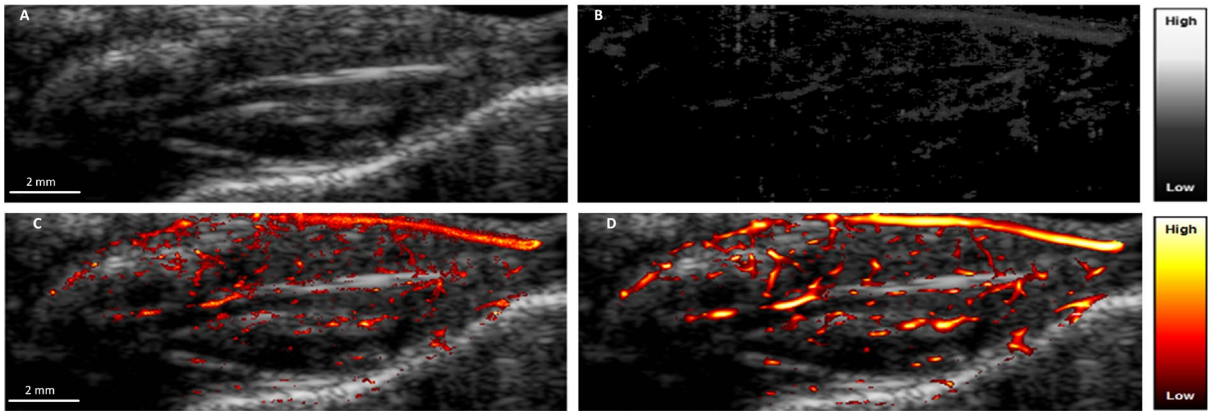


Figure 5.7. Representative obese subject. (A) Grayscale ultrasound (US) images of skeletal muscle tissue and co-registered (B) DCE-US-derived maximum intensity projection (MIP) images depicting the microvascular networks (C) after SVD filtering and (D) after vessel enhancement. Color bars denote image intensity.

segmentation. Figure 5.8 and Figure 5.9 show representative TMC curves from a lean and obese mouse, respectively. TMC curves were derived using either an $ROI_{FULL}$, which include all of the

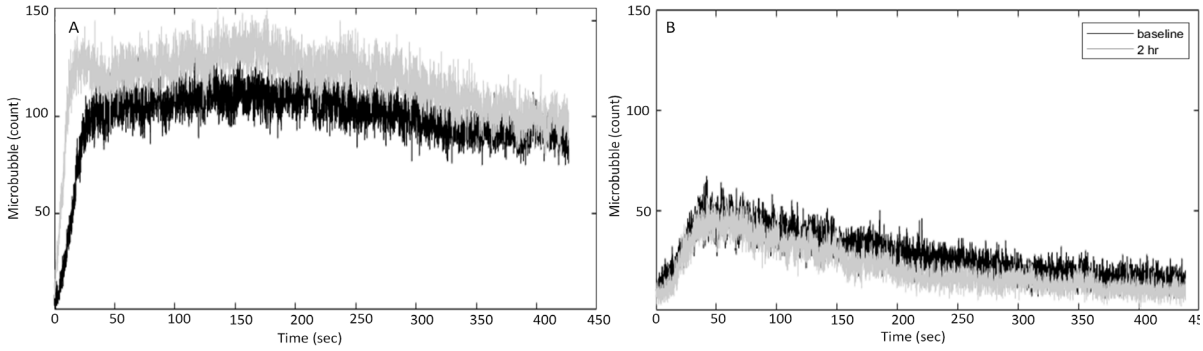


Figure 5.8. Representative TMCs for an obese subject showing the time history of MBs detected. Skeletal muscle tissue perfusion in an obese mouse was assessed using the (A) full ROI and then from the same (B) ROI that only included vessels with diameters below 150 µm.

microvasculature structures, and the thresholded group that isolated and restricted the analysis to only those vessels with diameters less than 150 µm. Note the more pronounced change in the TMC amplitude from Figure 5.8 in the latter after application of the insulin challenge.

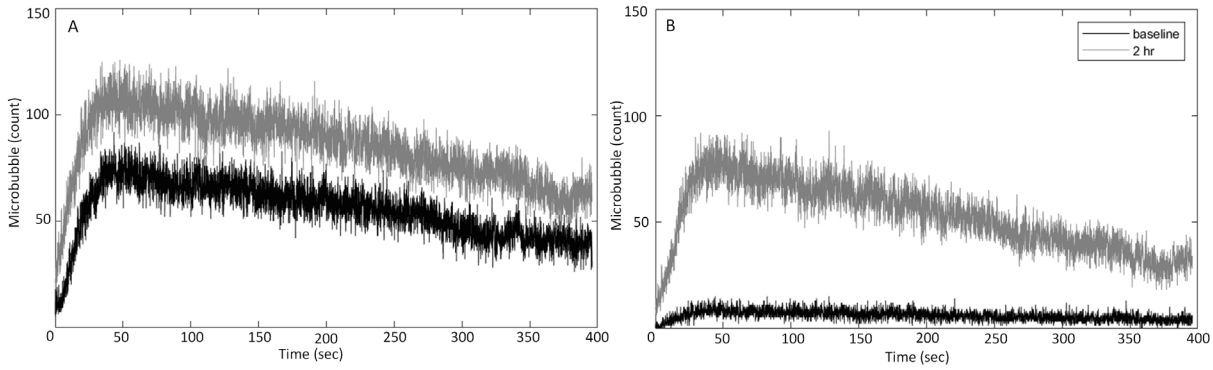


Figure 5.9. Representative TMCs for a lean subject showing the time history of MBs detected. Skeletal muscle tissue perfusion in a lean mouse was assessed using the (A) full ROI and then from the same (B) ROI that only included vessels with diameters below 150 µm. Baseline values in (B) were closer to zero and larger differences were observed between baseline and 2 h after application of a hyperinsulinemic-euglycemic clamp and microvascular size thresholding.

Figure 5.10 summarized differences between the lean and obese groups regarding percent increases above baseline at 2 h. Using all of the vessels, e.g., full ROI, the differences between

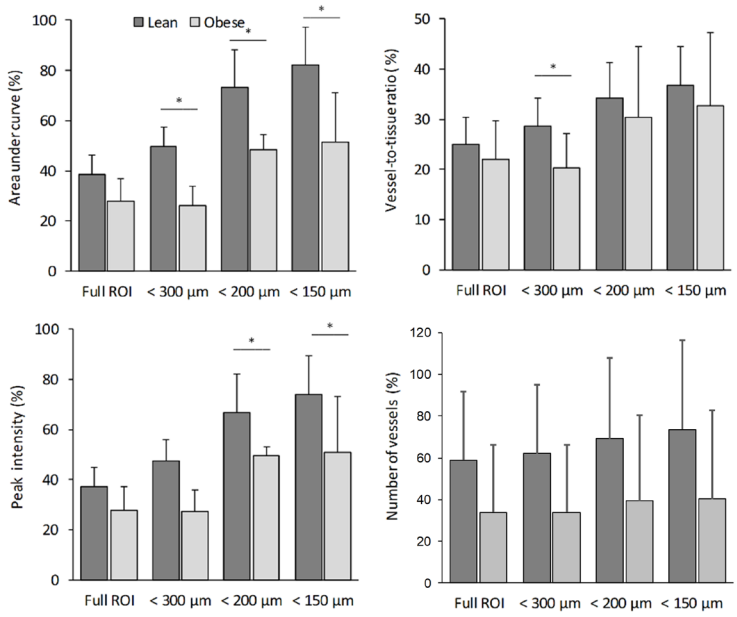


Figure 5.10. Summary of changes in DCE-US image-derived tissue perfusion and microvascular morphology measurements. Elimination of larger vessels from the image analysis process (above 300 µm in diameter) reveals a general increase in skeletal muscle microvascular perfusion and morphology parametric changes relative to baseline. A * denotes $p < 0.05$ relative to obese measures.

lean and obese group were not significant while significant differences were observed when using the thresholded vessel groups for the parameters AUC, IPK, and VR. All of the parameters demonstrated an increasing trend for the lean group compared to the obese group for smaller vessel sizes. The ability to detect differences in functional and structural parameter responses to insulin between lean and obese groups increased as the vessel diameter threshold was reduced. In short, our method allowed the observation of longitudinal changes in vessel groups of varying size distribution in lean and obese mice after applying a hyperinsulinemic-euglycemic clamp, which is a common procedure for evaluating insulin resistance in skeletal muscle tissue.

## 5.4 Discussion

Reliable analysis of smaller vessels is challenging when using CEUS imaging. In this study, a series of image processing algorithms were presented for multiscale analysis of CEUS images to discern microvascular properties in skeletal muscle after application of a hyperinsulinemic-euglycemic clamp. This procedure produced microvascular recruitment in the lean animal group, whereas it highlighted insulin resistance in the obese subjects, which is common condition associated with type 2 diabetes. A general quantification of impaired microvascular function in skeletal muscle may help researchers better understand various disease types [2], [4], [6], [28]–[30]. Previous research has confirmed that smaller vessels are more impacted by diabetic disease and treatment than larger vessels [5], [30]. In our study, the removal of larger vessels was crucial during the analysis of microvascular function and helped improve the sensitivity of CEUS for the detection of changes in skeletal muscle tissue.

The novelty of our work lies in the ability to isolate vessels at multiple scales based on their morphology from CEUS images. This was previously not possible because CEUS lacked the resolution necessary for applying morphological image processing operations. Previous work used knowledge of blood velocity information [15], [27], [29] or manually drawn ROIs [7], [16], [17] to help avoid larger vessels during any subsequent image analysis. The ROI drawing process is subjective and has been recognized as a major limitation in several prior studies [7], [16], [17].

During our study, it was found that the CEUS-derived TMC data from the different thresholded vessel groups exhibited smaller IPK values at 2 h after start of the hyperinsulinemic-euglycemic clamp because the larger vessels were removed from the image analysis. At the 2 h time-point relative to baseline, differences of AUC values were more pronounced in the thresholded vessel

group compared to the image including all vascular information. This specific vessel size selection process enabled us to use perfusion data from a specific group of vessels at the scale of interest. The relative differences between microvasculature properties in lean and obese mice was found to be more pronounced using our image processing method as compared to utilizing microvascular information from the entire ROI, further highlighting the increased sensitivity of the analysis.

In addition to the more traditional tissue perfusion parameters, the present work also evaluated the use of microvascular morphologic parameters for quantification of defects associated with type 2 diabetes. Large variations in these structural parameter values may have been caused by limited sample size. Additionally, structural measurements were limited to the physical pixel size of 55 μm. Increasing the spatial resolution of the CEUS images will further enhance the ability to detect changes in structural parameters. A higher image resolution will also allow data analysis comparing distinct ranges of vessel sizes, which may be more informative from both physiologic and pathophysiologic perspectives.

A potential limitation of this study is that it quantified functional and structural alterations in microvascular networks using only a single US imaging plane. Since the structural pattern of microvascular architecture is inherently manifests in volume space, a 3D approach could provide additional information of value. For example, a single bright pixel of a vessel that is placed orthogonal to the coronal slice is not considered as a vessel in 2D analysis while the 3D reconstruction of the same vessel from many coronal slices would visualize the entire vessel, which would be counted in the image analysis. We validated our diameter measurements with the FWHM method, which is the gold standard for vessel diameter estimation [27]. Since the relative changes in the images were of greater importance than the absolute diameter measurements, the results of

our analysis were not affected. The accuracy of the vessel diameter measurements could not be estimated which is a limitation of this study. During our study, we also fixed the transducer to have a consistent US imaging plane. Notwithstanding, it has been shown that the remaining free form deformations may further affect image quantifications. Motion artifacts from the CEUS images have been reported to result in duplicate visualizations of a single vessel [31] or random fractions on a long vessel [32]. We hypothesize that the results for the structural parameters might have been more affected by motion artifacts compared to the functional parameters. A motion correction method before quantification and a volumetric approach could help resolve these potential limitations.

### 5.5 Conclusion

Multiscale morphological image processing of CEUS data introduces a new vessel sized-based approach for the quantification of parametric information that details properties of a microvascular network in states of health and disease. Collectively, CEUS image-derived microvascular morphology and perfusion parameters detected differential longitudinal changes in skeletal muscle tissue after application of a hyperinsulinemic-euglycemic clamp procedure in lean and obese subjects.

### 5.6 References

[1] World Health Organization, *Global report on diabetes*. Geneva, Switzerland: World Health Organization, 2016.

[2] K. Tanigaki *et al.*, "Hyposialylated igg activates endothelial igg receptor fcγriib to promote obesity-induced insulin resistance," *The Journal of Clinical Investigation*, vol. 128, no. 1, pp. 309–322, 2016.

[3] T. H. IJzerman, N. C. Schaper, Tom. Melai, K. Meijer, P. J. B. Willems, and H. H. C. M. Savelberg, "Lower extremity muscle strength is reduced in people with type 2 diabetes, with and without polyneuropathy, and is associated with impaired mobility and reduced quality of life," *Diabetes Research and Clinical Practice*, vol. 95, no. 3, pp. 345–351, 2012.

[4] I. Martín-Timón, C. Sevillano-Collantes, A. Segura-Galindo, and F. J. del Cañizo-Gómez, "Type 2 diabetes and cardiovascular disease: Have all risk factors the same strength?," *World Journal of Diabetes*, vol. 5, no. 4, pp. 444–470, 2014.

[5] T. R. Porter, "Capillary blood flow abnormalities in the skeletal muscle and microvascular complications in diabetes: lessons that cannot be learned from larger vessels," *Journal of the American College of Cardiology*, vol. 53, no. 23, pp. 2184–2185, 2009.

[6] J. P. Glotzbach, V. W. Wong, and G. C. Gurtner, "Neovascularization in diabetes," *Expert Review of Endocrinology & Metabolism*, vol. 5, no. 1, pp. 99–111, 2010.

[7] D. Ghosh *et al.*, "Super-resolution ultrasound imaging of the microvasculature in skeletal muscle: a new tool in diabetes research," *Proc IEEE Ultrason Symp (IUS)*, pp. 1–4, 2017.

[8] K. Hoyt *et al.*, "Determination of breast cancer response to bevacizumab therapy using contrast-enhanced ultrasound and artificial neural networks," *Journal of Ultrasound in Medicine*, vol. 29, no. 4, pp. 577–585, 2010.

[9] R. Saini and K. Hoyt, "Recent developments in dynamic contrast-enhanced ultrasound imaging of tumor angiogenesis," *Imaging in medicine*, vol. 6, no. 1, pp. 41–52, 2014.

[10] K. Hoyt, H. Umphrey, M. Lockhart, M. Robbin, and A. Forero-Torres, "Ultrasound imaging of breast tumor perfusion and neovascular morphology," *Ultrasound in Medicine & Biology*, vol. 41, no. 9, pp. 2292–2302, 2015.

[11] K. Hoyt, A. Sorace, and R. Saini, "Quantitative mapping of tumor vascularity using volumetric contrast enhanced ultrasound," *Investigative Radiology*, vol. 47, no. 3, pp. 167–174, 2012.

[12] K. Hoyt, "Parametric imaging of tumor perfusion and neovascular morphology using ultrasound," *Proc. SPIE Medical Imaging*, p. 941911, 2015.

[13] J. R. Lindner, "Microbubbles in medical imaging: current applications and future directions," *Nature Reviews Drug Discovery*, vol. 3, no. 6, pp. 527–533, 2004.

[14] C. Errico *et al.*, "Ultrafast ultrasound localization microscopy for deep super-resolution vascular imaging," *Nature*, 2015.

[15] D. Dawson *et al.*, "Vascular recruitment in skeletal muscle during exercise and hyperinsulinemia assessed by contrast ultrasound," *American Journal of Physiology-Endocrinology and Metabolism*, vol. 282, no. 3, pp. E714–E720, 2002.

[16] M. G. Clark, "Impaired microvascular perfusion: a consequence of vascular dysfunction and a potential cause of insulin resistance in muscle," *American Journal of Physiology - Endocrinology and Metabolism*, vol. 295, no. 4, pp. E732–E750, 2008.

[17] C. Manrique and J. R. Sowers, "Insulin resistance and skeletal muscle vasculature: significance, assessment and therapeutic modulators," *Cardiorenal Medicine*, vol. 4, no. 3–4, pp. 244–256, 2014.

[18] I. Özdemir and K. Hoyt, "Morphological image processing for multiscale analysis of super-resolution ultrasound images of tissue microvascular networks," *Proc. SPIE Medical Imaging*, vol. 10955, p. 1095505, 2019.

[19] S. Sirsi and M. Borden, "Microbubble compositions, properties and biomedical applications," *Bubble science engineering and technology*, vol. 1, no. 1–2, pp. 3–17, 2009.

[20] C. Demené *et al.*, "Spatiotemporal clutter filtering of ultrafast ultrasound data highly increases doppler and fultrasound sensitivity," *IEEE Transactions on Medical Imaging*, vol. 34, no. 11, pp. 2271–2285, 2015.

[21] D. Ghosh, F. Xiong, S. R. Sirsi, P. W. Shaul, R. F. Mattrey, and K. Hoyt, "Toward optimization of in vivo super-resolution ultrasound imaging using size-selected microbubble contrast agents," *Medical Physics*, vol. 44, no. 12, pp. 6304–6313, 2017.

[22] A. F. Frangi, W. J. Niessen, K. L. Vincken, and M. A. Viergever, "Multiscale vessel enhancement filtering," *SpringerLink*, pp. 130–137, 1998.

[23] N. Otsu, "A threshold selection method from gray-level histograms," *IEEE Transactions on Systems,Man and Cybernetics*, no. 9, 1979.

[24] R. C. Gonzalez and R. E. Woods, *Digital Image Processing*, 4th ed. New York, NY, USA: Pearson, 2018.

[25] T.-C. Lee, "Building skeleton models via 3-D medial surface/axis thinning algorithms," *CVGIP*, vol. 56, pp. 462–478, 1994.

[26] M. Kerschnitzki *et al.*, "Architecture of the osteocyte network correlates with bone material quality," *Journal of Bone and Mineral Research*, vol. 28, no. 8, pp. 1837–1845, 2013.

[27] H. Bouma, J. O. Bescós, A. Vilanova, and F. A. Gerritsen, "Unbiased vessel-diameter quantification based on the FWHM criterion," *Proc. SPIE Medical Imaging*, pp. 1–4, 2007.

[28] M. A. Vincent *et al.*, "Microvascular recruitment is an early insulin effect that regulates skeletal muscle glucose uptake in vivo," *Diabetes*, vol. 53, no. 6, pp. 1418–1423, 2004.

[29] S. M. Chadderdon *et al.*, "Temporal changes in skeletal muscle capillary responses and endothelial-derived vasodilators in obesity-related insulin resistance," *Diabetes*, vol. 65, no. 8, pp. 2249–2257, 2016.

[30] L. Womack, D. Peters, E. J. Barrett, S. Kaul, W. Price, and J. R. Lindner, "Abnormal skeletal muscle capillary recruitment during exercise in patients with type 2 diabetes mellitus and microvascular complications," *Journal of the American College of Cardiology*, vol. 53, no. 23, pp. 2175–2183, 2009.

[31] S. Harput *et al.*, "Two-stage motion correction for super-resolution ultrasound imaging in human lower limb," *IEEE Transactions on Ultrasonics, Ferroelectrics, and Frequency Control*, vol. 65, no. 5, pp. 803–814, 2018.

[32] I. Oezdemir, C. Shaw, J. R. Eisenbrey, and K. Hoyt, "Improved quantitative contrast-enhanced ultrasound imaging of hepatocellular carcinoma response to transarterial chemoembolization," *Proc IEEE Int Symp Biomedical Imaging (ISBI)*, pp. 1737–1740, 2019.

# CHAPTER 6

# CONTRAST-ENHANCED ULTRASOUND IMAGING OF ACUTE CHANGES IN PANCREATIC CANCER FOLLOWING TARGETED HYALURONAN TREATMENT

Authors – Ipek Oezdemir, Kulsoom Javed, Girdhari Rijal, Kenneth Hoyt

The Department of Bioengineering, BSB 11
The University of Texas at Dallas
800 West Campbell Road
Richardson, TX 75080-3021

* Adapted from © 2019 IEEE. Reprinted, with permission, from Ipek Oezdemir, Kulsoom Javed, Girdhari Rijal, Kenneth Hoyt, Contrast-enhanced ultrasound imaging of acute changes in pancreatic cancer following targeted hyaluronan treatment, 2019 IEEE International Ultrasonics Sympsoium (IUS), October 2019.

Author contribution: Ipek Ozdemir (myself) was responsible for the experimental design, the data acquisition, data analysis, and the manuscript preparation presented here.

The purpose of this study was to monitor acute changes in pancreatic tumor perfusion with contrast-enhanced ultrasound (CEUS) imaging following targeted hyaluronan (HA) treatment. Intratumoral accumulation of HA is one of contributing factors that can lead to an increased tumor interstitial pressure (TIP). These elevated TIP levels can hinder delivery of chemotherapeutic drugs and cause treatment failure. For this study, pancreatic cancer-bearing mice were imaged at baseline and again at 2 h after intravenous administration of physiological saline (control group) or PEGPH20, which targets HA (therapy group). CEUS data were collected for 5 min and the temporal sequence was first analyzed using a singular value filter (SVF) to remove any background clutter signal. Given the time history of contrast agent flow, a tumor perfusion parametric analysis was performed. A series of morphological image operations was applied to quantify structural features of the tumor angiogenic network including vessel count, density, length, diameter, tortuosity, and branching points. After imaging, animals were euthanized, and tumors excised for histological processing. Acute microvascular changes were found at 2 h after drug administration as confirmed by CEUS imaging. Further, histologic analysis of tumor sections revealed lower HA accumulation in the therapy group animals. Overall, these findings suggest that CEUS imaging of acute changes in tumor perfusion may help identify an optimal window whereby follow-up chemotherapeutic drug dosing would be more effective.

## 6.1 Introduction

Pancreatic cancer accounts for about 3% of all cancers in the US and about 7% of all cancer deaths [1]. Effective drug delivery to the bulk tumor can be profoundly impacted by excessive accumulation of hyaluronan (HA), which is a component of the extracellular matrix [2]. Increased HA is associated with high tumor interstitial pressure (TIP), and vascular collapse [3]–[6]. These physical conditions can compromise microvascular function and impede chemotherapeutic drug delivery. Recently, a PEGylated version of recombinant human hyaluronidase (PEGPH20) has been described. When administered systemically PEGPH20 was shown to degrade HA levels in pancreatic cancer and improve drug delivery [4]–[8].

Real-time contrast-enhanced ultrasound (CEUS) is a noninvasive imaging technique that uses an intravascular tracer (microbubble, MB) to help visualize tumor microvascular networks [9]. These CEUS images can then be analyzed to extract both tumor perfusion and microvascular morphology features [10]–[14]. To that end, CEUS imaging has been used to assess the tumor response (or lack thereof) to gemcitabine plus PEGPH20 therapy [5]. This study revealed that this treatment protocol produced a positive response in pancreatic cancer-bearing mice after only one cycle of combination therapy. Consistent with known mechanisms, treated tumors exhibited decreased proliferation and increased apoptosis of primary cancer cells compared to placebo control. Using a novel image processing strategy applied to CEUS data, this paper aims to expand on earlier findings by evaluating the acute functional and structural changes of tumor microvasculature after administration of PEGPH20.

## 6.2 Materials and Methods

All studies were approved by the Institutional Animal Care and Use Committee (IACUC) at the University of Texas at Dallas. Human BxPC3/HAS3 pancreatic cancer cells were implanted in the hindlimb (2 million per site near the tibia) of six-week-old male athymic nude mice (Charles River Laboratories, Wilmington, ME). Once tumors reached a size of 10 to 12 mm, animals were assigned to one of two groups, namely, control or therapy ($N$ = 2 per). CEUS imaging of each tumor was performed using a clinical system (Acuson Sequoia 512, Siemens Healthcare, Mountain View, CA) equipped with a 15L8 linear transducer array. The transducer was fixed using a ring stand to maintain the same imaging plane during repeat measurements. Each animal received a 50 μL bolus injection of MBs (Definity, Lantheus Medical Imaging, N Billerica, MA) via a tail vein catheter. Using a MB sensitive imaging mode, a low transmit power (mechanical index, MI, less than 0.2) helped minimize contrast agent destruction.

Each tumor was imaged by CEUS for 5 min at baseline and again at 2 h after systemic administration of a matched dose of saline (control) or PEGPH20 (therapy) (1.0 mg/kg, Halozyme Therapeutics, San Diego, CA). The body temperature of each animals was monitored during the entire study using a rectal probe regulated by a homeothermic controller (Kent Scientific Corp, Torrington, CT).

### 6.2.1 Image Processing

Sequences of CEUS images were first processed using a singular value filter (SVF) to remove the clutter signal [11] followed by MB localization [15]. A maximum intensity projection (MIP) image was then created with the values for each pixel location from 8x interpolated CEUS images. This

step created high-resolution CEUS images from each imaging session. A spherical region-of-interest (ROI) of 100-pixel radius was placed on a hypoenhanced area of the tumor space (baseline images). A matched size ROI was used for all subjects. According to the mean intensity distribution as a function of time in this ROI, time-intensity curves (TICs) were created [16], [17]. Select tumor perfusion parameters were derived from TIC data, i.e., area under the curve (AUC) and peak intensity (IPK) [18]–[20].

To assess tumor microvascular morphology features, CEUS images were improved with a multiscale vessel enhancement filter, e.g., tubular structures in the image [21]. After binarization, a series of morphological image processing methods [22] were applied for computation of different structural metrics from tumor microarchitecture [23], e.g., number of branching points (NB), number of vessels (NV), mean vessel length (VL), mean vessel tortuosity (VT), mean vessel diameter (VD), and microvessel density (MVD) [14]. Note that only connected components having more than two pixels were considered as vessels for all the above-mentioned metrics.

### 6.2.2 Histology Analysis

Mice were euthanized and tumors were harvested after CEUS imaging at 2 h. Tumors were fixed in 10% formalin and tissue section were prepared from paraffin blocks. Sections were processed and stained for immunohistochemistry using anti-HA IgG horseradish peroxidase (HRP) conjugate and DAB substrate (Fisher Scientific, Waltham, MA). Five histology images were selected randomly from each group and used to quantify the color intensity of the HA stain.

### 6.2.3 Statistical Analysis

All experimental data was summarized as mean ± standard error when applicable. A linear regression analysis was performed between select functional and structural parameters. A 2-way Analysis of variance (ANOVA) was used to analyze the longitudinal measurements relative to absolute baseline values from histology data. A *p*-value less than 0.05 was considered statistically significant.

## 6.3 Results

From our CEUS image analysis, we report the changes in tumor perfusion and microvascular morphology parameters at baseline and 2 h for all of the individual subjects. Also, TICs and ROIs from representative subjects of each group are presented in this section. Tumor microvascular structural parameters increased at 2 h for the therapy group animals when compared to control measurements. CEUS image-based parametric values at baseline and 2 h are listed in Table 6.1.

Table 6.1. Functional and structural parameter values for each subject and timepoint

| | Control 1 | | Control 2 | | Therapy 1 | | Therapy 2 | |
|---|---|---|---|---|---|---|---|---|
| Parameter | Baseline | 2 h | Baseline | 2 h | Baseline | 2 h | Baseline | 2 h |
| IPK | 17.04 | 15.17 | 11.96 | 14.22 | 10.04 | 32.82 | 27.47 | 34.54 |
| AUC | 169.10 | 182.97 | 179.41 | 211.08 | 137.41 | 388.33 | 258.56 | 322.17 |
| NB | 0.00 | 0.00 | 5.00 | 6.00 | 0.00 | 8.00 | 0.00 | 4.00 |
| NV | 2.00 | 1.00 | 14.00 | 13.00 | 0.00 | 22.00 | 6.00 | 16.00 |
| VD | 0.00 | 0.00 | 0.07 | 0.03 | 0.00 | 0.10 | 0.01 | 0.05 |
| VT | 0.10 | 0.00 | 0.92 | 0.26 | 0.00 | 0.31 | 0.05 | 0.13 |
| VL | 22.07 | 1.00 | 38.59 | 17.19 | 0.00 | 19.55 | 11.87 | 14.20 |
| MVD | 0.01 | 0.01 | 0.08 | 0.03 | 0.00 | 0.13 | 0.02 | 0.06 |

IPK = Peak intensity, AUC =Area under curve, NB = Number of vessels, NV = Number of vessels, VD = Vessel diameter, VT = Vessel tortuosity, VL = Vessel length,

Two control subjects had slightly different starting values and both ended up with decreased values or no changes at 2 h after administration of saline. In contrast, the therapy subjects showed marked increased values at 2 h compared to the control group. Figure 6.1 depicts the qualitative changes in tumor microarchitecture for a representative control and therapy subject, respectively. Perfusion parameters indicate a considerably higher blood volume (AUC and IPK) for the therapy group

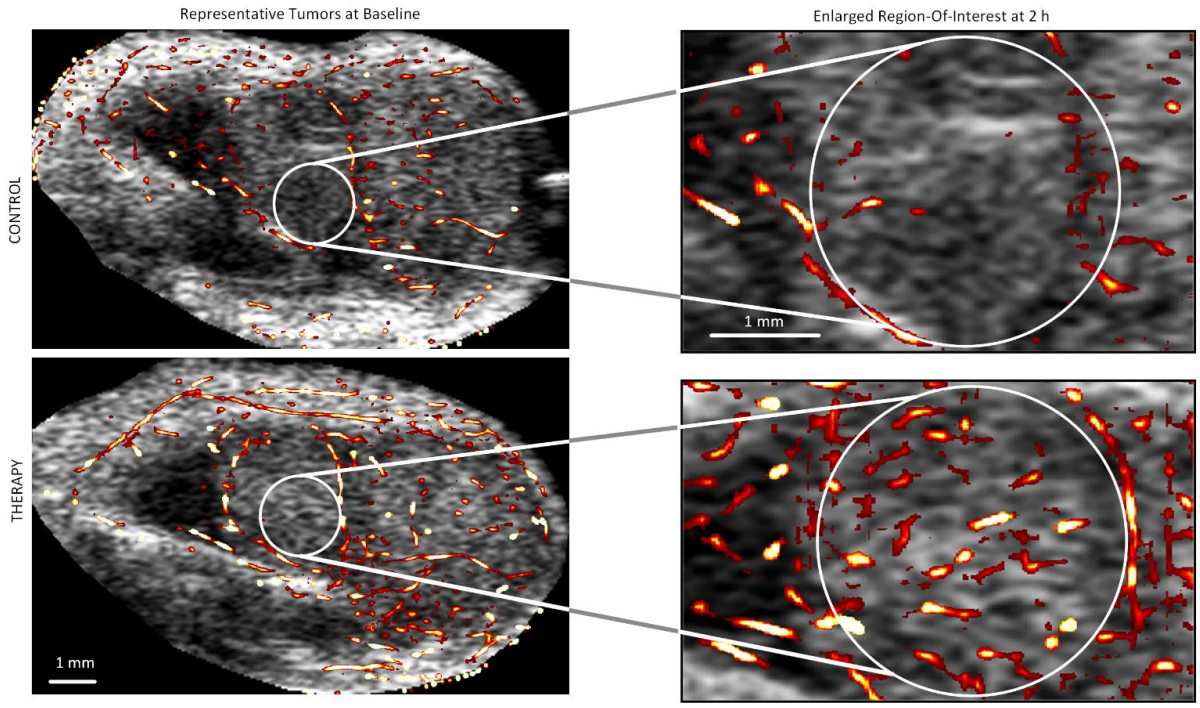


Figure 6.1. B-mode ultrasound (US) images of representative pancreatic cancer-bearing mice overlaid with contrast-enhanced US (CEUS) images. Images were acquired at baseline and again at 2 h after dosing with either targeted hyaluronan (therapy, PEGPH20 drug) or saline (control). An intratumoral region-of-interest (ROI, white) was manually selected to encompass an area with relatively low tissue perfusion

animals at 2 h after administration of PEGPH20, Figure 6.2. Figure 6.3 illustrates the linear relationship between tumor perfusion and microvascular morphology parameters. A significant correlation was observed between AUC and NV ($R^2$ = 0.64, $p$ = 0.01) suggesting the amount of MBs is proportional with the number of vessels. The same is true also for the AUC and MVD

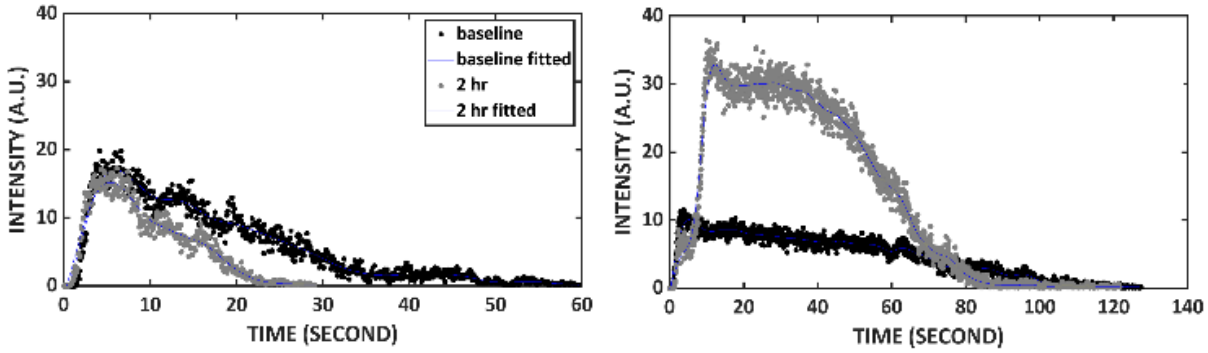


Figure 6.2. Time-intensity curves (TICs) for control (left) and therapy (right) subjects. Note CEUS-derived parameter increases for the therapy group animals compared to the control group at 2 h relative to baseline.

parameters ($R^2 = 0.58$, $p = 0.02$). In contrast, another functional parameter IPK showed a weak correlation with the structural parameters NV ($R^2 = 0.35$, $p > 0.10$) and MVD ($R^2 = 0.29$, $p < 0.16$), respectively. After further investigation, we found that having a large vessel can produce a similar

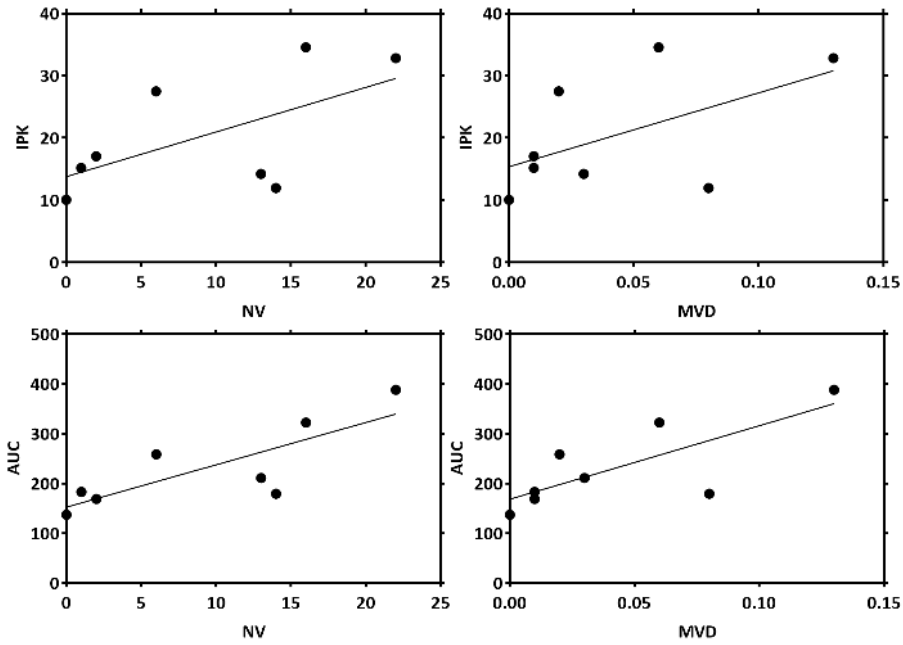


Figure 6.3. Linear relationship between CEUS-derived tumor blood volume (peak intensity, IPK; area under curve, AUC) and microvascular structure (number of vessels, NV; microvessel density, MVD) at 2 h.

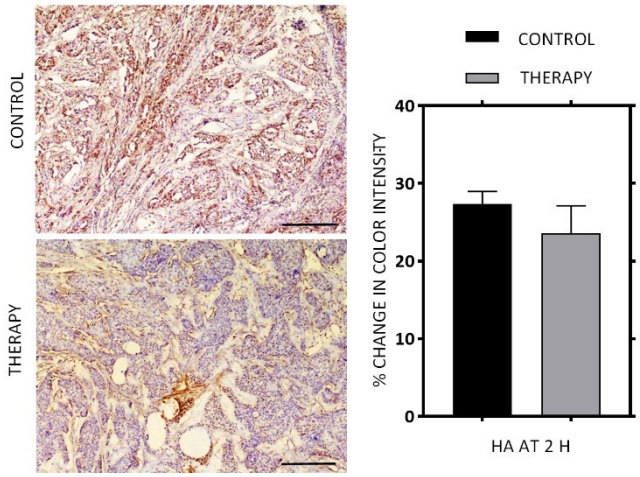


Figure 6.4. Histology images from pancreatic cancer-bearing mice at 2 h after being dosed with saline (control) or PEGPH20 (therapy). Sections were stained for HA (hyaluronan) accumulation and quantified as percent tumor cross-sectional area. Scale bar = 0.5 mm.

IPK value as having many small vessels. While our analysis did not discriminate based on microvessel size within the tumor ROI, if we focused our analysis on only the smaller blood vessels, we would expect an improved correlation between these CEUS image-based parametric measures. In short, these results suggest that tumors with a more extensive microvascular network have a corresponding increased tumor blood volume. CEUS imaging results were confirmed by histologic analysis of excised pancreatic tumor tissue samples, Figure 6.4. At 2 h after dosing with saline or PEGPH20, tissue samples exhibited a pronounced decrease in intratumoral HA levels when compared to control findings ($p < 0.0001$). Accumulation of HA is associated with the microvascular collapse and high TIP [3].

## 6.4 Discussion

This study can be improved in a few aspects. Specifically, the accuracy of the morphological parameters can be improved by removing the motion artifacts from the images before MB

localization [10]. Also, the quality of the high-resolution CEUS images could have been increased by a slower bolus injection and longer imaging sessions [13].

Previous studies have demonstrated that targeted HA degradation with PEGPH20 can help restore blood flow through previously collapsed microvascular segments and improve drug delivery [2], [5], [6]. In this study, preliminary results reveal that advantageous tumor changes after targeted HA treatment can also be monitored using CEUS images and parametric measurements of tumor perfusion and microvascular morphology.

### 6.5 Conclusion

Monitoring acute changes in tumor perfusion and microvascular morphological features may help assess early changes such as dosing windows that are beneficial for follow up chemotherapeutic drug delivery.

### 6.6 References


[1] R. L. Siegel, K. D. Miller, and A. Jemal, "Cancer statistics, 2019," *CA Cancer J Clin*, vol. 69, no. 1, pp. 7–34, 2019.

[2] M. A. Jacobetz, "Hyaluronan impairs vascular function and drug delivery in a mouse model of pancreatic cancer," *Gut*, vol. 62, no. 1, pp. 112–120, 2013.

[3] T. Stylianopoulos, L. L. Munn, and R. K. Jain, "Reengineering the physical microenvironment of tumors to improve drug delivery and efficacy: from mathematical modeling to bench to bedside," *Trends in Cancer*, 2018.

[4] C. B. Thompson *et al.*, "Enzymatic depletion of tumor hyaluronan induces antitumor responses in preclinical animal models," *Molecular Cancer Therapeutics*, 2010.

[5] P. P. Provenzano, C. Cuevas, A. E. Chang, V. K. Goel, D. D. Von Hoff, and S. R. Hingorani, "Enzymatic targeting of the stroma ablates physical barriers to treatment of pancreatic ductal adenocarcinoma," *Cancer Cell*, 2012.

[6] C. J. Whatcott *et al.*, "Desmoplasia in primary tumors and metastatic lesions of pancreatic cancer," *Clinical Cancer Research*, 2015.

[7] A. Kultti, X. Li, P. Jiang, C. B. Thompson, G. I. Frost, and H. M. Shepard, "Therapeutic targeting of hyaluronan in the tumor stroma," *Cancers*, 2012.

[8] D. Nikitovic, M. Tzardi, A. Berdiaki, A. Tsatsakis, and G. N. Tzanakakis, "Cancer Microenvironment and Inflammation: Role of Hyaluronan," *Frontiers in Immunology*, 2015.

[9] R. Saini and K. Hoyt, "Recent developments in dynamic contrast-enhanced ultrasound imaging of tumor angiogenesis," *Imaging in Medicine*, vol. 6, no. 1, pp. 41–52, 2014.

[10] I. Oezdemir, C. Shaw, J. R. Eisenbrey, and K. Hoyt, "Improved quantitative contrast-enhanced ultrasound imaging of hepatocellular carcinoma response to transarterial chemoembolization," *Proc IEEE Int Symp Biomedical Imaging (ISBI)*, pp. 1737–1740, 2019.

[11] F. W. Mauldin, D. Lin, and J. A. Hossack, "The singular value filter: a general filter design strategy for pca-based signal separation in medical ultrasound imaging," *IEEE Transactions on Medical Imaging*, vol. 30, no. 11, pp. 1951–1964, 2011.

[12] D. Ghosh *et al.*, "Monitoring early tumor response to vascular targeted therapy using super-resolution ultrasound imaging," *Proc. IEEE IntUltrason Symp (IUS)*, pp. 1–4, 2017.

[13] D. Ghosh, F. Xiong, S. R. Sirsi, P. W. Shaul, R. F. Mattrey, and K. Hoyt, "Toward optimization of in vivo super-resolution ultrasound imaging using size-selected microbubble contrast agents," *Medical Physics*, vol. 44, no. 12, pp. 6304–6313, 2017.

[14] I. Özdemir and K. Hoyt, "Morphological image processing for multiscale analysis of super-resolution ultrasound images of tissue microvascular networks," *Proc. SPIE Medical Imaging*, vol. 10955, p. 1095505, 2019.

[15] C. Errico *et al.*, "Ultrafast ultrasound localization microscopy for deep super-resolution vascular imaging," *Nature*, 2015.

[16] D. Ghosh *et al.*, "Super-resolution ultrasound imaging of the microvasculature in skeletal muscle: a new tool in diabetes research," *Proc IEEE Ultrason Symp (IUS)*, pp. 1–4, 2017.

[17] K. Tanigaki *et al.*, "Hyposialylated IgG activates endothelial IgG receptor FcγRIIB to promote obesity-induced insulin resistance," *J Clin Invest*, vol. 128, no. 1, pp. 309–322, 2018.

[18] K. Hoyt, A. Sorace, and R. Saini, "Quantitative mapping of tumor vascularity using volumetric contrast enhanced ultrasound," *Investigative Radiology*, vol. 47, no. 3, pp. 167–174, 2012.

[19] K. Hoyt *et al.*, "Determination of breast cancer response to bevacizumab therapy using contrast-enhanced ultrasound and artificial neural networks," *J Ultrasound Med*, vol. 29, no. 4, pp. 577–585, 2010.

[20] K. Hoyt, A. Sorace, and R. Saini, "Volumetric contrast-enhanced ultrasound imaging to assess early response to apoptosis-inducing anti-death receptor 5 antibody therapy in a breast cancer animal model," *J Ultrasound Med*, vol. 31, no. 11, pp. 1759–1766, 2012.

[21] A. F. Frangi, W. J. Niessen, K. L. Vincken, and M. A. Viergever, "Multiscale vessel enhancement filtering," *SpringerLink*, pp. 130–137, 1998.

[22] R. C. Gonzalez and R. E. Woods, *Digital Image Processing*, 4th ed. New York, NY, USA: Pearson, 2018.

[23] K. Hoyt, H. Umphrey, M. Lockhart, M. Robbin, and A. Forero-Torres, "Ultrasound imaging of breast tumor perfusion and neovascular morphology," *Ultrasound in Medicine & Biology*, vol. 41, no. 9, pp. 2292–2302, 2015.

# CHAPTER 7

# THREE-DIMENSIONAL VISUALIZATION AND IMPROVED QUANTIFICATION WITH SUPER-RESOLUTION ULTRASOUND IMAGING – VALIDATION FRAMEWORK FOR ANALYSIS OF MICROVASCULAR MORPHOLOGY USING A CHICKEN EMBRYO MODEL

Authors – İpek Özdemir[1], Kenneth Johnson[1], Shelby Mohr-Allen[1], Kara E. Peak[1], Victor Varner[1], Kenneth Hoyt[1,2]

[1]The Department of Bioengineering, BSB 11
The University of Texas at Dallas
800 West Campbell Road
Richardson, TX 75080-3021

[2]The Department of Radiology
The University of Texas Southwestern Medical Center
1801 Inwood Rd
Dallas, TX 75390

*This is the Accepted Manuscript version of an article accepted for publication in Physics in Med and Biology. IOP Publishing Ltd is not responsible for any errors or omissions in this version of the manuscript or any version derived from it. The Version of Record is available online at 10.1088/1361-6560/abf203.

Author contribution: Ipek Ozdemir (myself) was responsible for the experimental design, the data analysis, and the manuscript preparation presented here.

The purpose of this study was to improve the morphological analysis of microvascular networks depicted in three-dimensional (3D) super-resolution ultrasound (SR-US) images. This was supported by qualitative and quantitative validation by comparison to matched brightfield microscopy and traditional B-mode ultrasound (US) images. Contrast-enhanced US (CEUS) images were collected using a preclinical US scanner (Vevo 3100, FUJIFILM VisualSonics Inc) equipped with an MX250 linear array transducer. Volume data was collected by mechanically scanning the US transducer throughout a tissue volume-of-interest (VOI) in 90 μm step increments. CEUS images were collected at each increment and stored as in-phase/quadrature (IQ) data. All SR-US images were then used to reconstruct a final 3D volume for vessel diameter quantification and for surface rendering. Vessel diameter quantification from the 3D SR-US data exhibited an average error of 6.1 ± 6.0% when compared with matched brightfield microscopy images, whereas measurements from B-mode US images had an average error of 77.1 ± 68.9%. Volume and surface renderings in 3D space enabled qualitative validation and improved visualization of small vessels below the axial resolution of the US system. Overall, 3D SR-US image reconstructions depicted the microvascular network of the developing chicken embryos. Improved visualization of isolated vessels and quantification of microvascular morphology from SR-US images achieved a considerably greater accuracy compared to B-mode US measurements.

## 7.1 Introduction

Traditional ultrasound (US) imaging is not overly sensitive to slow blood flow in small vessels, and this motivated in part the development of microbubble (MB) contrast agents. In response to sufficiently high US pressures, MBs resonant and produce backscattered US signals with a nonlinear component. This nonlinearity helps make them differentiable from the surrounding tissue by an increased MB signal-to-tissue ratio, and allows more accurate visualization of small vessels due to the velocity independent MB properties [1]. MBs have a nontoxic gas core and after intravenous administration, they can be detected with high sensitivity by US imaging. With recent FDA approval of MBs for use in the United States, clinical use is increasing, particularly in patient populations where magnetic resonance imaging (MRI) and computed tomography (CT) contrast agents are contraindicated [2]. Contrast-enhanced US (CEUS) is a noninvasive and nonionizing imaging modality that enables an accurate assessment of blood flow and tissue perfusion [3]. CEUS has therefore been widely used to perform parametric analysis of blood dynamics to assist the diagnosis and treatment monitoring of diseases where tissue perfusion plays an important role [4]–[6].

While blood perfusion is defined by functional properties, CEUS-derived morphological features of microvessels are related to the structural organization of the microvascular networks. The complexity of the underlying microarchitecture can be defined by the number of vessels and bifurcations, geometric measures of mean vessel diameter and tortuosity, and microvessel density (MVD) as a measure of compactness. These morphological features are crucial because it is known that some more severe diseases, such as diabetes, begin developing impaired functionality at the capillary level [7], [8]. Other severe diseases, such as cancer, can also trigger neovascularization

as the disease progresses. The addition of structural information to the functional analysis of tissue microvascular networks may help improve disease management, particularly in the oncological setting [5]. Morphological features of microvascular networks can be clinically informative. For example, complex networks may assist in guiding repeat therapies while simpler networks may suggest a successful therapy response [9]. CEUS-derived quantification of microvascular morphology can expand our understanding of the chaotic development of pathologic angiogenesis by which tumors develop their own blood supply to receive nutrients and oxygen from the host vascular system [10].

Despite the advantages of CEUS, the spatial resolution of any US imaging system is fundamentally limited by diffraction to length scales of approximately half the wavelength of the transmitted beam. The recently introduced super-resolution US (SR-US) imaging technique is based on precise MB localization and has been shown to achieve a remarkably high spatial resolution beyond the diffraction limit [11]–[13]. With the use of SR-US imaging, it is now possible to provide functional and structural quantification of microvascular networks [14]. SR-US imaging offers the promise of more accurate identification of microvascular morphology for the vessels below 50 μm in diameter [15], [16]. For the most reliable morphological analysis derived from US studies, volumetric SR-US imaging is critical because microvascular networks inherently exist in three-dimensional (3D) space [17]–[20]. While several important features of microvascular networks can be quantified from 2D and 3D SR-US images, detailed validation of these measurements is challenging.

Most CEUS imaging studies to date have relied on use of vascular flow phantoms for in vitro validation [21], [22] and histological biomarkers of microvessel density or prior knowledge about

healthy versus tumor tissue for in vivo validation [23]–[26]. Recently, a CEUS study using a chicken embryo model demonstrated that image-derived morphology metrics (e.g., intervessel distance and microvascular tortuosity) were correlated to local tissue hypoxia [27]. Herein, we present an automated approach for 3D SR-US imaging and morphological analysis of microvascular networks. SR-US image-derived vessel diameters were extracted using an automated thinning algorithm. Accuracy was validated with matched brightfield microscopy images of vessel structures from the same chicken embryo model. The primary novelty of this research lays in improved visualization and validation of an approach to measure microvascular morphology features using 3D SR-US imaging.

## 7.2 Materials and Methods

### 7.2.1 Phantom Materials

A tubing material of regenerated cellulose (Dow Corning Corp, Midland, MI) with a 200 μm internal lumen diameter was immersed and secured inside a water filled container. Two different phantom setups were used for US system configuration testing and custom software calibration. In the first experiment, a single straight tube was used to circulate MBs, whereas in the second experiment, two crossing straight tubes were US imaged. With these flow phantoms, scale parameters for a vessel enhancement filter, were optimized using several different US image and focal depths.

### 7.2.2 Chicken Embryo Model

Fertilized white leghorn chicken eggs were obtained from a commercial vendor (Texas A&M University, College Station, TX) and stored in a forced-draft incubator (GQF Manufacturing Company Inc, Savannah, GA) maintained at 37°C and 60% humidity until Hamburger-Hamilton stage 18 (HH18, 3 days). Eggs were then transferred to an open 3D printed polymer boat with a window created on one of the sides by gluing a thin polyester film (McMaster-Carr, Elmhurst, IL). A total of eight chicken embryos were used for this study.

### 7.2.3 Ultrasound Imaging Protocol

CEUS imaging was performed using a preclinical US scanner (Vevo 3100, FUJIFILM VisualSonics Inc, Toronto, Canada) equipped with an MX250 linear array transducer. This transducer has a center frequency of 21 MHz (axial resolution ≈ 75 μm) and bandwidth from 15 to 30 MHz. A custom MB contrast agent was formulated using established methods [28]. For the phantom studies, 2 μL of MBs were diluted in 100 mL of degassed water and perfused through the cellulose tubes using a syringe pump at a rate of 2 mm/min similar to the blood flow of a chicken embryo [27], [29]. For the chicken embryo studies, 5 μL of the MB solution was loaded into a pulled glass pipette. Physical measurement of MB size and concentration found a mean diameter of $2.6 \pm 1.3$ μm and $1.4 \times 10^{10}$ MBs/mL, respectively. While visualizing the embryo with a stereomicroscope (Carl Zeiss Microscopy, White Plains, NY) connected to a digital camera, MBs were slowly introduced into the embryo's vitelline network by microinjection for a duration of about 5 sec. Both phantoms and chicken embryos were US imaged as the transducer was mechanically scanned over a volume-of-interest (VOI) in 90 μm step increments using the Vevo

Imaging Station (FUJIFILM VisualSonics Inc). Note that MBs circulated throughout the microvascular network of the chicken embryo until the heart stopped, which could take up to 30 min according to our observations. The volume of the circulating blood in the chick embryo on day 4 was estimated to be 44 ± 12 $mm^3$ [30].As detailed in Figure 7.1, a series of CEUS images were acquired at each increment and stored as in-phase/quadrature (IQ) data ($N = 2000$). All scan parameters, such as time gain compensation (TGC) and system power (1%) were saved as a preset and fixed for all experimental studies. Volume US datasets from eight different embryos were saved for offline processing and analysis.

### 7.2.4 Ultrasound Image Processing

All image processing, quantification, and visualization was performed using custom MATLAB software (MathWorks Inc, Natick, MA). For each CEUS dataset, a singular value filter (SVF) was first applied to the IQ frames [31]. SVF separates the stationary speckle signal (tissue) from the nonlinear MB signal of interest. After the removal of tissue signal, MBs were detected by an 8-connected component analysis. A single MB was represented as a connected component. The

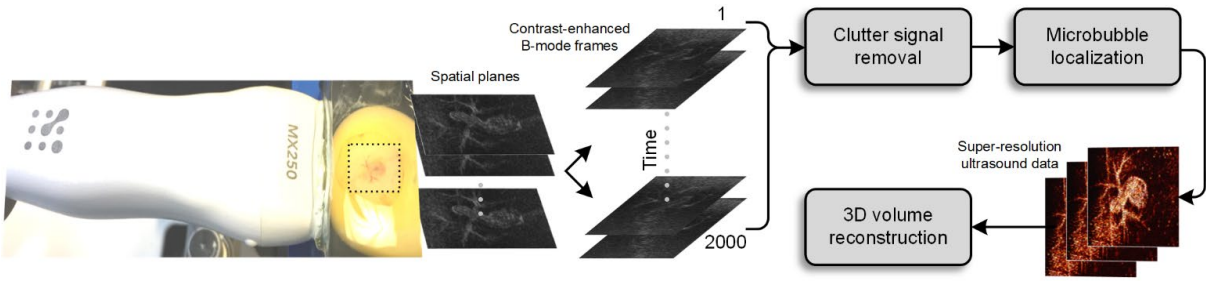


Figure 7.1. Diagram of the experimental design and the data processing strategy used for acquiring a sequence of contrast-enhanced ultrasound (CEUS) images and subsequent generation of the three-dimensional (3D) super-resolution ultrasound (SR-US) maps of microvascular structures. Two thousand frames of ultrasound (US) data was collected for each cross-section as the transducer was mechanically scanned over a defined volume-of-interest (VOI).

centroid of each connected component was then determined and mapped as described previously [8]. The centroid of each connected component was then determined and mapped. At any tissue cross-section, a sequence of 2000 CEUS images were collected and a SR-US image was created by counting the number of MBs found at each pixel location. Lastly, SR-US data from each spatial position were resampled to reconstruct an isotropic 3D SR-US volume.

A multiscale vessel enhancement filter was applied to the 3D SR-US volume to further enhance microvascular structures [32], [33]. Note this method has been widely used in CT and MRI angiography to improve diagnostic quality. Vessels were assumed to be tubular structures having a Gaussian profile and detected using the second derivative of Gaussian kernels of a specific dispersion. This parameter helps to detect a range of large and small vessels with wider and thinner Gaussian kernels, respectively. Next, we introduce a vesselness function $V_o(\gamma)$ defined as:

$$V_o(\gamma) = \begin{cases} 0 & \text{if } \lambda_2 > 0 \text{ or } \lambda_3 > 0 \\ \left(1 - e^{-\left(\frac{R_A{}^2}{2a^2}\right)}\right) e^{-\left(\frac{R_B{}^2}{2\beta^2}\right)} \left(1 - e^{-\left(\frac{S^2}{2c^2}\right)}\right) & \text{elsewise} \end{cases} \tag{7.1}$$

where $\lambda_{1,2,3}$ are the eigen values from the Hessian matrix, and:

$$R_B = \frac{|\lambda_1|}{\sqrt{|\lambda_2|\lambda_3|}}, R_A = \frac{|\lambda_2|}{|\lambda_3|}, \qquad S = \sqrt{\sum_{j=1}^{3} \lambda_j^2}. \tag{7.2}$$

Here, $V_o(\gamma)$ results in greater values for tubular structures in 3D space and consequently, background noise is suppressed, i.e., nontubular structures. Previous experience has revealed that enhancement of the vascular structures is helpful to improve individual vessel segmentation before performing any diameter measurements. The vesselness function is needed to enhance

connectivity between pixels belonging to the same vessel segment. This function improves the process in two main ways. First, it suppresses background structures that are not necessarily tubular. And second, it enhances the tubular structures at different scales so we retain smaller vessels in the image as connected components during binarization. This is requisite for creating an accurate 3D centerline of the vessel segment, which relies on pixel connectivity of binary images. It was not possible to create accurate 3D centerlines without applying this multiscale vessel enhancement due to the presence of non-connected vessel segment components. Segmentation is performed using an adaptive thresholding algorithm [34]. This method finds a local threshold to create a binary volume that represents vessels as foreground voxels. This binary volume was then used for morphological image processing.

3D SR-US image-based morphological analysis was automated such that centerlines of the vasculature from the binary volume were extracted and a connected component analysis was performed. A 3D parallel medial-axis-thinning algorithm was then used for centerline extraction [35]. This method uses a morphological thinning operator that removes the voxels starting from the vessel border until it represents each vessel segment by a voxel-thick line (centerline) in volume space [36]. Also called a skeleton, the centerlines have the same topology as the original vasculature. Vessel groups containing different vascular branches are defined by 26-voxel connectivity, where connected voxels are defined as two adjacent voxels sharing their faces, edges, or corners. Following the thinning process, a standard pruning algorithm is used to remove all branches shorter than 10 voxels in length [37]. Branching points are also removed to create isolated vessel segments and the shortest vessel segments are identified as two-voxel connected centerlines. Vessel diameter (VD) for each point on the centerline were estimated using another morphological

operator called the distance transform. The Euclidean distance of each centerline point to the nearest point on the vessel border is computed and multiplied by the voxel size to obtain the VDs for the 3D SR-US data. Each embryo needed up to 30 min of processing time to create the final skeleton using an Alien Aurora desktop computer (Dell Inc, Round Rock, Texas). Parallel processing was performed to reduce computation time for creation of the SR-US images. Skeletonized microvasculature and diameter measurements at each centerline point were used for the surface reconstruction and for the extraction of morphological features, namely, number of bifurcations (NB), number of vessels (NV), mean vessel length (VL), and mean vessel tortuosity (VT). VL is computed as the total vessel arc length. VT is the ratio of the VL to the distance between vessel end points. The VDs from microscopy and B-mode US images were measured using the reference method full-width-half-maximum (FWHM) for randomly selected individual vessels within the VOI. A mean FWHM from a single vessel segment is computed as the average of three randomly selected locations on the same vessel segment. Maximum intensity projection (MIP) images are created using the maximum values of the image stack. A control point registration method from the MATLAB Image Processing Toolbox (MathWorks Inc) was used to apply affine realignment between the three imaging modalities. Control points were selected on the static image (microscopy) and moving image (B-mode US or SR-US MIP) and the spatial transformation was performed to locate the same vessels on all three different imaging modalities.

Finally, surfaces of the individual vessels were reconstructed based on the centerline and diameter values at each centerline point to improve visualization [38]. The final surfaces of isolated vessels were calculated as follows. First, the gradient vector was calculated to show the proper orientation of the microvasculature at each centerline point. A plane orthogonal to the gradient

vector was established to determine surface reference points. Using sequential orthogonal planes, all surface reference points are connected to create right triangles that build the surface of the microvasculature. Visualization improvement was defined by 3D SR-US volume and surface renderings generated from microvascular centerlines to provide the shape information of a specific vessel in volume space, and by assessing the ability to detect vessels with diameters less than 75 μm. Both types of improvements were validated using co-registered brightfield microscopy images that were used to identify the matching vessels by qualitative assessment.

### 7.2.5 Performance Metrics

The VD parameter was used to quantitatively compare FWHM microscopy, B-mode US, and thinning-based 3D SR-US-derived image diameter measurements. Unpaired *t*-tests between microscopy and 3D SR-US measurements, and between microscopy and B-mode US diameter measurements, were performed to test for differences in VD. Further, average diameter values for individual vessel segments were used to assess the accuracy in VD between the microscopy images and SR-US or B-mode US images using the following metrics:

$$\text{Absolute Error } (\mu\text{m}) \; \Delta = \left| \text{VD}_{\text{SR-US}} - \text{VD}_{\text{Microscopy}} \right| \tag{7.3}$$

and

$$\text{Percent Error } (\%) = \frac{\Delta}{\text{VD}_{\text{Microscopy}}} \times 100. \tag{7.4}$$

From equation (3), the root-mean-square error (RMSE) for VD measures is computed between those derived from microscopy and each of 3D SR-US images as follows:

$$\mathrm{RMSE} = \sqrt{\frac{\sum_{i=1}^{N}(\mathrm{VD}_{\mathrm{SR-US(i)}} - \mathrm{VD}_{\mathrm{Microscopy(i)}})^2}{K}} \tag{7.5}$$

where i is the individual diameter measurement index and K is the number of vessel segments that were analyzed. Note that $\mathrm{VD}_{\mathrm{SR-US}}$ was replaced with $\mathrm{VD}_{\mathrm{B-mode}}$ for the B-mode US measurements..

### 7.3 Results

A set of 3D SR-US images were acquired from a slowly perfused flow phantom (internal vessel diameter of 200 μm) and volume reconstructions are presented in Figure 7.2. Representing a simple vessel structure, the phantom containing a single straight tube was successfully visualized using a MIP from the SR-US data and in 3D space. The skeletonized image illustrates a simplified topology of this single vessel. Using data acquired from the flow phantom with crossing tubes, scaling parameter optimization of the vessel enhancement filter resulted in successful visualization of the 3D SR-US data and the derived topology of the vascular network. As further summarized in Figure 7.2, mean internal vessel diameter measurements were found to be 204 ± 19 μm and 206 ± 12 μm for the straight and crossing tube phantoms, respectively. The corresponding vessel diameter measurements from the co-registered B-mode US images were 242 ± 92 μm and 188 ± 59 μm, respectively.

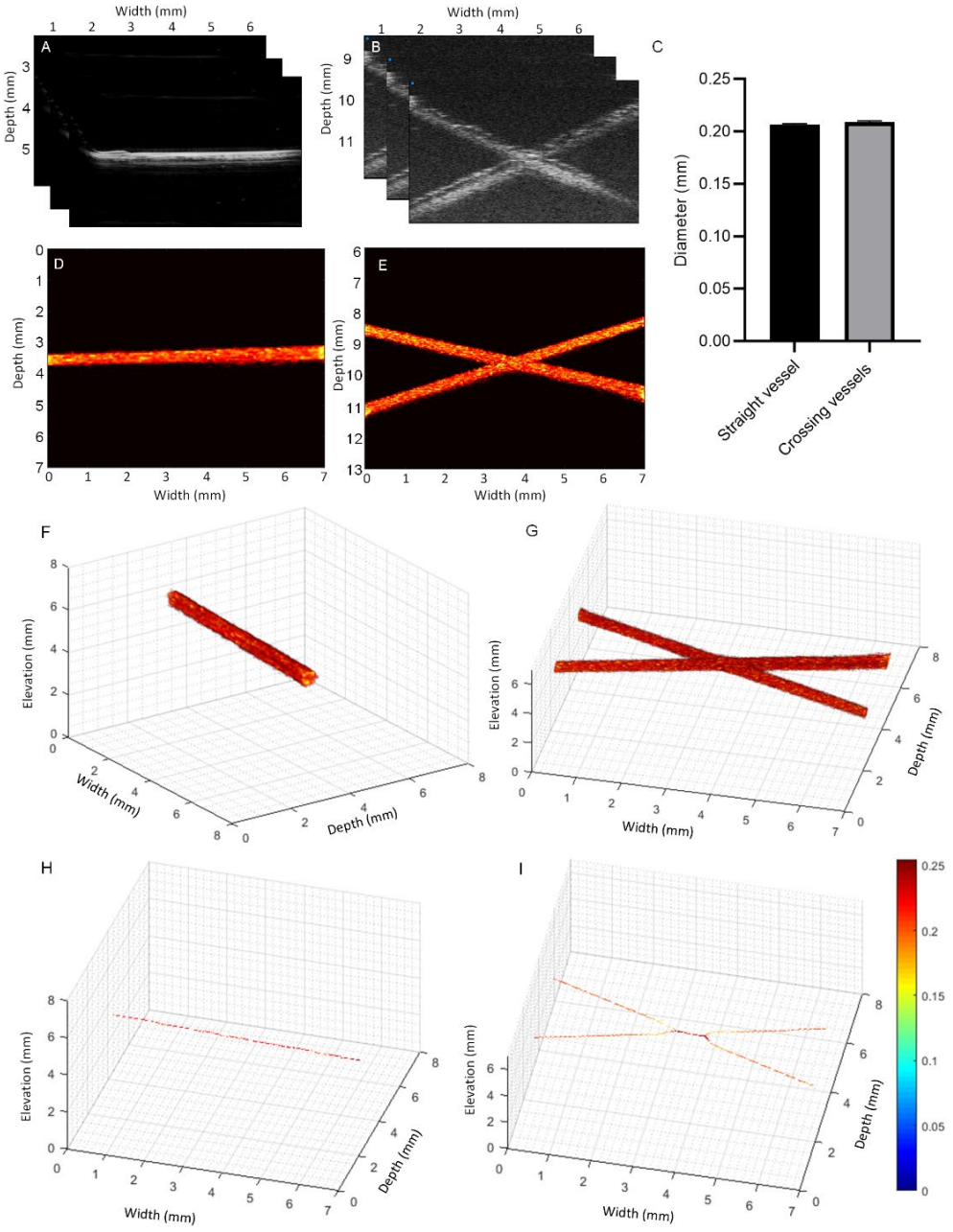


Figure 7.2. Representative CEUS images from two phantoms containing either a (A) single straight tube or (B) two crossing tubes, all with an internal lumen diameter of 200 µm. After acquisition of the CEUS data, (D, E) SR-US maps were created and displayed as 2-dimensional (2D) projections. Matched (F, G) 3D SR-US image reconstructions are also shown in volume space. After binary image skeletonization as needed for morphological analysis of microvascular features, (H, I) centerline segments were colorized to reflect local vessel diameter measurements. (C) Tube diameter measurements (mean ± standard deviation) were found to be 204 ± 19 µm and 206 ± 12 µm for the straight and crossing tubes, respectively.

Phantom studies demonstrated that 3D SR-US morphological analysis with multiscale vessel enhancement and surface reconstruction qualitatively improved the visualization of microvascular structures. A validation study using developing chicken embryos then showed promising results when compared to co-registered brightfield microscopy images. Representative B-mode US and SR-US images from this model system are presented in Figure 7.3, which allows a qualitative

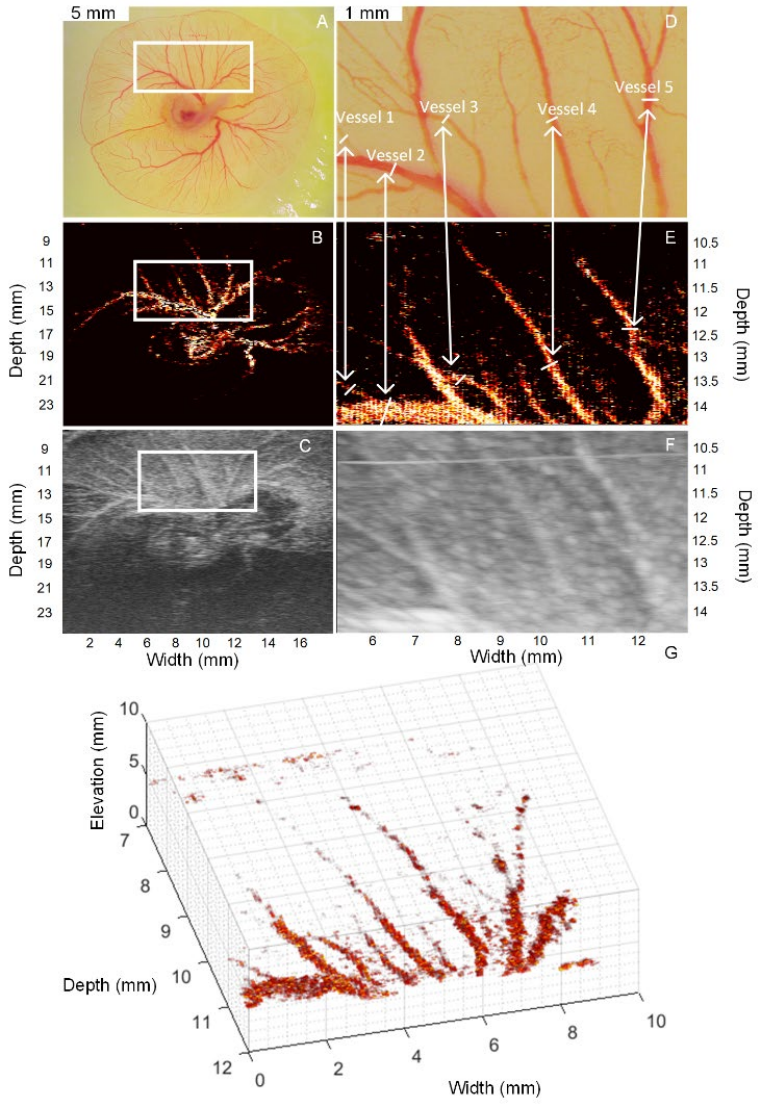


Figure 7.3. Co-registered (A) brightfield microscopy, (B) SR-US, and (C) B-mode US images for a defined area (white box), which has been enlarged in (D, E, F), respectively. Panel (G) contains the 3D SR-US volume reconstruction of the microvascular network from a developing chicken embryo.

comparison between the three different imaging methods for a VOI containing vessels with several varying morphological characteristics. A 3D reconstruction of the SR-US volume data provides a more comprehensive view of the microvascular network in the developing chicken embryo although some structures are disconnected due to the limited number of US frames (i.e., sparse dataset). The spatial gaps between the detected MBs were partially filled after the use of a multiscale vessel enhancement algorithm.

As detailed in Figure 7.4, the SR-US image processing approach removes the unwanted stationary tissue signal while leaving the MB signal of interest for further analysis. Further highlighted, the microvascular network in the B-mode US image is obscured and vessels within are not clearly distinguishable due in part to insufficient spatial resolution and reverberation artifacts. However, the SR-US MIP image in Figure 7.4 clearly depicts the microvasculature that was successfully perfused with MBs. When considering a specific VOI, the smallest vessel resolved was approximately 30 μm in diameter as estimated from the FWHM profiles shown. Here, vessel diameter was accurately estimated by the 3D SR-US-derived MIP image when compared to the reference standard brightfield microscopy image. This specific vessel was isolated from the microvascular network and its surface was reconstructed for a qualitative comparison to the B-mode US image embedded in the width-depth plane. This example illustrates that the spatial resolution of the B-mode US image does not allow visualization of vessels that have a diameter below the US system resolution (about 75 μm) while 3D SR-US MIP images can accurately delineate vessels with diameters as small as 30 μm. The ability to reconstruct the surface from the 3D SR-US data using the simplified network topology, together with the vessel diameters, enables

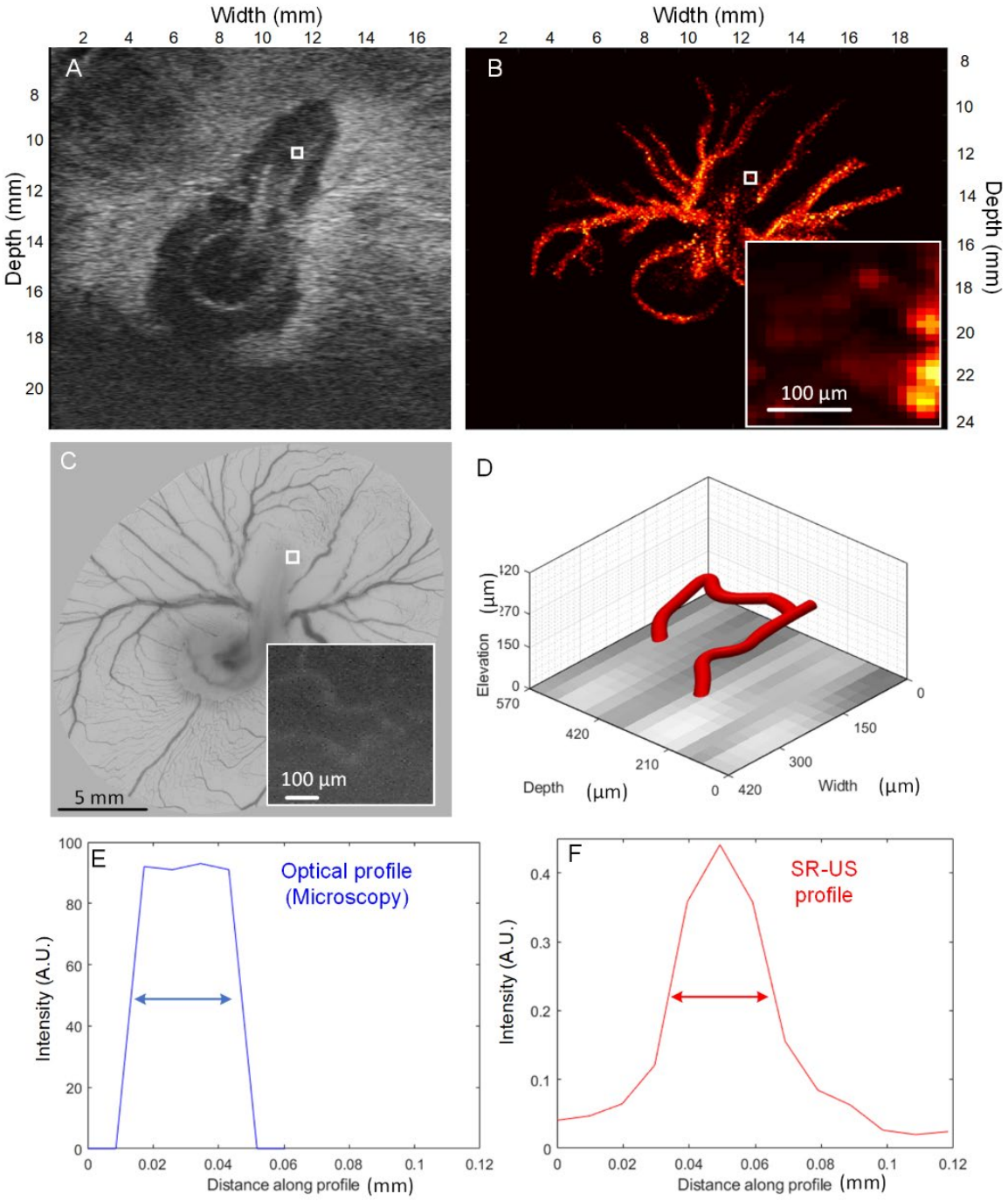


Figure 7.4. Comparison of co-registered (A) B-mode US (A), (B) SR-US, and (C) brightfield microscopy images of a developing chicken embryo. Vessel cross-sectional line plots in (E) and (F) were taken from within the white box and estimated to be approximately 30 µm and below the axial resolution of the US system used for data acquisition. (D) Zoomed-in area from the B-mode US image is shown into the width-depth plane (grayscale map) with the matched 3D SR-US surface reconstruction provided for qualitative comparison.

a more complete morphological analysis that can provide information about the complexity, geometric diversity, and the compactness of the underlying microvascular network.

A collection of vessels segments from a brightfield microscopy image and 3D SR-US data are shown in Figure 7.5. The mean diameter of the sample vessels vary and range from 30 to 350 µm. As a result of the thinning algorithm, representative samples of isolated vessel topologies containing the morphological information is depicted in volume space. According to the automatically extracted tortuosity measurements, for example, vessel 3 is the most tortuous vessel (14.0) and vessels 1, 5, and 4, have decreasing tortuosity contours of 2.7, 1.9, and 1.5, respectively). Vessel 2 is the simplest vessel with the least tortuosity (0.5), which implies it is a nearly straight segment. The centerlines of different microvascular segments from a developing chicken embryo are presented in Figure 7.6, and allow for an analysis using morphological features from the network topology. Qualitatively, B-mode US images are first improved by the SR-US MIP, which enables visualization of the microvascularity.

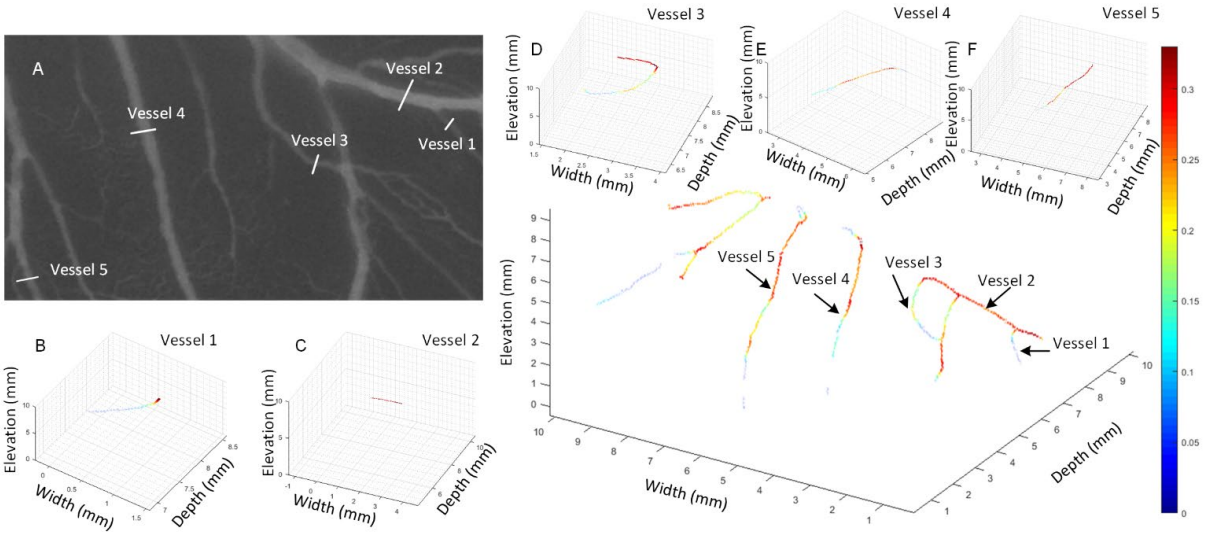


Figure 7.5. Individual vessels from a (A) brightfield microscopy image and (B - F) 3D SR-US images that were used to make select microvascular morphology measurements. Color bar represents vessel diameter.

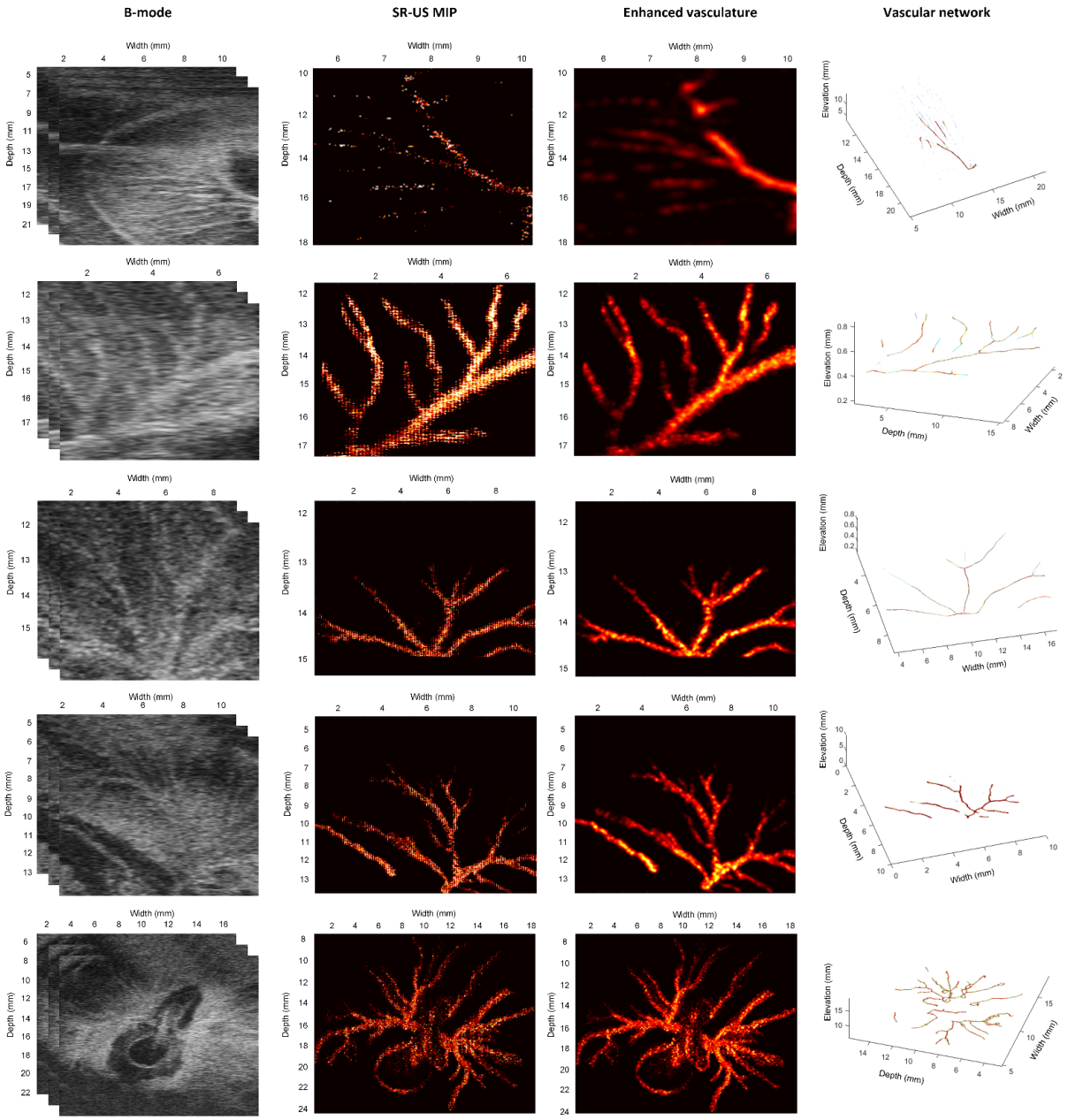


Figure 7.6. CEUS images of five different developing chicken embryos whereby each row shows the intermediate steps of the image processing pipeline for each target. Visual inspection of the B-mode US images (column one) compared to the SR-US MIP (column two), spatially filtered SR-US MIP (column three), and extracted 3D network topologies (column four), reveals a clear representation of tissue microvascular networks using SR-US imaging.

Further qualitative improvement is achieved after using the multiscale vessel enhancement filter, which provides a more connected microvascular structure in volume space after closer inspection. Improved connectivity resulted in more accurate segmentation and thinning for mapping the microvascular topology in a clear and simplified form of vessel centerlines. These qualitative results are also supported by the quantitative results summarized in Figure 7.7. Diameter measurements from 15 individual vessel segments extracted from different chicken embryo datasets show good agreement between the brightfield microscopy and 3D SR-US images. On the other hand, B-mode US image measurements exhibited large deviations from the true values (i.e., microscopy quantification). Physical limitations of the US system prevent accurate B-mode US measurement of vessels with diameters below the resolution threshold, which is about 75 µm for the transducer used. On average, 3D SR-US had an average vessel diameter measurement error of 6.1%, including small vessels, while B-mode US-derived results exhibited an average error of 77.1% for vessels greater than this 75 µm diameter threshold, Table 7.1. The

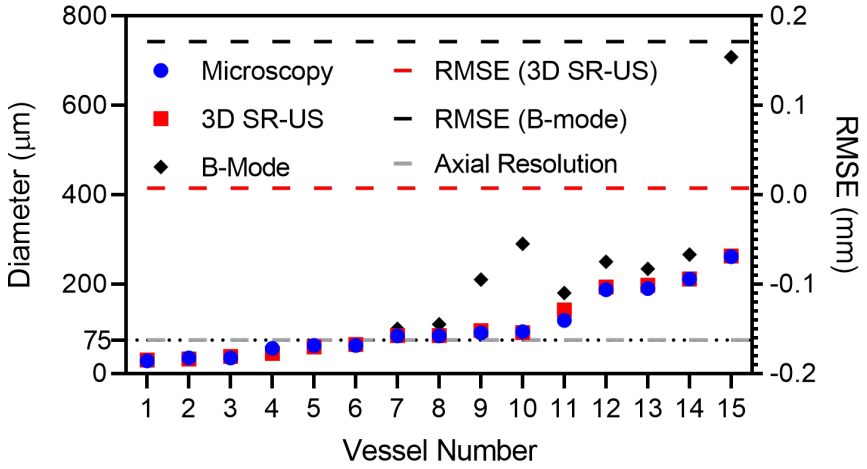


Figure 7.7. Comparison of vessel diameter validations using brightfield microscopy, B-mode US, and 3D SR-US images. Quantification from the 3D SR-US image reconstructions are in good agreement with the microscopic measurements. Vessels are ordered by diameter values and it was not possible to measure vessels from the B-mode US images that were smaller than the spatial resolution limits US system used for image acquisition.

Table 7.1. Quantification error of vessel diameters when comparing B-mode ultrasound (US) and super-resolution US (SR-US) after comparison to co-registered microscopy-based (reference) measurements.

| Imaging Technique | Absolute Error (μm) | Percent Error (%) | *p*-value |
|---|---|---|---|
| B-mode US | 113.9 | 77.1 | 0.007 |
| 3D SR-US | 4.8 | 6.1 | 0.9 |

absolute error between the 3D SR-US and microscopy image measurements was 4.8 μm for all 15 vessels studied and only 4.2 μm for the smaller vessels (those less than 75 μm in diameter). The RMSE between the 3D SR-US and microscopy measures was 7.4 μm, while the RMSE between the B-mode US and microscopy was found to be considerably higher and 171.6 μm. B-mode US image-derived estimations were found to be significantly different than those from the microscopy measurements ($p < 0.01$), which was no true for the 3D SR-US estimates ($p = 0.93$) and supports the previously observed qualitative improvements.

### 7.4 Discussion

It was shown that 3D SR-US image reconstructions could be obtained from CEUS data acquired at multiple tissue cross-sections on a preclinical US system without any hardware modifications. Vessel diameters were quantified using co-registered B-mode US, SR-US, and brightfield microscopy images. An automated 3D SR-US morphological analysis was performed and VD measurements demonstrated greater accuracy when compared to B-mode US image-derived values and use of microscopy image measures as the reference standard. This work helps validate the accuracy of 3D SR-US imaging and quantification of microvascular morphology features.

Structural properties of vascular networks depicted in preclinical and clinical CEUS images have previously been investigated using a single cross-sectional plane [5], [39]. While these studies demonstrated the potential of structural analysis from CEUS images, use of a single plane is a limitation and it was suggested that a 3D CEUS imaging approach could better capture the heterogeneous nature of tumor vascularization in volume space [40], [41] and allow isotropic measurements [42]. This current study provided a 3D morphological analysis of CEUS images and the use of super-resolution techniques provided a more precise and accurate depiction of morphometries extracted from the microvascular network of developing chicken embryos. Further, results were compared with morphological measurements from traditional B-mode US images to highlight the improvements.

Other studies have performed CEUS-derived morphological analysis using US systems with modified hardware components [19], [24], [26], [43]. Although these studies validated MVD by histological analysis and found correlations between the CEUS-derived morphological features and tumor growth, a detailed validation of the underlying geometrical measurements was missing. Our study demonstrated a reliable multimodal imaging validation of VD using an *in vivo* embryo model and brightfield microscopy. This current work also showed that 3D SR-US image measurements are highly accurate compared to those derived using traditional B-mode US. With the 3D surface reconstruction of isolated smaller vessels, it is now possible to identify the same vessels for longitudinal studies and to track quantifiable morphological changes to assess disease progression, which typically manifests at the capillary level.

Chicken embryo models have been investigated in a non CEUS imaging study [44]. Compared to CEUS, contrast-free US is known to have limited sensitivity to slow blood flow. A recent CEUS

study using chicken embryo models have shown that image-derived morphology metrics (e.g., intervessel distance and vascular tortuosity) were correlated to tissue hypoxia [27]. This particular study compared manually selected vessel profiles from brightfield microscopy to SR-US images acquired with a research US system, where morphological metrics were validated with histological analysis. Our approach in the current study is different from this work in several aspects. First, we used a preclinical US system with a smaller step size to collect the 3D CEUS data. Second, our automated 3D SR-US software measures the vessel centerlines based on a thinning algorithm. Third, and most importantly, we compare the validated VD measurements with B-mode US images and demonstrate improved accuracy and visualization using 3D SR-US imaging.

Extracting vascular morphometric maps directly from B-mode US images can lead to systematic biases that result in erroneous measurements, particularly from smaller vessels. The effect of such a bias is reduced with use of 3D SR-US data for two principal reasons. First, the higher spatial resolution allows more accurate delineation of microvascular details. Second, 3D reconstructions of microvascular shape improves the geometric accuracy because the microvasculature inherently exists in volume space. The coherent geometry of the microvascular structures from a VOI can be better visualized and measured more accurately (10-fold improvement) based on the percent error in VD using the proposed method. Visualization of smaller blood vessels (i.e., those with diameters below the diffraction limit) is only possible with SR-US data as these structures are not readily visible in B-mode US images.

For some longitudinal studies, it is assumed that various types of artifacts are included in baseline and follow-up measurements, and these would contribute equally to erroneous results. It would therefore be beneficial to observe relative changes to capture a disease treatment response

or to observe progressive tumor growth. Nevertheless, it is important to characterize the tumor microvascularity as accurately as possible using a noninvasive imaging method so as to appropriately plan a drug delivery and treatment study [9]. Being able to observe any sub-optimal vascularization and reduced tumor blood flow could guide the selection of alternative treatment strategies. For example, if the microvasculature has collapsed due to high intratumoral pressures, the angiogenic network could be normalized first [45], [46]. In this case, as a pre-therapeutic necessity, the vessels needed to be dilated to a certain diameter range to deliver any systemic anticancer drug efficiently. The software approach presented here is also appropriate for these types of drug delivery studies.

Compared to traditional B-mode US image analysis, 3D SR-US morphological analysis offers the prospect of measurement repeatability. Instead of single imaging plane, a volumetric representation can assist in repeating measurements for the same subject, which is important for monitoring drug response or status of disease progression. A reproducible quantitative morphometric analysis increases the reliability of the metrics, and this may improve drawing clinically-relevant correlations to the measured quantities. 3D isolation of individual vessels allows for more accurate monitoring of vessel shape alterations. In 2D, the binarization process creates many overlapping vessels, and this may cause the centerline detection to fail. Due to the heterogeneous nature of the tumor burden, a noninvasive 3D morphological analysis is the preferred method.

A potential limitation of the method presented herein is related to motion artifacts. When applying the proposed approach to complex microvascular structures and in the presence of tissue displacement, this method would presumably necessitate a fine motion correction strategy [47],

which was not necessary in the present study due to negligible cardiac motion of the chicken embryo. All imaging was performed in live chicken embryos and it was noted that the heartbeat did tend to slow after introduction of the MB contrast agent. Subsequently, microvascular displacement was negligible relative to MB motion. An optimizer to correct any CEUS frame motion might have revealed any otherwise negligible microvascular pulsations. A multi-stage motion correction strategy for SR-US [48], [49] can be performed and will be needed with use of more complex *in vivo* models. Any of these respiratory, cardiac, or transducer motions would have a more profound impact on the skeletonization and thinning processing when devoid of a motion correction strategy. In future studies, we will explore use of motion correction before thinning and any subsequent microvascular measurements. The limitation of elevational plane thickness is minimized by having a smaller step size (90 μm) than the slice thickness (403 μm). This allowed overlap between sequential slices and a 90 μm window for updated and differentiable information between two slices.

As MB size is known to impact SR-US image quality, use of a larger MB contrast agent [50] and more sensitive US imaging strategy [51] may further help improve quantification of the finer microvascular detail in the developing chicken embryo and other tissue environments. Recently, a simultaneous comparison between different transmit pulsing strategies revealed that a combined CEUS approach can improve SR-US imaging by increasing the number of MBs detected during a given acquisition time period [52]. It was also shown that MB tracking can help improve delineation of smaller vessels [53]. To use our quantification and visualization approach for SR-US imaging of human subjects, the image processing will need to address additional considerations, including the impact of US attenuation and the ability to detect MBs at tissue depth,

acceptable motion correction accuracy, etc. Once adequate SR-US images are produced, our quantification and visualization approach could be applied without any known limitations. Although some promising results have shown that SR-US image can be formed using clinical data [54], 3D CEUS image acquisition needs to be assessed in a controlled clinical setup due to above noted (and other) potential concerns.

### 7.5 Conclusion

The work presented details a novel framework for image processing and validation of 3D SR-US. Morphological analysis of microvascular networks was validated using co-registered brightfield microscopy images. Microvessel segments with a diameter (size) below the B-mode US image resolution were visible in volume and surface reconstructions of the 3D SR-US image data.

### 7.6 References


[1] M. A. Averkiou, M. F. Bruce, J. E. Powers, P. S. Sheeran, and P. N. Burns, "Imaging methods for ultrasound contrast agents," *Ultrasound Med Biol*, vol. 46, no. 3, pp. 498–517, 2020.

[2] T. D. Hull, A. Agarwal, and K. Hoyt, "New ultrasound techniques promise further advances in AKI and CKD," *JASN*, vol. 28, no. 12, pp. 3452–3460, 2017.

[3] R. Saini and K. Hoyt, "Recent developments in dynamic contrast-enhanced ultrasound imaging of tumor angiogenesis," *Imaging Med*, vol. 6, no. 1, pp. 41–52, 2014.

[4] L. Basavarajappa *et al.*, "Multiparametric ultrasound imaging for the assessment of normal versus steatotic livers," *Sci Rep*, vol. 11, no. 1, p. 2655, 2021.

[5] K. Hoyt, H. Umphrey, M. Lockhart, M. Robbin, and A. Forero-Torres, "Ultrasound imaging of breast tumor perfusion and neovascular morphology," *Ultrasound Med Biol*, vol. 41, no. 9, pp. 2292–2302, 2015.

[6] D. Ghosh *et al.*, "Monitoring early tumor response to vascular targeted therapy using super-resolution ultrasound imaging," *Proc IEEE Ultrason Symp*, pp. 1–4, 2017.

[7] K. Tanigaki *et al.*, "Hyposialylated IgG activates endothelial IgG receptor FcγRIIB to promote obesity-induced insulin resistance," *J Clin Invest*, vol. 128, no. 1, pp. 309–322, 2018.

[8] D. Ghosh *et al.*, "Super-resolution ultrasound imaging of skeletal muscle microvascular dysfunction in an animal model of type 2 diabetes," *J Ultrasound Med*, vol. 38, no. 5, pp. 2589–2599, 2019.

[9] I. Oezdemir, C. E. Wessner, C. Shaw, J. R. Eisenbrey, and K. Hoyt, "Tumor vascular networks depicted in contrast-enhanced ultrasound images as a predictor for transarterial chemoembolization treatment response," *Ultrasound Med Biol*, vol. 46, no. 9, pp. 2276–2286, 2020.

[10] J. Folkman, "How is blood vessel growth regulated in normal and neoplastic tissue?," *Cancer Res*, vol. 76, no. 10, pp. 2854–2856, 2016.

[11] K. Christensen-Jeffries, R. J. Browning, M.-X. Tang, C. Dunsby, and R. J. Eckersley, "In vivo acoustic super-resolution and super-resolved velocity mapping using microbubbles," *IEEE Trans Med Imaging*, vol. 34, no. 2, pp. 433–440, 2015.

[12] M. A. O'Reilly and K. Hynynen, "A super-resolution ultrasound method for brain vascular mapping," *Med Phys*, vol. 40, no. 11, p. 110701, 2013.

[13] C. Errico *et al.*, "Ultrafast ultrasound localization microscopy for deep super-resolution vascular imaging," *Nature*, vol. 527, no. 7579, p. 499, 2015.

[14] I. Oezdemir *et al.*, "Multiscale and morphological analysis of microvascular patterns depicted in contrast-enhanced ultrasound images," *J Med Imaging*, vol. 7, no. 3, p. 034001, 2020.

[15] K. Christensen-Jeffries *et al.*, "Super-resolution ultrasound imaging," *Ultrasound Med Biol*, vol. 46, no. 4, pp. 865–891, 2020.

[16] K. G. Brown, D. Ghosh, and K. Hoyt, "Deep learning of spatiotemporal filtering for fast super-resolution ultrasound imaging," *IEEE Trans Ultrason Ferroelectr Freq Control*, vol. 67, no. 9, pp. 1820–1829, 2020.

[17] S. Harput *et al.*, "3-D super-resolution ultrasound imaging with a 2-D sparse array," *IEEE Trans Ultrason Ferroelectr Freq Control*, vol. 67, no. 2, pp. 269–277, 2020.

[18] B. Heiles *et al.*, "Ultrafast 3D ultrasound localization microscopy using a 32 x 32 matrix array," *IEEE Trans Med Imag*, vol. 38, no. 9, pp. 2005–2015, 2019.

[19] F. Lin, S. E. Shelton, D. Espíndola, J. D. Rojas, G. Pinton, and P. A. Dayton, "3-D ultrasound localization microscopy for identifying microvascular morphology features of tumor angiogenesis at a resolution beyond the diffraction limit of conventional ultrasound," *Theranostics*, vol. 7, no. 1, pp. 196–204, 2017.

[20] J. Zhu *et al.*, "3D super-resolution ultrasound imaging of rabbit lymph node vasculature in vivo by using microbubbles," *Radiology*, vol. 291, no. 3, pp. 642–650, 2019.

[21] O. M. Viessmann, R. J. Eckersley, K. Christensen-Jeffries, M. X. Tang, and C. Dunsby, "Acoustic super-resolution with ultrasound and microbubbles," *Phys Med Biol*, vol. 58, no. 18, pp. 6447–6458, 2013.

[22] D. Espíndola, R. M. DeRuiter, F. Santibanez, P. A. Dayton, and G. Pinton, "Quantitative sub-resolution blood velocity estimation using ultrasound localization microscopy ex-vivo and in-vivo," *Biomed Phys Eng Express*, vol. 6, no. 3, p. 035019, 2020.

[23] Q. Chen, J. Yu, B. M. Rush, S. D. Stocker, R. J. Tan, and K. Kim, "Ultrasound super-resolution imaging provides a noninvasive assessment of renal microvasculature changes during mouse acute kidney injury," *Kidney Int*, vol. 98, no. 2, pp. 355–365, 2020.

[24] S. R. Rao, S. E. Shelton, and P. A. Dayton, "The 'fingerprint' of cancer extends beyond solid tumor boundaries: Assessment with a novel ultrasound imaging approach," *IEEE Trans Biomed Eng*, vol. 63, no. 5, pp. 1082–1086, 2016.

[25] R. C. Gessner, S. R. Aylward, and P. A. Dayton, "Mapping microvasculature with acoustic angiography yields quantifiable differences between healthy and tumor-bearing tissue volumes in a rodent model," *Radiology*, vol. 264, no. 3, pp. 733–740, 2012.

[26] A. Panfilova *et al.*, "On the relationship between dynamic contrast-enhanced ultrasound parameters and the underlying vascular architecture extracted from acoustic angiography," *Ultrasound Med Biol*, vol. 45, no. 2, pp. 539–548, 2019.

[27] M. R. Lowerison, C. Huang, F. Lucien, S. Chen, and P. Song, "Ultrasound localization microscopy of renal tumor xenografts in chicken embryo is correlated to hypoxia," *Sci Rep*, vol. 10, no. 1, p. 2478, 2020.

[28] S. Sirsi and M. Borden, "Microbubble compositions, properties and biomedical applications," *Bubble Sci Eng Technol*, vol. 1, no. 1–2, pp. 3–17, 2009.

[29] K. Johnson, I. Oezdemir, and K. Hoyt, "Three-dimensional evaluation of microvascular networks using contrast-enhanced ultrasound and microbubble tracking," *Proc IEEE Ultrason Symp*, pp. 1–3, 2020.

[30] C. Kind, "The development of the circulating blood volume of the chick embryo," *Anat Embryol*, vol. 147, no. 2, pp. 127–132, 1975.

[31] F. W. Mauldin, D. Lin, and J. A. Hossack, "A singular value filter for rejection of stationary artifact in medical ultrasound," *Proc IEEE Ultrason Symp*, pp. 359–362, 2010.

[32] A. F. Frangi, W. J. Niessen, K. L. Vincken, and M. A. Viergever, "Multiscale vessel enhancement filtering," *MICCAI*, pp. 130–137, 1998.

[33] I. Oezdemir, S. Mohr-Allen, K. E. Peak, V. Varner, and K. Hoyt, "Three-dimensional super-resolution ultrasound imaging of chicken embryos - A validation framework for analysis of microvascular morphology," *Proc IEEE Ultrason Symp*, pp. 1–4, 2020.

[34] D. Bradley and G. Roth, "Adaptive thresholding using the integral image," *Journal of Graphics Tools*, vol. 12, no. 2, pp. 13–21, 2007.

[35] T.-C. Lee, "Building skeleton models via 3-D medial surface/axis thinning algorithms," *CVGIP*, vol. 56, pp. 462–478, 1994.

[36] P. Kollmannsberger, M. Kerschnitzki, F. Repp, W. Wagermaier, R. Weinkamer, and P. Fratzl, "The small world of osteocytes: Connectomics of the lacuno-canalicular network in bone," *New J Phys*, vol. 19, no. 7, p. 073019, 2017.

[37] R. C. Gonzalez and R. E. Woods, *Digital image processing*, Forth. Delhi, India: Pearson Education, 2018.

[38] M. Kociński, A. Materka, A. Deistung, and J. R. Reichenbach, "Centerline-based surface modeling of blood-vessel trees in cerebral 3D MRA," *Sig P Algo Arch Arr*, pp. 85–90, 2016.

[39] I. Oezdemir, K. Javed, G. Rijal, and K. Hoyt, "Contrast-enhanced ultrasound imaging of acute changes in pancreatic cancer following targeted hyaluronan treatment," *Proc IEEE Ultrason Symp*, vol. 1, pp. 2303–2306, 2019.

[40] K. Hoyt, A. Sorace, and R. Saini, "Quantitative mapping of tumor vascularity using volumetric contrast-enhanced ultrasound," *Invest Radiol*, vol. 47, no. 3, pp. 167–174, 2012.

[41] K. Hoyt, A. Sorace, and R. Saini, "Volumetric contrast-enhanced ultrasound imaging to assess early response to apoptosis-inducing anti-death receptor 5 antibody therapy in a breast cancer animal model," *J Ultrasound Med*, vol. 31, no. 11, pp. 1759–1766, 2012.

[42] M. Mahoney, A. Sorace, J. Warram, S. Samuel, and K. Hoyt, "Volumetric contrast-enhanced ultrasound imaging of renal perfusion," *J Ultrasound Med*, vol. 33, no. 8, pp. 1427–1437, 2014.

[43] S. E. Shelton *et al.*, "Quantification of microvascular tortuosity during tumor evolution using acoustic angiography," *Ultrasound Med Biol*, vol. 41, no. 7, pp. 1896–1904, 2015.

[44] C. Huang *et al.*, "Noninvasive contrast-free 3d evaluation of tumor angiogenesis with ultrasensitive ultrasound microvessel imaging," *Sci Rep*, vol. 9, no. 1, p. 4907, 2019.

[45] R. K. Jain, "Normalizing tumor microenvironment to treat cancer: Bench to bedside to biomarkers," *J Clin Oncol*, vol. 31, no. 17, pp. 2205–2218, 2013.

[46] K. Hoyt *et al.*, "Determination of breast cancer response to bevacizumab therapy using contrast-enhanced ultrasound and artificial neural networks," *J Ultrasound Med*, vol. 29, no. 4, pp. 577–585, 2010.

[47] V. Hingot, C. Errico, M. Tanter, and O. Couture, "Subwavelength motion-correction for ultrafast ultrasound localization microscopy," *Ultrasonics*, vol. 77, pp. 17–21, 2017.

[48] S. Harput *et al.*, "Two-stage motion correction for super-resolution ultrasound imaging in human lower limb," *IEEE Trans Ultrason Ferroelectr Freq Control*, vol. 65, no. 5, pp. 803–814, 2018.

[49] I. Oezdemir, C. Shaw, J. R. Eisenbrey, and K. Hoyt, "Improved quantitative contrast-enhanced ultrasound imaging of hepatocellular carcinoma response to transarterial chemoembolization," *Proc IEEE Int Symp Biomedical Imaging*, vol. 1, pp. 1737–1740, 2019.

[50] D. Ghosh, F. Xiong, S. R. Sirsi, P. W. Shaul, R. F. Mattrey, and K. Hoyt, "Toward optimization of in vivo super-resolution ultrasound imaging using size-selected microbubble contrast agents," *Med Phys*, vol. 44, no. 12, pp. 6304–6313, 2017.

[51] M. Khairalseed, I. Oezdemir, and K. Hoyt, "Contrast-enhanced ultrasound imaging using pulse inversion spectral deconvolution," *J Acoust Soc Am*, vol. 146, no. 4, p. 2466, 2019.

[52] K. Brown and K. Hoyt, "Simultaneous evaluation of contrast pulse sequences for ultrafast contrast-enhanced ultrasound imaging," *Proc IEEE Ultrason Symp*, pp. 1444–1447, 2019.

[53] P. Song *et al.*, "Improved super-resolution ultrasound microvessel imaging with spatiotemporal nonlocal means filtering and bipartite graph-based microbubble tracking," *IEEE Trans Ultrason Ferroelectr Freq Control*, vol. 65, no. 2, pp. 149–167, 2018.

[54] S. Dencks *et al.*, "Clinical pilot application of super-resolution US imaging in breast cancer," *IEEE Trans Ultrason Ferroelectr Freq Control*, vol. 66, no. 3, pp. 517–526, 2019.

# CHAPTER 8

# CONCLUSIONS AND FUTURE WORK

## 8.1 Conclusions

Microvascular networks are an integral component of all types of tissues and they may be used to monitor tissue function in patients diagnosed with several major diseases, including diabetes and cancer. Contrast-enhanced ultrasound (CEUS) provides a noninvasive characterization of tissue microvascular networks using morphological image processing pipelines. Currently, these imaging methods are limited by motion artifacts, low resolution, manual segmentation, and single plane imaging [1]. Ongoing studies suggest that advanced image registration methods can be used for motion correction and that super-resolution ultrasound (SR-US) imaging can achieve improved morphological quantification [2], [3]. Previous literature shows the necessity of additional work to be performed to provide multiscale three-dimensional (3D) quantification and visualization of tissue microvascular networks depicted in CEUS images [4], [5]. In this dissertation, the limitations of the image analysis pipeline for CEUS-derived tissue characterization are addressed using advanced image processing and multimodal imaging. Improvements are assessed using preclinical and clinical data. The purpose of this research aimed to: (1) improve the CEUS-derived image processing pipeline by using an advanced motion correction strategy and to assess the improved quantification of morphological parameters from tissue microvascular networks as a predictor of early therapy response; (2) develop and evaluate a multiscale and multiparametric quantitative analysis of high-resolution CEUS images from microvascular networks; and (3) develop and validate 3D visualization and quantification methods to demonstrate the feasibility of CEUS-derived 3D morphological microvascular analysis.

In the Chapters 2 to 4, a two-stage motion correction method to increase the accuracy of CEUS-derived morphological feature maps that manifest the structural features of the tumor vascular networks. These structural features were used to evaluate patient-specific hepatocellular carcinoma (HCC) response to transarterial chemoembolization (TACE) treatment in 36 patients. The motion-compensation approach increased the correlation coefficients (CC) values between consecutive frames by 40%. A multiscale vessel enhancement filter increased thinning accuracy by accounting for both small and large vessels together, though on different scales. By training a machine learning model with morphological features of number of vessels (NV), number of bifurcations (NB), and vessel-to-tissue ratio (VR), we achieved 86% validation accuracy, 89% sensitivity, and 82% specificity. Collectively, these performance metrics demonstrated that our model was able to make reliable pre-therapeutic predictions of HCC responses to TACE. This study showed the feasibility of morphologic feature extraction from HCC tumor vasculature after applying a motion correction strategy and the ability to assess the future TACE therapy response using CEUS imaging and machine learning.

In Chapter 5, the image analysis pipeline is enhanced with the SR-US technique to utilize the advantages of multiscale analysis. Applying the SR-US technique allowed for the selection of vessels below 100 μm, and implementation of automated vessel diameter quantification made multiscale perfusion analysis possible. This automated technique enabled reproducible and repeatable CEUS-derived tissue characterization by morphological analysis. In addition to quantifying perfusion parameters (area-under-curve (AUC) and intensity peak (IPK)), two morphological parameters (NV and VR) were also quantified using morphological image processing methods. With these functional and structural parameters together, a new tool in

diabetes research was developed for multiparametric microvascular recruitment analysis with ultrasound (US).

In Chapter 6, this multiparametric US approach was also applied to monitoring acute changes in pancreatic cancer after targeted hyaluronan (HA) treatment. This study demonstrated the association between structural and functional parameters. In response to HA-targeted therapy, HA was removed and interstitial pressure was reduced. As a result, previously collapsed microvasculature structures recovered by opening. This early response to the HA therapy was captured both quantitatively by increased perfusion and qualitatively by increased detail in the microvascular structure in the CEUS images. CEUS-derived quantifications were also validated by histological outcomes.

In Chapter 7, a 3D CEUS-derived image analysis method is developed for the characterization of the tissue microvascular networks. The image analysis pipeline was validated by multimodal imaging. First, 3D CEUS-derived vessel diameter (VD) measurements were extracted using a flow phantom of known dimensions. Two different flow phantoms were used in a series of experiments to calibrate the image processing algorithms according to the ultrasound system and the focus of the transducer. The vessel diameters from a developing chicken embryo microvascular network were then measured using 3D CEUS imaging methods. Finally, we compared the VD measurements of 3D CEUS with two-dimensional (2D) B-mode US and microscopy images using the reference method full-width-half-maximum (FWHM). 3D CEUS-derived measurements achieved an absolute error of 4.8 μm while this error was 113.9 μm for the B-mode measurements. VD measurements deviated from the true value by 6.1% in the 3D CEUS method and by 77.1% in the FWHM method from B-mode US images. Improved quantification using 3D CEUS with

advanced imaging methods demonstrated superior performance. Volume and surface reconstructions of microvascular structure improved the visualization of high-resolution CEUS images. CEUS-derived 3D microvascular network mappings will enable tracking of the same vessels for longitudinal studies in future.

### 8.2 Future work

To use CEUS-derived morphological tissue characterization, image processing will need to address computational considerations. For example, the motion correction method presented in Chapter 2 to 4 and the 3D SR-US technique presented in Chapter 5 to 7 have used high performance computation clusters (HPC) [6]. The translation of these methods to the daily clinical practice requires faster processing and elimination of the need for any HPC. Future studies, therefore, may further improve the computation time by introducing deep learning methods.

### 8.3 References


[1] K. Hoyt, H. Umphrey, M. Lockhart, M. Robbin, and A. Forero-Torres, "Ultrasound imaging of breast tumor perfusion and neovascular morphology," *Ultrasound in Medicine & Biology*, vol. 41, no. 9, pp. 2292–2302, 2015.

[2] K. Christensen-Jeffries *et al.*, "Super-resolution ultrasound imaging," *Ultrasound in Medicine & Biology*, vol. 46, no. 4, pp. 865–891, 2020.

[3] S. Harput *et al.*, "Two-stage motion correction for super-resolution ultrasound imaging in human lower limb," *IEEE Transactions on Ultrasonics, Ferroelectrics, and Frequency Control*, vol. 65, no. 5, pp. 803–814, 2018.

[4] K. Hoyt, A. Sorace, and R. Saini, "Volumetric contrast-enhanced ultrasound imaging to assess early response to apoptosis-inducing anti–death receptor 5 antibody therapy in a breast cancer animal model," *Journal of Ultrasound in Medicine*, vol. 31, no. 11, pp. 1759–1766, 2012.

[5] M. Mahoney, A. Sorace, J. Warram, S. Samuel, and K. Hoyt, "Volumetric contrast-enhanced ultrasound imaging of renal perfusion," *Journal of Ultrasound in Medicine*, vol. 33, no. 8, pp. 1427–1437, 2014.

[6] I. Oezdemir, C. E. Wessner, C. M. Shaw, J. R. Eisenbrey, and K. Hoyt, "Faster motion correction of clinical contrast-enhanced ultrasound imaging using deep learning," *Proc IEEE Ultrason Symp*, 2020.

## BIOGRAPHICAL SKETCH

İpek Özdemir attended Bursa Uludağ University where she received a BS degree in Mathematics (2002) and she then obtained her BS and MS degrees in Computer Science at the University of Applied Sciences Mittelhessen (Technische Hochschule Mittelhessen) where she was recipient of a German Academic Exchange Service (DAAD) Best International Student Award (2009). Following eight years of experience in Software Engineering with onsite assignments in several cities (Frankfurt, Istanbul, Shanghai, Minsk, and Seattle) completed with two promotions and five top engineer awards, she moved back to academia. She worked as Researcher in Brain Imaging Center in the Department of Psychiatry and Psychotherapy at the Johann Wolfgang von Goethe University (2013-2014) and as Visiting Scientist in Brain Image Computation Lab in the Department of Pediatrics at the University of Washington (2016). She then started her PhD studies in the Department of Bioengineering at The University of Texas at Dallas (2017). During her graduate studies in Dallas, she was also awarded a Jonsson Family Fellowship and Best Lecture Teaching Assistant Award. Over the course of her dissertation work, she has published nine first-author papers and presented her research at nine conference events.

**CURRICULUM VITAE**

# İpek Özdemir

(Digital Form: Ipek Oezdemir or Ipek Ozdemir)
Department of Bioengineering, 800 W Campbel Road, BSB 13.928, Richardson, TX 75080
Ipek.Ozdemir@utdallas.edu

## EDUCATION

2017 - present **PhD, Biomedical Engineering**
University of Texas at Dallas, TX, USA
Dissertation title: *"Novel Ultrasound Imaging Methods for the Characterization of Tissue Microvascular Networks"*
*Advisor: Assoc. Prof. Dr. Kenneth Hoyt*

2004 - 2009 **BS and MS, Computer Science**
University of Applied Sciences - Technische Hochschule Mittelhessen, Giessen, Germany
MS Thesis: *"Analysis of Open Source Enterprise Service Bus MULE"*
*Advisor: Prof. Dr. Thomas Letschert*
BS Thesis*: "Analysis of Open Service Gateway iniative Architecture"*
*Advisor: Prof. Dr. Peter Kneisel*

2003 **DSH Exam**
The language exam to begin studies in German**.**

1998 - 2002 **BS, Mathematics**
Bursa Uludağ University, Bursa, Turkey

## PROFESSIONAL RESEARCH & WORK EXPERIENCE

08.2017-present **Research Assistant,**
Ultrasound Imaging and Therapy Laboratory, Dallas, TX, USA
Department of Bioengineering, University of Texas at Dallas

08.2018-2019 **Teaching Assistant,**
Department of Bioengineering, University of Texas at Dallas
Biomedical Image Processing, Medical Imaging System and Methods, Digital Circuits

| | |
|---|---|
| 2016 | **Visiting Scientist,**<br>Biomedical Image Computing Group, Seattle WA, USA<br>Department of Pediatrics, University of Washington Medical Center |
| 2013-2014 | **Researcher,**<br>Brain Imaging Center, Frankfurt, Germany<br>University Clinic, Johann Wolfgang Goethe University |
| 2007-2009 | **Researcher,**<br>Computer Science Department, Giessen, Germany<br>University of Applied Sciences-Technische Hochschule Mittelhessen |
| 2006-2007 | **Intern,**<br>Siemens Medical Solutions, Kemnath, Germany |
| 2009-2017 | **Software Engineer (SE), Senior SE, Specialist SE**<br>Frankfurt, İstanbul, Shanghai, Minsk, Seattle<br>Ericsson Telecommunication, Germany, China, Belarus, USA |

## PEER-REVIEWED PUBLICATIONS

**Özdemir İ**, Johnson K, Mohr-Allen S, Peak KE, Varner V, Hoyt K. Three-dimensional visualization and improved quantification with super-resolution ultrasound imaging – Validation framework for analysis of microvascular morphology using a chicken embryo model. Physics in Medicine & Biology 66 (8), 085008, 2021.

**Oezdemir I**, Wessner CE, Shaw C, Eisenbrey JR, Hoyt K. Tumor vascular networks as predictor for transarterial chemoembolization treatment response. Ultrasound in Medicine and Biology, 46: 2276-2286, 2020.

**Oezdemir I**, Peng J, Ghosh D, Sirsi SR, Mineo C, Shaul PW, Hoyt K. Multiscale and morphological analysis of microvasculature patterns depicted in contrast-enhanced ultrasound images. Journal of Medical Imaging, 7: 034001, 2020.

**Oezdemir I**, Peak KE, Mohr-Allen S, Varner V, Hoyt K. Three-dimensional super-resolution ultrasound imaging of chicken embryos – A validation framework for analysis of microvascular morphology. Proc IEEE Ultrason Symp, 1-4, 2020.

**Oezdemir I**, Wessner C, Shaw C, Eisenbrey JR, Hoyt K. Faster motion correction of clinical contrast-enhanced ultrasound images using deep learning. Proc IEEE Ultrason Symp, 1-4, 2020.

Zheng, Q, Jones FK, Leavitt SV, Ung L, Labrique AB, Peters DH, Lee EC, Azman AS **& HIT-COVID Collaboration**. HIT-COVID, a global database tracking public health interventions to COVID-19. Sci. Data 7, 286 (2020)

Johnson K, **Oezdemir I**, Hoyt K. Three-dimensional evaluation of microvascular networks using contrast-enhanced ultrasound and microbubble tracking. Proc IEEE Ultrason Symp, 1-3, 2020.

**Oezdemir I**, Wessner C, Shaw C, Eisenbrey JR, Hoyt K. Multiscale quantification of tumor microarchitecture for predicting therapy response using dynamic contrast-enhanced ultrasound imaging. Proc IEEE Ultrason Symp, 1173-1176, 2019.

**Oezdemir I**, Javed K, Rijal G, Hoyt K. Contrast-enhanced ultrasound imaging of acute changes in pancreatic cancer following targeted hyaluronan treatment. Proc IEEE Ultrason Symp, 2303-2306, 2019.

**Oezdemir I**, Shaw C, Eisenbrey JR, Hoyt K. Improved quantitative contrast-enhanced ultrasound imaging of hepatocellular carcinoma response to transarterial chemoembolization. Proc IEEE Int Symp Biomedical Imaging, 1737-1740, 2019.

**Özdemir I**, Hoyt K. Morphological processing for multiscale analysis of super-resolution ultrasound images of tissue microvascular networks. Proc of the SPIE, 1095505: 1-9, 2019.

Khairalseed M, **Oezdemir I**, Hoyt K. Contrast-enhanced ultrasound imaging using pulse inversion spectral deconvolution. Journal of the Acoustical Society of America, 146: 2466-2474, 2019.

Brodski-Guerniero A, Paasch GF, Wollstadt P, **Özdemir I**, Lizier JT, Wibral M. Information theoretic evidence for predictive coding in the face-processing system. Journal of Neuroscience, 37(34):8273-8283, 2017.

## POSTER-PRESENTATIONS

**Oezdemir I**, Peak KE, Mohr-Allen S, Varner V, Hoyt K. Three-dimensional super-resolution ultrasound imaging of chicken embryos – A validation framework for analysis of microvascular morphology. IEEE International Ultrasonics Symposium, Las Vegas (virtual), NV, USA, 2020.

**Oezdemir I**, Wessner C, Shaw C, Eisenbrey JR, Hoyt K. Faster motion correction of clinical contrast-enhanced ultrasound images using deep learning. IEEE International Ultrasonics Symposium, Las Vegas (virtual), NV, USA, 2020.

Johnson K, **Oezdemir I**, Hoyt K. Three-dimensional evaluation of microvascular networks using contrast-enhanced ultrasound and microbubble tracking. Proc IEEE Ultrasonics Sysmposium, Las Vegas (virtual), NV, 2020

Javed K, **Oezdemir I**, Rijal G, Hoyt K. Monitoring acute changes in pancreatic tumor perfusion with contrast-enhanced ultrasound imaging following targeted hyaluronic acid treatment. Biomedical Engineering Society Annual Meeting, Philadelphia, PA, USA, 2019.

**Oezdemir I**, Shaw C, Eisenbrey JR, Hoyt K. Improved ultrasound imaging assessment of hepatocellular carcinoma response to transarterial chemoembolization. American Institute for Ultrasound in Medicine Annual Convention, Orlando, FL, USA, 2019.

**Oezdemir I**, Hoyt K. Multiscale analysis of super-resolution ultrasound images of tissue microvascular networks. Biomedical Engineering Society Annual Meeting, Atlanta, GA, USA, 2018.

Gwendolyn Van Steenkiste, **Ipek Oezdemir**, Chris Gatenby, Colin Studholme. Framework to evaluate cortical FA mapping from motion corrected fetal diffusion weighted image. The Organization for Human Brain Mapping, Vancouver, BC, Canada, 2017.

Christoph Hartmann, **Ipek Oezdemir**, Michael Wibral, Ralf Galuske, Jochen Triesch, Matthias Kaschube. Local information dynamics in a model of A18-PMLS interaction in cat visual cortex. Bernstein Conference, Goettingen, Germany, 2014.

## TALKS

**Oezdemir I**, Shaw C, Eisenbrey JR, Hoyt K Multiscale quantification of tumor microarchitecture for predicting therapy response using dynamic contrast-enhanced ultrasound imaging. International Ultrasonic Symposium, SEC, Glasgow, Scotland, 8 Oct 2019.

**Oezdemir I**, Shaw C, Eisenbrey JR, Hoyt K. Improved quantification of microvascular structures in contrast-enhanced ultrasound images. Kavli Futures Symposium – Ultrasound Contrast Research, Dallas, TX, USA, 22 Feb 2019.

**Oezdemir I**, Hoyt K. Morphological image processing for multiscale analysis of super-resolution ultrasound images of tissue microvascular networks. SPIE Conference, San Diego, CA, USA, 19 Feb 2019.

**Oezdemir I**, Information theoretic analysis on neuronal data using Java Information Dynamics Toolkit (JIDT). Bernstein Center Freiburg, Germany, 1 Feb 2016.

## AWARDS

2019 **Jonsson Family Graduate Fellowship in Bioengineering**
Merit-based fellowship for graduate student in biomedical engineering in the Jonsson School, Dallas, TX, USA

2019 **Best Lecture Teaching Assistant Award**
Biomedical Engineering Department, Dallas, TX, USA

2009-2015 **Top Engineer Awards, Ericsson**
For the customer projects PCI/Israel (2009 and 2010), AVEA/Turkey (2012), VELCOM/Belarus (2013), and T-MOBILE/USA (2015)

2007 **Best International Student**
DAAD German Academic Exchange Service

## PROFESSIONAL MEMBERSHIPS

2021 Alpha Eta Mu Beta (AEMB)

2020 International Contrast Ultrasound Society (ICUS)

2019 The American Institute of Ultrasound in Medicine (AIUM)

2018 The International Society for Optics and Photonics (SPIE)

2017 Biomedical Engineering Society (BMES)

2015 Bernstein Network Computational Neuroscience